SYNTHESIS, PROPERTIES, AND APPLICATIONS OF FUNCTIONAL POLYMER FILMS

By

Liudmyla Prozorovska

Dissertation

Submitted to the Faculty of the

Graduate School of Vanderbilt University

in partial fulfillment of the requirements

for the degree of

DOCTOR OF PHILOSOPHY

in

Interdisciplinary Materials Science

May 31, 2021

Nashville, Tennessee

Approved:

G. Kane Jennings, Ph.D.

Douglas E. Adams, Ph.D.

Paul E. Laibinis, Ph.D.

Shihong Lin, Ph.D.

Greg Walker, Ph.D.

To my husband Sean, who inspires me

"To strive, to seek, to find, and not to yield."

To my parents, teachers, and professors

with profound respect and gratitude.

ACKNOWLEGEMENTS

I am thankful for my time at Vanderbilt, funding from the Vanderbilt School of Engineering and the U.S. Department of Energy (Award Numbers DE-NE0008712 and DE-EE0006926), and for the people who sustained me during this journey.

My dear advisor, Dr. Kane Jennings: your kindness, trust, and gentle guidance exemplify mentorship. You granted me a chance to pursue research I was most passionate about – for that I will always be thankful. I would like to extend special gratitude to Dr. Douglas Adams, who was my advisor during the first two years of graduate school. Thank you for your unwavering support; your generous spirit and contagious enthusiasm motivated and inspired me. I am also grateful to my committee members: Dr. Paul Laibinis, Dr. Shihong Lin and Dr. Greg Walker for your help in numerous matters, astute observations, guidance, encouragement, and good humor.

To my lab mates, Dr. Xuanli "Ricky" Deng, Bradley Baker, Joshua Passantino, Marc Nabhan, Kody Wolfe, and Rabeb Layouni: you made the time spent in the lab special. I am thankful for all the jokes and all the songs, our fruitful discussions and your help that was always there when I needed it. Thank you to the undergraduate students, Long Than and Carly Shafer, for graciously enduring my mentorship and putting in hours of hard work. Brad, thank you for teaching me lab techniques and your friendship; the lab would not be the same without you there. Rabeb, we supported each other through the difficult times; I am happy to have met you, dear friend. To my friend Krysta Waldrop: you elevated my grad school experience. I am grateful for the companionship of my IMS buddies Dr. Matt Gerboth, Dr. Casey Brock, Dr. Jake Benzing, Dr. Tengfei Cao, and Dr. Drew Tonigan – study partner and confidant.

I would like to thank Vanderbilt Institute of Nanoscale Science and Engineering (VINSE) community, particularly Sarah Ross, Alisha McCord, Dr. Alice Leach, Dr. Dmitry Koktysh, Dr. Anthony

Hmelo, and Robin Midgett, for their limitless help and friendship. Sarah and Alice, your warmth during my first two visits to Vanderbilt solidified my desire to study here. Sarah, I am forever grateful for your caring nature – if not for you, I would not have gotten this far. Alisha, thank you for your support at work and fun outside of it. Robin, you are a dear friend, I can't thank you enough for your help and kindness. Dr. Koktysh, thank you for all the cordial advice, training, and troubleshooting. Dr. Hmelo, thank you for patiently teaching me how to operate most of the sophisticated instruments in VINSE.

To the staff and students of Laboratory of Systems Integrity and Reliability, Dave Koaster, Garrett Thorne, Raymond Bond, Dr. Janett Mayer, Dr. Cole Brubaker, Dr. Christopher Nash, Thomas Stilton – thank you for the productive work and fun memories. Dave and Garrett, thank you for the support during my time at the lab and beyond. Ray, thank you for everything you taught me and helped me with, but most of all for your friendship. Many thanks to the Chemical Engineering department staff, Felisha Baquera and Mark Holmes for assisting with millions of administrative issues. Thank you to Rossane Delapp and Dr. Lesa Brown from Civil Engineering department for their kind help and advice on experiments.

Thank you to Dr. Andrew Westover, Dr. Nitin Muralidharan, and Dr. Cary Pint for the collaboration on cure monitoring of epoxy-based electrolytes; I am also grateful to Dr. Pintauro's group, especially Dr. Devon Powers, for the access to their Differential Scanning Calorimeter used in this project. Thank you to Linglong Shan, and Dr. Shihong Lin for the opportunity to contribute to their research on loose nanofiltration membranes with integrated surfactant self-assemblies.

To my beloved parents, Olena and Valerii, thank you for my life and the lessons I learned from you. To my family and friends in Ukraine and the US – thank you for your love and support. To my husband Sean: my soul had not been whole until I met you, and I thank the universe for you every day. No words can express my gratitude for your support. I am excited about our life of adventure ahead.

TBALE OF CONTENTS

LIST OF TABLES

LIST OF FIGURES

LIST OF ABBREVIATIONS

ARGET	activator regenerated by electron transfer
ATR	attenuated total reflection
ATRP	atom transfer radical polymerization
AsAc	ascorbic acid
CRP	controlled radical polymerization
DCM	dichloromethane
DCPD	dicyclopentadiene
DMF	dimethyl formamide
DI	deionized
DSC	differential scanning calorimetry
EDS	energy-dispersive X-ray spectroscopy
EEC	equivalent electric circuit
EIS	electrochemical impedance spectroscopy
FTIR	Fourier transform infrared spectroscopy
G2	Grubbs' catalyst 2nd generation
G3	Grubbs' catalyst 3rd generation
GMA	glycidyl methacrylate
HA	hydroxamic acid
HSAB	hard and soft acids and bases
NBDAC	norbornene diacyl chloride
NBOH	norbornene-2-methanol

NMR	nuclear magnetic resonance
IL	ionic liquid
IUPAC	International Union of Pure and Applied Chemistry
QCM	quartz crystal microbalance
PEI	polyethyleneimine
PMDETA	pentamethyl diethylenetriamine
PM-IRRAS	polarization modulation-infrared reflection absorption spectroscopy
PPM	post-polymerization modification
PSS	polystyrene sulfonate
RP	radical polymerization
ROMP	ring opening metathesis polymerization
SAM	self-assembly monolayer
SDS	sodium dodecyl sulfate
SEM	scanning electron microscope
Si-	surface-initiated-
SIP	surface-initiated polymerization
TGA	thermogravimetric analysis
UV-vis	ultraviolet–visible

Chapter I

INTRODUCTION

Materials have defined epochs: Stone Age, Bronze Age, Iron Age, … the Age of Plastic[1,2]. New materials enable revolutionary technology, altering the face of our planet and the history of human civilization. In our post-industrial society, the paradigm for the development of materials shifted to purposeful design: researchers focus on creating materials with a set of characteristics determined by the desired end use. From this approach emerged a class of advanced polymers with molecular building blocks chosen and arranged based on the required function[3,4].

Functional polymers are macromolecules with unique properties and applications that depend on the presence of specific chemical moieties within their structure[5]. Such polymer chains can have useful intrinsic properties (e.g. electron[6–8] and proton[8,9] conductivity, specific wettability[10,11], self-healing[12,13], low refractive index[14], selective binding of particular species[15,16], etc.), respond to external stimuli[17,18] (e.g. shifts in temperature[19–21], pH conditions[22–24], concentrations of molecules and ions[25], and electric/magnetic fields[26]), and self-assemble into supramolecular structures[27–29].

Thin films of functional polymers are produced for a myriad of applications, including membranes[30,31], sorption media and scaffolds[32,33], sensors[34,35], organic electronics[36–41], packaging[42], barrier[43,44], dielectric[45,46], bio-active[47], non-fouling[48], lubricative[49] or antireflective[50] coatings over substrates and devices, etc. Techniques for preparation of polymer thin films fall into three broad categories: 1) physical deposition methods, such as drop casting[40], dip coating[51], electrospinning[47,52,53], doctor blading[40], printing[54,55], micromolding[56–58], and spin coating[59,60]; 2) self-assembly, e.g., Langmuir−Blodgett process[61], layer-by-layer assembly[62,63]; 3) chemical bonding methods, comprising "grafting-to"[64] and "grafting-from"[65] approaches.

The majority of the film fabrication techniques introduced above are used routinely in the Jennings' laboratory at Vanderbilt University, where the author has had the privilege to work.

Drop casting is one of the simplest methods for obtaining a polymer film. A polymer is dissolved in an appropriate solvent, the liquid is dispensed onto a substrate and allowed to dry. The films of wide range of thicknesses can be obtained without any special equipment; however, precise control over the thickness and uniformity of the films is challenging[40]. Often, a "coffee ring" effect is observed upon drying[66]. In addition, to avoid crystallization and precipitation of the polymer during the solvent evaporation, good solubility of the polymer in a chosen solvent is required[40], which places constraints on the polymer composition and/or quality of the resulting film.

Dip (or immersion) coating[51] is another well-established technique for polymer film preparation. Batch dip coating is applied for rigid substrates that cannot be conveniently linked into a continuous line, while long flexible substrates or fibers can be coated in a continuous process[51]. Dip coating consists of three principal stages[67]: 1) immersion and dwell time, 2) deposition and drainage, 3) solvent evaporation and drying. The thickness and uniformity of the films prepared by dip coating is determined by the interplay of many factors, including surface tension, viscous force, speed of substrate withdrawal, solvent volatility, and flow conditions of the liquid bath and ambient air[51]. Such complexity makes theoretical prediction, optimization, and control of the process performance difficult, but a number of semi-experimental equations published to date[67] predict the critical withdrawal speed and minimum thickness for a given deposition solution reasonably well.

Spin coating is extensively employed in academia and industry due to its ability to quickly yield structurally uniform films over moderately large areas ($\geq$ 30 cm in diameter) with high reproducibility[60]. In a typical spin coating process, a polymer solution in a volatile solvent is deposited on a substrate, which is either already rotating or is immediately accelerated to the desired velocity (usually chosen within the

range of 400 – 8000 rpm), so the fluid spreads evenly under the centrifugal force[68,69]. While spin coating is mainly used for planar substrates[60], the technique is also adaptable to substrates with complex geometry, such as foams[70] and topographically patterned surfaces[71–73]. Spin coating can be broadly divided into four key stages[51,74,75]: 1) deposition, 2) spin-up (outward flow of the solution driven by centrifugal force), 3) spin-off (outward flow and ejection of excess polymer solution), and 4) solvent evaporation. The morphology of the resulting polymer films depends on the characteristics of the polymer solution and the substrate, as well as the process parameters[76,77].

Over the years, spin coating was modeled with various degrees of complexity. Emslie et. al[78] offered the first theoretical description of the process for Newtonian fluids, where the thinning rate is defined as:

$$\frac{dh}{dt} = -2\frac{\rho\omega^2}{3\eta}h^3 \quad (1)$$

where h is the films thickness, t is time, ρ is the fluid density, ω is the rotation rate in radians per second and η is the viscosity in poise.

To accurately describe the latter stages of spin coating, the effects of solvent evaporation must be taken into account. Thus, Meyerhofer[79] introduced an evaporation rate term (e, [ml s^{-1} cm^{-2}]) into the equation (1):

$$\frac{dh}{dt} = -2\frac{\rho\omega^2}{3\eta}h^3 - e \quad (2)$$

Equation (2) can be solved by assuming that the loss of the film thickness due to evaporation was negligible until the thinning due to the radial flow decreased to the level of evaporation rate[69]. Later, a number of computational models[69,80,81] with various refinements were proposed; however, these models still rely on the basic principles described above[74].

The term "self-assembly" defines spontaneous organization of molecules into stable aggregates joined by noncovalent, intermolecular forces (e.g., electrostatic interactions, hydrogen bonding, van der Waals forces) and weak covalent (coordination) bonds[28]. The concept was pioneered by a Noble Laureate Jean-Marie Lehn within the field of supramolecular chemistry[82]. In the 1990s, Whitesides' research group developed self-assembly of nanoscale structures[83], while Stupp and coworkers extended the concept to functional bulk materials and polymers[27,84]. The principles of self-assembly continue to enable innovations in materials and technology development today.

Self-assembled monolayers (SAMs) are two-dimensional organic structures, most commonly formed by adsorption of molecules from solution or gas phase onto solid substrates[85–87]. The molecules that form SAMs have a distinct structure, consisting of a "head group" with specific affinity to a substrate, a hydrocarbon "spacer", and an "end" group of particular functionality[85]. Examples of adsorbate/substrate combinations include[88]: 1) sulfur-containing molecules on gold[89], silver[90,91], copper[92], indium-tin oxide, gallium arsenide[93], and indium phosphate; 2) alkylsilane derivatives on hydroxylated surfaces[87]; 3) carboxylic acids on aluminum oxide and silver[88]; 4) alcohols, amines, and isonitriles on platinum[88]. SAMs provide a convenient way to tailor the interfacial properties of numerous bulk materials and are extensively employed in surface patterning and bottom-up nanofabrication techniques[94].

Layer-by-layer assembly[63,95] implies alternating deposition of materials into multilayer structures based on complementary electrostatic[96], hydrogen bonding[62], and host-guest[97] interactions. The technique established an easy, efficient, and versatile route for fabrication of thin films and nanostructures from diverse materials, including polymers, proteins, nanoparticles, dyes, surfactants, etc., over any type of substrate[98] or in a freestanding format[99].

Covalent attachment of molecules and polymers to substrates is required for obtaining modified surfaces with enhanced physiochemical stability and durability. For polymers, two distinct strategies have

emerged: "grafting-to"[64] and "grafting-from"[65] a substrate. "Grafting-to" is accomplished by reacting functionalized polymers (in solution or melt) with a complementary chemical moiety on the surface of a substrate. The ability to thoroughly characterize the polymers prior to the attachment is a significant advantage of this method[64]. However, the thicknesses of the films prepared by "grafting-to" are typically much below 100 nm (the efficiency of immobilization reaction drops dramatically for polymers with high molecular weight) and the grafting density is limited due to steric hindrance[64,65,100].

"Grafting-from" involves in situ polymerization from an initiator immobilized onto a surface (usually via a monolayer), which yields tethered polymer films[101,102]. Hence, the alternative name for the technique is surface-initiated polymerization (SIP). The SIP methods[103] 1) negate the need for the preparation of bulk polymers, their subsequent purification and dissolution (ensuring economical use of materials and ease of product separation); 2) provide improved stability of the grafted polymer chains; 3) enable more precise control over film composition, architecture, and thickness; 4) allow for uniform film coverage and patterning on substrates of various compositions and complex geometries. The main SIP approaches are based on well-known polymerization techniques, such as atom transfer radical polymerization (ATRP)[104–106] and ring opening metathesis polymerization (ROMP)[36,43,44,107].

This dissertation encompasses synthesis and characterization of functional polymer films designed for their target applications. In Chapter II, relevant polymerization strategies are reviewed, and specific functional groups are highlighted. Chapter III describes synthesis of polymer films containing catechol moieties via surface-initiated (Si-) ATRP and post-polymerization modification. Chapter IV presents a new method (in-situ ROMP during spin-coating) for synthesizing tethered and freestanding films, with emphasis on the properties of polynorbornene films containing hydroxamic acid functional groups. Chapter V reports cure monitoring and characterization of epoxy/amine networks, modified with 1-butyl-3-methylimidazolium tetrafluoroborate ionic liquid. Additionally, layer-by-layer assembly and

characterization of surfactant-intercalated polyelectrolyte thin films used as separation layers in loose nanofiltration membranes is presented in the Appendix.

Chapter II

BACKGROUND

Polymerization methods

A polymer (from Greek "poly-" – many and "-mer" – part) is a substance of high molecular mass consisting of multiple covalently linked repeating subunits (monomers). In general, a polymerization process involves a recuring reaction in which a monomer is converted into a polymer segment[108]. Now, chemists have an arsenal of polymerization methods to choose from, enabling the synthesis of polymers with specific properties and functions. However, each method has a unique set of benefits and constraints: for instance, special reaction conditions, high-purity reagents, and protection of certain functional groups of the monomers are often required.

Step-growth[109] polymerization is based on the individual reactions between the functional groups present in the monomers. The buildup of the polymer chain proceeds slowly in a random manner, continuing whenever molecules with appropriate functional groups, geometry, and sufficient activation energy collide and react[110]. The moieties at the end of the growing polymer chain and monomers have the same reactivity. Thus, species with a broad distribution of molecular weights exist throughout the course of polymerization. Linear polymers with high molecular weight can be obtained from difunctional monomers, but the following conditions[109] are critical: perfect stochiometric balance between the reagents, high degree of reagent purity, absence of side reactions, and high yield from the polymerization reaction itself. Although most of the polymers found in nature are step-growth polymers, only a fraction of commercially available synthetic polymers is currently produced by this method, because few reactions meet the above-mentioned requirements at feasible costs. Notably, epoxide resins[111] ubiquitous in

consumer and industrial applications are produced though polycondensation between oxirane-containing molecules and amines (as they were prepared in Chapter VI of this thesis).

Chain-growth polymerization[110] rapidly yields high molecular weight species via addition of monomers to a growing polymer chain end by one unit at a time. Polymerization proceeds through distinct stages, including initiation, propagation, chain transfer, and termination, all of which have different rates and mechanisms (Fig. 2.1)[112]. During propagation, monomers (M) react exclusively with the active species (M*) at the end of the growing polymer chain. By limiting or, ideally, eliminating the chain transfer and termination, "living" polymerizations can be achieved[112], which offer enhanced control over polymer architectures and chain functionalities[113].

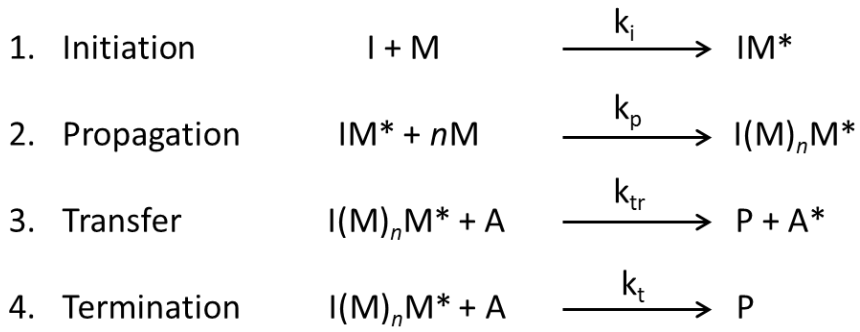

Figure 2.1. General schematics of key stages of chain-growth polymerization[112], where I is initiator, M – monomer, M* – active center, A – reagent, P – inactive polymer chain, and k_i, k_p, k_{tr}, k_t are the corresponding rate constants.

During the initiation step, the growth of a polymer chain can be started by a cation, anion, free radical initiator or a coordination catalyst[110]. Consequently, the major chain polymerization techniques derive their names from the type of initiation.

Ionic polymerization methods

Cationic and anionic polymerizations involve formation and propagation of ionic species (carbocations and carbanions) as active centers, and require monomers that have electron-donating (e.g., phenyl, vinyl) and electron-withdrawing (e.g., carboxyl, halide) groups, respectively[110]. Examples of initiators for cationic polymerization include sulfuric acid, perchloric acid, and pure Lewis acids, such as $AlCl_3$, BF_3, with a co-catalyst (e.g., water)[110]. Anionic polymerizations are typically initiated by strong nucleophiles, such as alkyllithium compounds[114]. To obtain high molecular weight products though ionic polymerizations, the stability of delicate active species must be preserved during the propagation stage, which imposes stringent reaction conditions[112]: strictly anhydrous and deoxygenated medium, high purity reagents, exclusion of polar solvents. However, ionic polymerizations yield more linear polymers with narrower molecular weight distribution, compared to radical polymerization, and are suitable for preparation of well-defined block copolymers[112].

Coordination polymerization methods

Polymerization using coordination catalysts was pioneered by Giulio Natta and Karl Ziegler in the 1950s for production of polymers with high degree of crystallinity (isotactic polypropylene and high-density polyethylene)[110], discovery of which made a tremendous economic impact[115]. The Zeigler-Natta catalysts are a combination of transition metal compound from groups IV – VIII of the periodic table (e.g., $TiCl_4$), referred to as the "catalyst", and a metal cation from groups I – III (e.g., $Al(C_2H_5)$) – the "cocatalyst". The main distinction of the polymerization technique is that the growing chain is bound to the metal atom of the catalyst and the monomers are incorporated into the propagating chain through their coordination with the metal[116]. Coordination polymerization can be terminated by introduction of water, hydrogen, aromatic alcohol, and certain metals into the reaction medium[116]. The first generation of catalysts produced stereoregular polymers but at a low yield. Subsequently, catalyst systems were

improved to enable high yields and better stereoselectivity, while being less sensitive to contamination[115]. In the 1980s metallocene catalysts were developed[116], which typically consist of a transition metal, M, from group IV of the periodic table (Zr, Ti, Hf), cyclopentadienyl ligand, Cp, and a halogen, X, (Cl or Br), e.g., Cp_2MX_2. These catalyst systems provide an avenue to obtain extremely uniform polymers with narrow molecular weight distribution, and can produce more polymer per quantity of catalyst used, compared to Zeigler-Natta systems[116].

Olefin metathesis is a catalytically induced reaction, entailing scission and redistribution of carbon-carbon double bonds[110], which was discovered accidentally through studies on Zeigler-Natta polymerizations and initially used similar catalyst systems – a transition metal compound with an organometallic alkylating agent[117]. Nowadays, olefin metathesis catalysts usually contain chlorides, oxides, and other readily accessible compounds of Mo, Ru, Re, or W[118]. The most important olefin metathesis subtypes are cross metathesis, ring closing metathesis, and ring opening metathesis reactions[119]. Ring opening metathesis polymerization (ROMP) enables synthesis of a wide range of functional polymers with specific architectures. The technique was utilized in Chapter V of this thesis.

Ring-opening metathesis polymerization (ROMP)

ROMP is a chain-growth polymerization method utilizing cyclic olefins to produce monodisperse stereoregular polymers with unsaturated backbones[120,121]. The driving force of ROMP is relief of the ring strain, which has to overcome the entropic penalties associated with polymerization[120], therefore monomers with high strain energy, such as norbornenes (E = 100 kJ/mol), react the most efficiently[122]. As ROMP is an equilibrium-controlled reaction, the highest monomer concentration and the lowest temperature are favored. The technique achieved its current popularity after Robert Grubbs developed Ru-based catalysts[123], which are selective toward olefins over any other functional group and tolerate ambient

oxygen and moisture[124]. Many catalysts enable living ROMP; thus ROMP has become one of the most versatile living polymerization techniques in terms of functional group tolerance[120].

The general mechanism of ROMP, first elucidated by Chauvin[125], is presented in Figure 2.3[120]. The polymerization is initiated by coordination of a transition metal alkylidene complex to a cyclic olefin and subsequent cycloaddition that, through formation of a four-membered metallacyclobutane intermediate, establishes the active site for the growth of the polymer chain[120]. Despite the increased size, the reactivity of the active species toward cyclic olefins is similar to that of the initiator[120]. So, the propagation proceeds in the analogous manner until the monomer is consumed, the reaction equilibrium is attained, or the reaction is terminated (often through introduction of a terminating agent, which replaces the metal with a specific functional group)[120]. In addition, intra- and intermolecular chain transfer reactions may occur, which are undesirable in ROMP but useful for synthesis of cyclic oligomers[120].

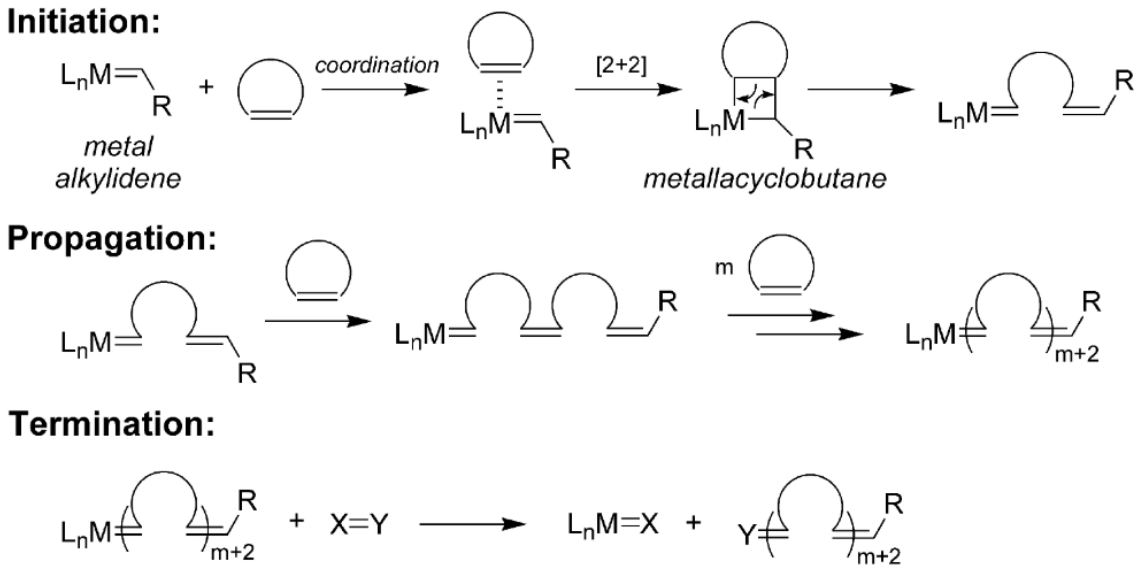

Figure 2.2. General schematics of a typical ROMP process[120].

To execute surface-initiated ROMP (Si-ROMP)[36,44,126,127], the catalyst is first bound onto a desired substrate, typically through a thiol[85,86] (on Au) or silane[86,87] (on Si/SiO_2) self-assembled monolayer (SAM). After immobilization of the catalyst, the substrate is immersed into a monomer solution to yield a polymer film attached to the surface. The thickness of the films obtained by Si-ROMP can be controlled by varying the concentration of the monomer[127] and the duration of polymerization[44].

Radical polymerization methods

Radical polymerization[128] (RP) proceeds though in situ generation of organic free radicals by homolytic cleavage of covalent bonds using heat, light, or high-energy radiation[112]. In contrast to carbocations and carbanions, radicals are comparatively stable active species, and can be further stabilized by resonance and, to a lesser extent, polar effects[129]. Hence, RP is tolerant to impurities and monomer stabilizers, compatible with water, protic solvents, and wide range of functional monomers[128,130]. Quite predictably, at least 50% of all commercialized polymers, including low density polyethylene, poly(vinyl alcohol), polyacrylates, polystyrene, and fluorinated polymers, are currently produced by RP[129]. The major disadvantage of RP is limited control over polymer molecular weight distribution and architecture: the propagating radicals are susceptible to bimolecular termination, transfer, and other side reactions[130].

Controlled radical polymerization (CRP) emerged from the efforts to mitigate the drawbacks of RP while preserving its flexibility. The key difference of the CRP mechanism is the presence of dormant species and intermittent reversible activation, which alleviate the chain breaking reactions and extend the lifetime of propagating chains (by at least 60 times compared to RP) to over 1 h[129]. Superior control over chain architecture is attainable, as in most types of CRP systems initiation is very fast and almost instantaneous growth of all chains can be realized[129]. The three most renowned types of CRP processes are nitroxide-mediated polymerization (NMP)[131], atom transfer radical polymerization (ATRP)[132], and reversible addition fragmentation chain transfer (RAFT)[133] polymerization. RAFT features a degenerative

transfer mechanism with either alkyl iodides or dithioesters as transfer agents[113]. NMP and ATRP are based on spontaneous or catalyzed persistent radical effect, respectively, and involve reversible activation/deactivation of the radical species[113]. As a variant of ATRP is utilized in research included in this dissertation (Chapter IV), the method is reviewed in more detail below.

Atom transfer radical polymerization (ATRP)

ATRP is a transition-metal mediated controlled radical polymerization method based on reversible redox activation of an organic radical on a polymer chain terminated with an alkyl-halide (dormant species) by a halogen transfer to a transition metal complex[134] (Fig. 2.3.). Complexes of Cu with N-based polydentate ligands (e.g., pentamethyl diethylenetriamine (PMDETA)) are commonly employed as catalysts in ATRP[129]. The ligand is chosen to ensure good solubility of the metal halide in the reaction medium and to adjust the redox potential of the metal, which affects the activation/deactivation kinetics of the polymer chains during the reaction[134]. ATRP is suitable for a wide variety of functional monomers and provides an improved control over polymer architecture and polydispersity. However, the propagating radicals can be rapidly trapped by O_2, so the reaction mixture for ATRP must be rigorously deoxygenated.

To simplify the synthesis routine and reduce the amount of catalyst needed down to ppm level, activator regenerated by electron transfer (ARGET) ATRP[135] was developed as an alternative process that is tolerant to limited amounts of O_2. Oxidatively-stable Cu^{II} species (e.g. $CuBr_2$) are added to the reaction solution, and after mixing and partial deoxygenation by N_2 bubbling, a reducing agent (e.g. ascorbic acid (AsAc)[136]) is introduced to generate Cu^{I} species which activate the polymerization (Fig. 2.3.). As in conventional ATRP, in ARGET ATRP the reaction equilibrium is strongly shifted toward dormant species ($K_{ATRP} = k_{act}/k_{deact}$, $k_{act} <<< k_{deact}$)[134]. Occurrence of termination reactions decreases steadily with the increase in polymer chain length, as long chains undergo cross-termination with initiating radicals and newly generated short chains much faster than with other polymer chains of high molecular weight[134].

The reducing agent compensates for any loss of active species due to biradical termination[134], but one must ensure that the acid produced during the regeneration step does not induce dissociation of the metal/ligand complex[137]. Excess ligand or reducing agent (acting as a base) is usually required to trap the acid[137].

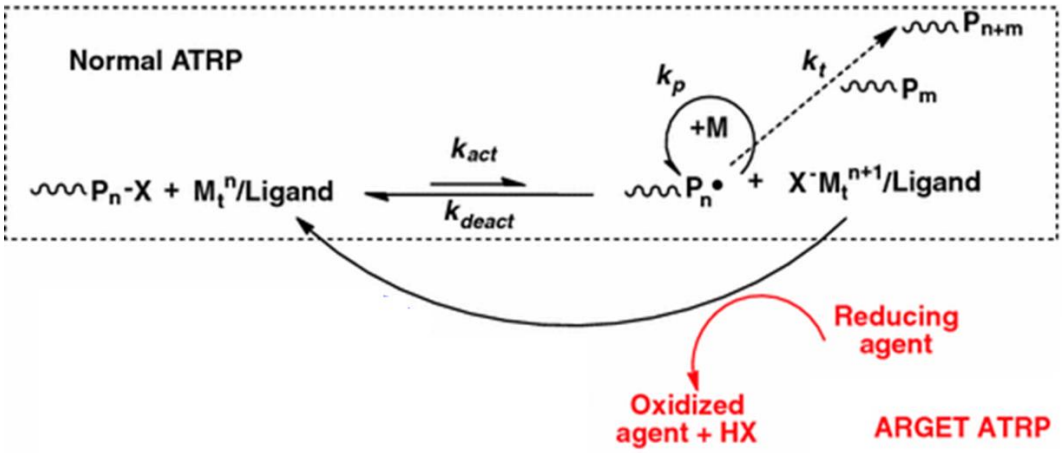

Figure 2.3. Schematic representation of ATRP and ARGET ATRP reactions[138], where M_t^n is a transition metal, L_n is a complexing ligand, X and HX are a halogen (Br or Cl) and the corresponding acid, M is a monomer, P_n- and $P_n^\bullet$ designate a dormant and propagating polymer chain, respectively, and k_{act}, k_{deact}, k_p, k_t are the rate constants of activation, deactivation, propagation, and termination respectively.

For Si-ARGET ATRP[104], initiator molecules, for example, containing an alkyl halide[101], from which a stable radical can be generated via homolytic cleavage, are immobilized onto a surface. Next, the substrate is placed into a vessel, and after purging with N_2, the deoxygenated solution containing a monomer, catalyst, ligand, and reducing agent is added. The substrates are kept in the sealed containers for a desired duration, then the polymerization is terminated by breaking the seal and exposing the solution to air[104]. The kinetics of polymerization can be fine-tuned by changing the ratios of solution components (e.g. Cu : ligand, Cu^I : Cu^{II}), types of ligand, initiator, or solvent[134].

Post-polymerization modification

Despite ongoing progress in coordination polymerization and CRP methods toward functional group tolerance, a multitude of side-chain functionalities still cannot be obtained by direct polymerization using any of the available techniques[129,139]. Some functional groups may either completely impede the polymerization process or participate in side reactions that render the polymerization reaction poorly controllable[139]. In such cases, polymerization of protected monomers presents a solution, but subsequent deprotection step may not proceed to completion and may also disrupt the integrity of the polymer structure[139]. In addition, due to elaborate synthesis and purification strategies and small yields, the cost of monomers with complex functional groups is prohibitive for certain applications[140]. To circumvent these issues, a two-stage process is employed, involving direct polymerization of monomers containing moieties that are inert toward polymerization conditions but can be quantitatively converted to a desired functionality in the subsequent step – "post-polymerization modification" (PPM)[33,139,141]. Moreover, PPM is a convenient method for systematic studies of structure-property relationships of functional polymers, as polymers bearing diverse pendant groups can be obtained from the same base polymer[33,139,141].

In this thesis, PPM was used in conjunction with SIP methods. For polymer films attached to substrates a high degree of conversion can be challenging due to the limitations in physiochemical stability of polymer-substrate bonds and mass transport of the reagents, steric hindrance effects, entropic constraints, etc[140]. Therefore, the monomers containing oxirane (glycidyl methacrylate (GMA)) and acid chloride (norbornene diacyl chloride (NBDAC)) moieties were chosen for polymerization via Si-ARGET ATRP (Chapter IV) and Si-ROMP (Chapter V), respectively. Both acid chlorides[32,33,142] and oxiranes[139,141] can react with numerous functional groups in mild conditions in a single-step and with high yield, thus presenting versatile platforms for preparation of functional polymer films through post-modification.

Functional groups in polymers

A functional group is an atom or a group of atoms that has similar characteristic reactivity and properties, regardless of its position and the rest of the chemical composition in any molecule or compound which contain it[143]. Functional groups determine the distinctive chemical and physical properties of families of organic compounds[143]. Functional polymers include functional groups in the main or side chains, and their type and concentration largely dictate the utility of these materials.

Metal-chelating functionalities

The introduction of specific functional groups into polymer chains makes them capable of forming chelate complexes with metal ions under certain favorable conditions[16]. All metals complex with molecules containing electron-rich centers, called "ligands" (e.g., H_2O, $–NH_2$ and $–CO_2^-$), which donate electrons to metal cations[144]. Chelation involves formation of two or more separate coordinate bonds between a polydentate ligand (multiple donor atoms) and a single metal ion[145]. Metal chelates, significantly more thermodynamically stable compared to analogous complexes containing monodentate ligands[145], are strong yet reversible, which is required for many applications. Chelating ligands most commonly include oxygen, nitrogen, and sulphur donor atoms[16,144].

Ligand selectivity toward specific metal ions is a key parameter in designing chelating polymers. As a starting point, Pearson's Hard and Soft Acids and Bases (HSAB) classification[146] is a useful qualitative tool for selection of donor atoms for chelating ligands. The term "hard" applies to species with small size, high charge states, which are weakly polarizable; in contrast "soft" species are big, have low charge states and are strongly polarizable[146,147]. According to the HSAB principle, hard Lewis acids bind preferentially with hard bases, whereas soft Lewis acids react faster and form more stable complexes with soft bases, all other factors being equal[147,148]. The examples of hard, soft, and borderline acids and bases

as originally classified by Pearson are given in the Table 2.1[146]. The table presents a useful starting point for ligand selection; however, a more sophisticated framework, e.g., considering steric efficiency of a ligand toward specific metal ions, is required for optimal ligand design[149].

Table 2.1. Classification of Lewis acids and bases according to Pearson's HSAB principle[146].

Type	Acids	Bases
Hard	H^+, Li^+, Na^+, K^+ Be^{2+}, Mg^{2+}, Ca^{2+}, Sr^{2+}, Ba^{2+}, Al^{3+}, Sc^{3+}, Ga^{3+}, In^{3+}, La^{3+} Gd^{3+}, Lu^{3+}, Cr^{3+}, Co^{3+}, Fe^{3+}, As^{3+}, Si^{4+}, Ti^{4+}, Zr^{4+}, Hf^{4+}, Th^{4+}, U^{4+}, Pu^{4+}, Ce^{4+}, Wo^{4+}, Sn^{4+}, UO^{2+}, VO^{2+}, MoO^{3+}	H_2O, OH^-, F^-, $CH_3CO_2^-$, PO_4^{3-} SO_4^{2-}, Cl^-, CO_3^{2-}, ClO_4^-, NO_3^-, ROH^-, RO^-, R_2O, NH_3, RNH_2, NH_2NH_2
Soft	Cu^+, Ag^+, Au^+, Ti^+, Hg^+ Pd^{2+}, Cd^{2+}, Pt^{2+} Hg^{2+}, $CH_3{}^+Hg$, $Co(CN)_5^{2-}$, Pt^{4+}, Te^{4+}, Br^+, I^+	R_2S, RSH, RS^-, I^-, SCN $S_2O_3^{2-}$, R_3P, R_3As, $(RO)_3P$, CN^-, RNC, CO, C_2H_4, H^-, R^-
Borderline	Fe^{2+}, Co^{2+}, Ni^{2+}, Cu^{2+}, Zn^{2+}, Pb^{2+}, Sn^{2+}, Sb^{3+}, Bi^{3+}, Rh^{3+}, Ir^{3+}, $B(CH_3)_3$	$C_6H_5NH_2$, C_5H_5N, N_3^-, Br^-, NO^{2-}, N_2, SO_3^{2-}

Catechol functional groups

Catechol (1,2-dihydroxybenzene) ligands can form stable complexes with various di- and, most efficiently, trivalent metal ions[150]. Catechols are recognized as the best bidentate chelators for Fe^{3+} with stability constants ranging from $\log K_1 = 20.01$ for mono- to $\log\beta = 43.76$ for triscatecholate complexes[151]

(Fig. 2.4). However, the affinity of catechols toward other trivalent ions is comparably high. For instance, the stability constants for mono-, bis-, and triscatecholate complexes with Al^{3+} are 16.3, 29.3 and 37, respectively[151]. The coordination mode (mono-, bis-, or tris-) of catechol ligands depends on the pH, as they exhibit high affinity to protons with pKa of the most acidic hydroxyl group ranging between ~6 – 10 depending on the electronic nature of the other substituents on the benzene ring[152–156]. Nonetheless, catechols are easily deprotonated in the presence of metal ions even in acidic conditions[154,156]. In addition to the pH, the stoichiometry of catechol complexes with metal cations is also controlled by the concentration of both the ion and the ligand[154,156].

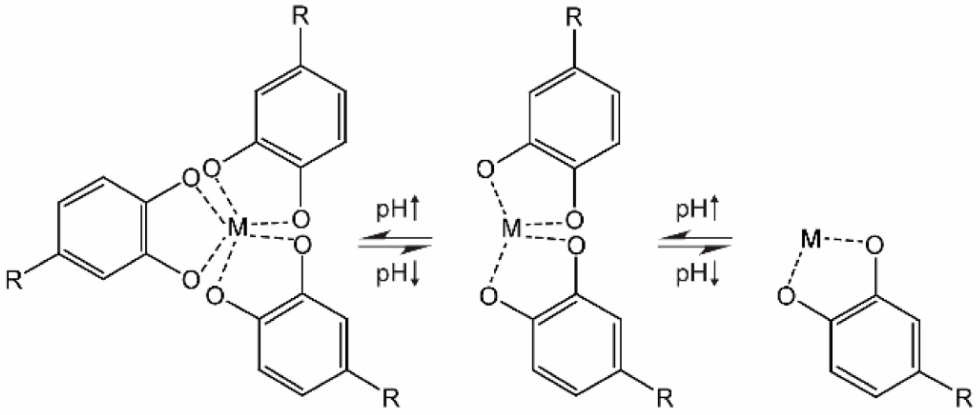

Figure 2.4. Schematic structure of tris-, bis-, and monocatecholate complexes with metal cations[157].

Besides metal chelation, incorporation of catechol moieties into polymers endows them with a broad range of functions[158–160]. Catechol-functionalized polymers can: 1) undergo reversible redox[161] in buffered/unbuffered aqueous media, and in aprotic solvents; 2) participate in various non-covalent interactions (hydrogen-bonding, π-π interactions, cation-π interactions)[158]; 3) oxidize to quinones and subsequently form covalent cross-links via phenol-radical coupling or tautomerization[162].

Chapter IV of this thesis describes a route for introduction of catechol functionality into pGMA films via PPM. Dopamine, which consists of a catechol group and an amine attached to it through an ethyl chain, was chosen as a modifying molecule due to its commercial availability at low cost in a form of shelf-stable hydrochloride salt.

Hydroxamic acid functional groups

Hydroxamic acid (HA) groups, bidentate ligands with two oxygen atoms as donors, have a lower affinity for metal ions than catechols, but also favor trivalent ions over divalent[144,163]. The major advantages of HAs over catechols is their stability to oxidation and lower sensitivity to pH of the medium[164]. The pKa values for HAs are in the range of 7 – 9[165]. Therefore, compared to catechols, the oxygen atom in HAs is more deprotonated at neutral pH and the predominant type of complexes in solution is tris (HA : metal = 3 : 1)[144]. Naturally, HAs chelate metal cations more efficiently with increasing pH; though complexation can occur at pH values as low as 2[163]. HA ligands and metal cations form 5-membered chelate rings, which are ~7 orders of magnitude more stable compared to analogous 4-membered rings formed by carboxylic acids (Fig. 2.5)[164].

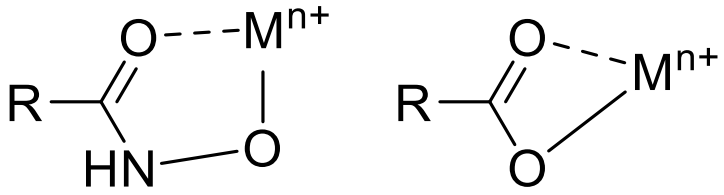

Figure 2.5. Schematic structure of metal ion complexes with bidentate HA (left) and carboxylic acid (right) ligands[164].

To date, the majority the polymers bearing HA functional groups reported in literature have been prepared using PPM with hydroxylamine from poly(methyl methacrylate)s and poly(acrylamide)s[164,166]. The degree of conversion to HA groups through these routs is moderate at best, and the harsh reaction conditions are incompatible with many applications (especially biomedical)[165]. Direct radical polymerization of monomers with unprotected HA groups was inhibited due to radical transfer to the HA moieties[164]. Recently, Johann et. al[165] reported synthesis of dioxazole-protected HAs containing hydroxyl moieties, and subsequent end-group functionalization of poly(ethylene glycol) chains using these molecules. The deprotection step involved treatment of the polymers with 0.1 HCl, which resulted in quantitative cleavage of dioxazole groups. These acidic conditions lead to degradation of the dioxazole structure, thus liberating the free hydroxamic functional PEG in quantitative yields. The same paper provides procedures for preparation of epoxide and methacrylate monomers from the synthesized hydroxyl functional dioxazole-protected HAs, but not yet their polymerization.

In Chapter V of this thesis, free-standing and tethered polymer films with two HA groups per repeat unit were prepared by ROMP of NBDAC and subsequent PPM with hydroxylamine in water at room temperature, which resulted in complete conversion of acid chlorides to hydroxamic acid within 20 h.

Chapter III

EXPERIMENTAL PROCEDURES AND CHARACTERIZATION METHODS

Experimental Procedures

Materials

Silicon (100) wafers were purchased from WRS Materials. Deionized (DI) water (≥ 5.0 MΩ) was purified using a Millipore Elix filtration system. Gold shot (99.99 %) and chromium-coated tungsten rods were obtained from J&J Materials and R.D. Mathis, respectively.

The following materials were purchased from Sigma-Aldrich and used as received: activated basic Brockmann I, aluminum oxide (alumina), N,N,N′,N″,N″-Pentamethyldiethylenetriamine (99%) (PMDETA), copper (II) bromide (99%), 5-norbornene-2-methanol (NBOH) (98%, mixture of endo and exo), hydroquinone (99%), dicyclopentadiene (DCPD) (containing BHT as stabilizer), thylenediaminetetraacetic acid disodium salt dihydrate (EDTA), 2,2,2-trifluoroethylamine hydrochloride (98%), 1-butyl-3-methyl-imidizolium-tetrafluoroborate ([BMIM]BF4), N,N-Dimethylformamide (anhydrous, 99.8%), toluene (anhydrous, 99.8%), triethylamine (anhydrous, ≥ 99.5%), DCM (anhydrous). [(5-Bicyclo[2.2.1]hept-2-enyl)ethyl]trichlorosilane ($NbSiCl_3$) and L-ascorbic acid were purchased from Tokyo Chemical Industry and used as received.

Glycidyl methacrylate (97%, containing 100 ppm of monomethyl ether hydroquinone inhibitor) was obtained from Sigma-Aldrich, and used immediately after removing the inhibitor by passing the monomer through a ~5cm-long activated alumina column.

Trans-3,6-endomethylene-1,2,3,6-tetrahydrophthaloyl chloride (97%) (NBDAC) was obtained from Sigma-Aldrich and purified via distillation at reduced pressure. Grubb's second-generation catalyst

[(H_2IMes)(PCy_3)($Cl)_2$Ru=CHPh] and 3-bromopyridine were used as received from Sigma-Aldrich to synthesize Grubb's third generation catalyst as described by Love et. al[167].

Bisphenol A/F based Super Sap CCR epoxy resin and the corresponding CCF fast hardener (polyoxypropylenediamine) were purchased from Entropy Resins and used as received.

The following chemicals were obtained from Fisher Scientific and used as received: dichloromethane (DCM), ethanol (200 Proof), toluene, sulfuric acid (95%), hydrogen peroxide (30%), (chloromethyl)phenyl trichlorosilane, (97%), dopamine hydrochloride (99%), hydroxylamine hydrochloride, iron (III) chloride (anhydrous, 98%), aluminum (III) chloride (anhydrous, 99%), zinc (II) chloride (anhydrous, 98%+), 1H,1H,2H-perfluoro-1-octene (99%), isopropylamine (99%), N,N-diethylethylenediamine (98+%), pyrrolidine (99%) (Alfa Aesar), copper foil (0.025 mm thick).

Silica-coated sensors QSX303 (quartz, 4.95 MHz, 14 mm diameter, polished, AT-cut with gold electrodes) for QCM-D studies were obtained from Nanoscience Instruments, Inc.

(Perfluorohexyl)norbornene (NBC_6F_{13}) monomer (used in Chapter V) was synthesized via a Diels-Alder reaction described by Perez et al[168]: a Parr Instrument high pressure reaction vessel was charged with molar ratios of 1H,1H,2H-perfluoro-1-octene : DCPD : hydroquinone (quenching agent) = 1 : 0.5 : 0.03. The reaction was held at 170 °C for 72 h. WARNING: *the contents of the reactor will be under high pressure – wait until the vessel cools down to room temperature before opening it to remove the products, handle with caution!* Next, the contents of the reaction vessel were distilled under reduced pressure and NBC_6F_{13} was collected as a clear liquid (~50% yield). The chemical structure and composition of the obtained monomer was confirmed by ^{1}H, ^{13}C, and ^{19}F NMR spectra collected in deuterated chloroform as a solvent, and the spectra are consistent with those reported by Faulkner et al.[127]: ^{1}HNMR($CDCl_3$): δ 6.2 (m) (1H), 6.0 (m) (1H), 3.2 (s) (1H), 2.9 (m) (1H), 2.8 (m) (1H), 2.0 (m) (1H), 1.5 (m) (1H), and 1.3 (m)

(2H); ^{19}F NMR ($CDCl_3$): δ -81.0 (s) (3F), -111.4 to 116.2 (m) (2F), -121.3 to -123.8 (m) (6F), -125.35 to -127.1 (m) (2F); ^{13}C NMR ($CDCl_3$) shifts for exo- end endo isomers are provided in the Table 3.1.

Table 3.1. ^{13}C NMR ($CDCl_3$) shifts for NBC_6F_{13}.

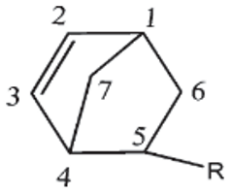

Isomer	^{13}C NMR δ (ppm)						
	C_1	C_2	C_3	C_4	C_5	C_6	C_7
exo	41.9	138.1	136.2	42.3	40.6	26.6	46.3
endo	41.1	137.1	131.6	43.5	40.7	27.4	49.5

Preparation of Si/SiO_2 substrates

Silicon wafers were cut into 2 cm × 1 cm substrates, rinsed with ethanol, water, and ethanol, dried in the stream of nitrogen, and soaked in 1:1, v/v mixture of ethanol and water for >16 h. The substrates were sonicated in the ethanol and water mixture for 30 min to displace any remaining contaminants, rinsed with ethanol and water, dried in the stream of nitrogen and immersed into a piranha solution (H_2SO_4/H_2O_2 =7:3, v/v) for 30 min (WARNING: *the mixture reacts violently with organic matter – should be handled with extreme caution!*) The substrates taken out of the piranha solution were washed thrice by submersion into di-water, rinsed with di-water, submersed into ethanol, then into toluene, rinsed with toluene, and dried in the stream of nitrogen.

Preparation of (chloromethyl)phenyl trichlorosilane monolayers on Si/SiO_2

Immidiately after piranha cleaning, the substrates were placed into 3mM solution of (chloromethyl)phenyl trichlorosilane initiator in anhydrous toluene for 2 h at room temperature to yield

surface-tethered monolayers. The substrates were then sonicated in toluene to remove any unbound material and baked at 100 °C for 5 h under vacuum.

Preparation of $NbSiCl_3$ monolayers on Si/SiO_2

Immediately after piranha cleaning, the substrates were placed into 5 mM solution $NbSiCl_3$ in anhydrous toluene for 1 h at room temperature to yield surface-tethered films. The substrates were then sonicated in toluene to remove any unbound material, and stored in a sealed container until further use.

Characterization Methods

Attenuated Total Reflectance–Fourier Transform Infra-Red (ATR–FTIR) Spectroscopy

IR (or vibrational) spectroscopy is a technique used to identify and study chemical substances based on absorption of electromagnetic radiation characteristic of their molecular structure[169,170]. The mid-IR region between wavenumbers of 4000 and 400 cm^{-1} is of primary interest for analysis of organic materials. An IR spectrum is represented in a graph of absorbance (or transmittance) in arbitrary units on the vertical axis vs. frequency in wavenumbers on the horizontal axis. The absorbance spectrum for the sample is calculated as follows[171]:

$$A = \log(I_0/I) \tag{3.1}$$

where A is absorbance, I_0 and I are intensity of the incident light and that transmitted by the sample, respectively. Absorption bands in the spectrum result from energy differences between vibrational states of the sample molecules relative to the background. The amplitudes of fundamental molecular vibrations increase upon absorption of IR radiation (as a result of change in the molecular dipole moment), so the intensity of the IR beam at the corresponding wavelength is decreased after interaction with the sample. The position of a particular absorption band depends on bond strength and the masses of the involved

atoms, and the corresponding absorbance is directly proportional to the number of bonds in the sample molecules responsible for that absorption[169].

FTIR spectroscopy allows collection of data at all frequencies simultaneously, improving both the speed of acquisition and signal-to-noise ratio[171]. The technique is based on the interference of two initially identical beams, one reflected from a fixed mirror and another from a moving mirror. The resulting interferogram is then converted from space domain into the frequency domain by applying a fast Fourier transform algorithm (automatically performed by the instrument's software).

In ATR-FTIR[172,173], the IR beam is passed through a crystal of an IR-transparent material with high refractive index (e.g. diamond, Ge, ZnSe) that is pressed against an optically less dense sample (Fig. 3.1). The incident angle, θ, (typically 45°) is greater than the critical angle ($\theta_c = \sin^{-1} n_{12}$, where n_{12} is the relative index of refraction of the crystal and the sample media), which leads to total internal reflection of the beam at the crystal to sample interface[174]. As the refractive index of the sample is lower than that of the crystal, a portion of the beam extends beyond the crystal's boundaries and penetrates the sample in a form of an evanescent wave. The depth of penetration, d_p, typically ranges between 0.5 and 5 μm, depending on the wavelength, n_{12}, and θ. For IR radiation wavelengths at which the sample absorbs, the reflected evanescent wave is attenuated. The reflected IR beam exits the crystal and is passed to the detector, as shown in Figure 3.1.

ATR-FTIR was employed to determine the composition of the various polymer films obtained in this work (Chapter IV, V), using Thermo Nicolet 6700 FT-IR Spectrometer equipped with a liquid-nitrogen cooled mercury-cadmium-telluride (MCT) detector and Smart iTR™ ATR attachment with a diamond crystal plate. The spectra were collected in the region of 4000 – 700 cm^{-1} over ~ 4 min (256 scans) at 2 cm^{-1} resolution and processed using OMNIC™ software.

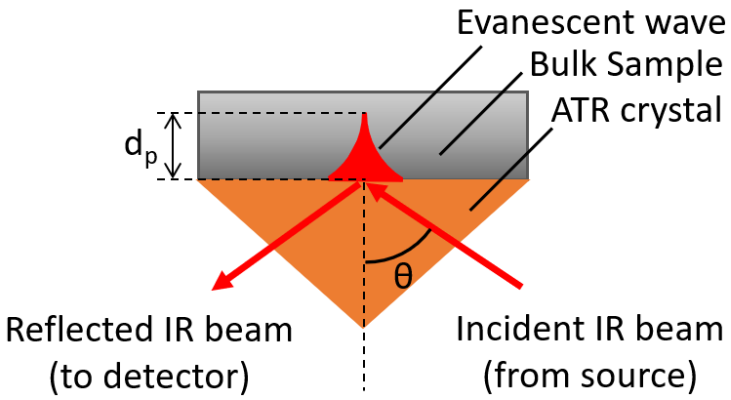

Figure 3.1. Schematic representation of the principle of ATR IR spectroscopy.

Contact Angle Goniometry

A contact angle is a quantitative measure of wetting of a solid by a liquid, defined as the angle between the solid surface horizontal under the liquid drop and the tangent to the liquid–vapor interface as it approaches the solid surface at the three-phase contact line (Fig. 3.2)[175]. The contact angle between liquid and an ideal (i.e., atomically smooth, homogeneous, non-reactive, and rigid) solid surface, resulting from the thermodynamic equilibrium of the drop under the action of the solid-vapor (γ_{sv}), solid-liquid (γ_{sl}), and liquid-vapor (γ_{lv}) interfacial free energies, is described by the Young equation:

$$\cos\theta_{Young} = \frac{\gamma_{sv}-\gamma_{sl}}{\gamma_{lv}} \tag{3.2}$$

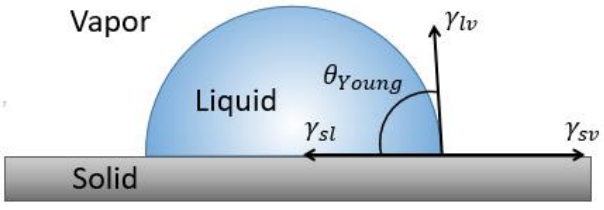

Figure 3.2. A drop of liquid on an ideal solid surface, illustrating the definition of the Young contact angle (θ_{Young}).

While the Young equation predicts a single equilibrium contact angle, experimentally a range of stable contact angles may be observed for a given solid surface[176]. The highest, "advancing", and the lowest, "receding", apparent contact angles can be measured by increasing and decreasing, respectively, the volume of the droplet, as shown in Figure 3.3. The difference between the advancing and receding contact angles ($\theta_a - \theta_r$), termed hysteresis (H), is primarily affected by surface roughness and/or chemical heterogenity[176], but can also result from absorbed impurities and rearrangement of the solid surface induced by the solvent.

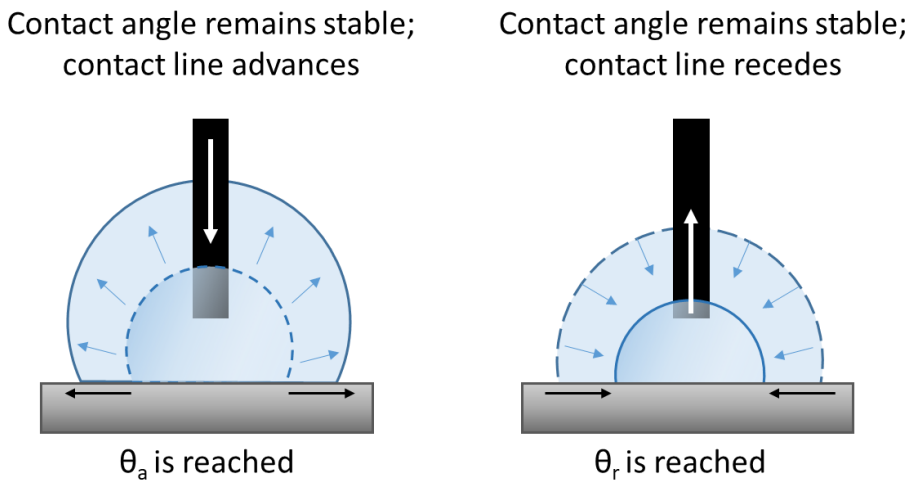

Figure 3.3. Schematics of advancing and receding contact angle measurement[175].

In this work, contact angle goniometry using deionized water as a liquid was employed to confirm the surface modifications by thiol and silane SAMs and to characterize the wetting properties of the synthesized polymer films (Chapter IV, V). Advancing and receding contact angles of ~ 5 μL water drops on the surfaces were measured at room temperature and ambient humidity using a Ramé-Hart manual goniometer with a microliter syringe. The tip of the syringe needle remained inside the probe droplets during measurements. The reported values and ranges represent the averages and standard deviations from at least three independently prepared samples. No fewer than three measurements per sample were

acquired, and the position of each measurement was varied to estimate the homogeneity of the sample and provide an average contact angle value representative of the whole surface.

Stylus Profilometry

Stylus profilometry[177] traces the topography of surfaces by physically moving a probe (a fine cone-shaped diamond stylus) laterally across the surface. The stylus is applied at a small load (less then mN), and the feedback loop is set to monitor the force from the sample features pushing up against the stylus as it scans. The change in the stylus height is detected by a displacement sensor as a function of position. The vertical resolution of the instrument is down to 10 nm, while the horizontal resolution is controlled by the scan speed and length.

In this thesis, profilometry was used to measure the thickness and roughness of films prepared by ROMP and spin-coating (Chapter V). The measurements were performed by Veeco Dektak 150 contact stylus profilometer with the stylus tip radius of 12.5 μm and applied force of 29.4 μN in the hills and valleys detection mode. The thicknesses of the films were estimated from three 1000-μm-long scans per sample across scratches manually introduced to establish baselines for uncoated substrates. The thickness was determined as the mean height variation for the polymer film from the bare substrate baseline, and the roughness of the polymer films was represented as the mean deviation of roughness profile (R_a). The scan results were plane fitted using the instrument's software. Reported values represent the averages and standard deviations of at least three independently prepared films.

Ellipsometry

Ellipsometry[178] is used to characterize thickness and optical constants of surfaces and thin films by measuring the change in polarization (amplitude ratio, Ψ, and the phase difference, Δ) of light reflected

or transmitted from them. The thickness of sub-nm- to a few-μm-thick films can be determined by interference between light reflected from the film surface and light transmitted through the film.

The main components of an ellipsometer include a light source, polarizer, polarization analyzer, sample stage, and detector (Fig. 3.4).

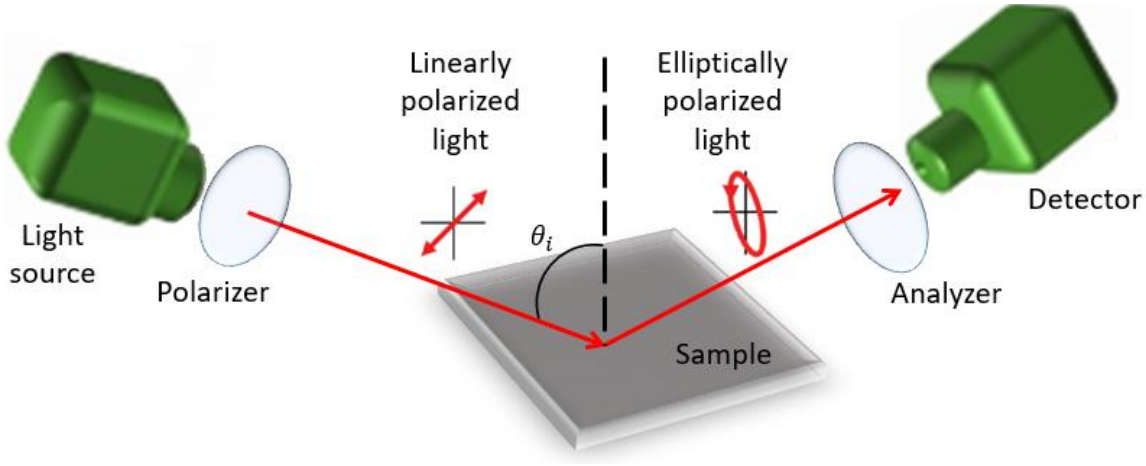

Figure 3.4. Schematic representation of a basic ellipsometry setup.

The unpolarized light generated by the source is sent through a polarizer, which allows light of a preferred electric field orientation to pass, resulting in the linearly polarized light incident on the sample surface[179]. The light reflected/transmitted from the sample becomes elliptically polarized and travels through another polarizer (acting as polarization state detector, i.e., analyzer), which permits variable amounts of light to pass onto the detector depending on the orientation of the polarizer relative to the electric field of the incoming beam. The detector converts the light into an electronic signal to determine the output polarization, which is compared to the known input polarization to determine the change in polarization resulting from the interaction of the light with the sample[179].

In this work, a J.A. Woollam M-2000VI variable angle spectroscopic ellipsometer was used to determine thicknesses of as-synthesized and modified pGMA films (Chapter IV). Thicknesses and refractive indices were obtained from fits to data taken at 60° and 70° angles of incidence. Optical constants and thicknesses of the underlying substrates with transparent thin films (Si wafers with a native oxide layer modified with silane SAMs or silica coated QCM crystals QSX303) were determined prior to the film growth and used in the subsequent data analysis. The thicknesses and optical parameters were obtained by regression analysis using an appropriate theoretical model for transparent or partially absorbent films. The best fit corresponds to the lowest root mean square error value between the measured data and the model.

The thicknesses of pGMA films deposited on silicon substrates were also determined using a Gaertner LSE ellipsometer (632.8 nm, incident angle = 70°). Data were processed using the Gaertner Ellipsometer Measurement Program. Relative thicknesses were calculated assuming an average refractive index of 1.5 for the multilayered films. Thicknesses were determined in at least three different standardized locations on each substrate and are presented as an average (with standard deviation) for each film, the thickness of native silicon oxide of 1.6 nm is subtracted from the values.

Electrochemical Impedance Spectroscopy (EIS)

EIS[180] enables investigation of ion transport through polymer films bound to electrodes and at the interfaces of the system. EIS is based on the perturbation of a system at equilibrium by a small alternating voltage (5 mV) applied over a range of frequencies (0.1 to 10^5 Hz), which allows one to examine different time scales within a single experiment[181]. The response (current at the same frequency but shifted in phase) is recorded. An expression analogous to Ohm's Law describes the complex impedance of the system[180]:

$$Z = \frac{V(t)}{I(t)} = \frac{V_A \sin(\omega t)}{I_A \sin(\omega t + \varphi)} = Z_A \frac{\sin(\omega t)}{\sin(\omega t + \varphi)}, \quad (3.2)$$

where *V(t)* is the applied potential at time t, *I(t)* is the corresponding response current signal, V_A and I_A are the amplitudes of the sinusoidal potential and current, respectively, ω is the radial frequency ($\omega = 2\pi f$, where f is the frequency in Hz), φ is the phase angle, and Z_A is the magnitude of the impedance.

Complex impedance (Z^*) is expressed as[180]:

$$Z^*(\omega) = Z' - jZ'' \tag{3.3}$$

where Z' is the real component and Z'' is the imaginary component. The impedance may also be expressed in an alternative form through its magnitude, $|Z|$, and phase angle, φ:

$$Z^*(\omega) = |Z|e^{j\varphi} \tag{3.4}$$

The EIS data representation as Bode plane (a plot of the phase angle and the logarithm of the impedance magnitude as a function of the logarithm of frequency) is convenient for analysis of polymer films: the impedance response at high frequencies is dominated by the electrolyte solution, the low frequencies correspond to the electrode/film interface, while the response at intermediate frequencies is often defined by resistive and capacitive effects of the polymer film itself.

In this work, EIS was employed for cure monitoring of epoxy/ionic liquid systems (Chapter VI), using the two-electrode setup depicted in Figure 3.5. All EIS measurements were performed on an a Gamry Instruments CMS300 electrochemical workstation at room temperature. During the testing procedure, the cell was placed in a Faraday cage in order to minimize Coulombic fields. EIS was conducted under sinusoidal 5 mV AC voltage over a frequency range of 10^{-1} to 10^5 Hz, with ten points per decade recorded. For quantitative data analysis, chemical and physical properties of a given system were reproduced with analogous electrical equivalent circuits (EEC) containing an appropriate combination of elements, using Gamry Echem Analyst software.

Quartz Crystal Microbalance with Dissipation (QCM-D)

QCM-D[182] is an ultrasensitive technique that can provide insight into molecular surface interactions in gaseous/liquid environments by monitoring the changes in resonant frequency (Δf) and energy dissipation (damping) (ΔD) of a freely oscillating piezoelectric quartz single crystal[183]. The QCM-D sensor crystal consists of a round, AT-cut piezoelectric quartz crystal with gold electrodes deposited onto the top and bottom surface of the quartz disc by evaporation[182].

During the measurement, an AC voltage is applied across the electrodes to induce the oscillations of the crystal at its resonant frequency. The driving voltage is periodically switched off, and the decay of the oscillation is monitored. Frequency and dissipation factor are determined by performing a fit (shown in red) to the decay (shown in blue) of the oscillatory amplitude over time (Fig. 3.6 a). If a viscoelastic film is applied to the surface of the crystal (Fig. 3.6 b), the frequency of the crystal's oscillation is reduced due to the added mass, but not in a linear fashion described by the Sauerbrey[184] equation. The accurate calculation of the viscoelastic mass requires measurement of both, the frequency and dissipation responses, which depend on the film properties, such as density, thickness, viscosity, and shear modulus[182].

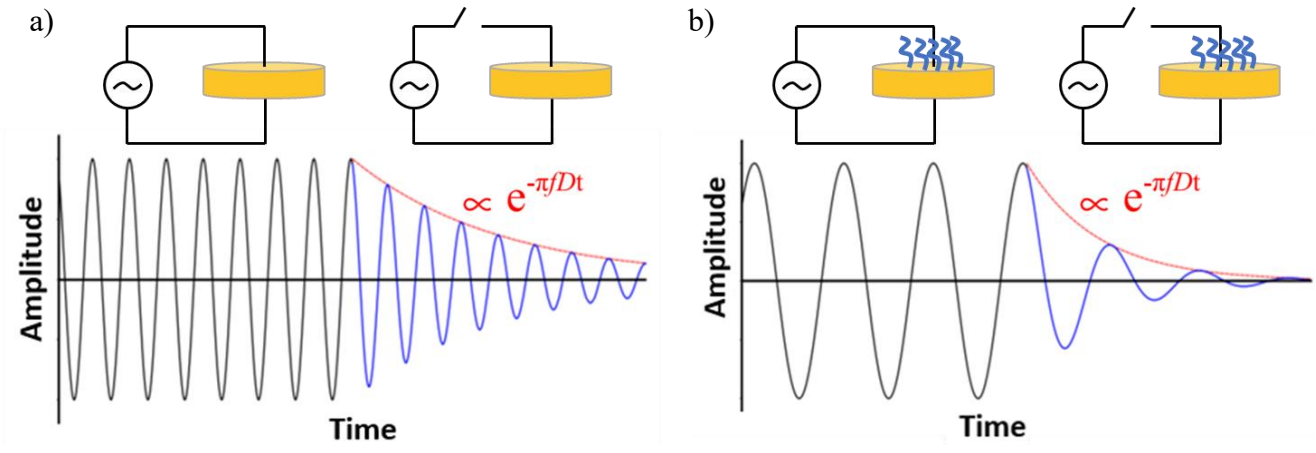

Figure 3.5. Schematics of QCM-D operation of a crystal: a) blank and b) with a viscoelastic coating.

The surface of quartz crystal electrodes can be modified with functional polymer films to obtain efficient sensors for a range of applications, including detection of metal ions[34,185] (Fig. 3.6 c). Real-time ion sensing is based on changes in mass and structural properties (e.g., cross-linking, swelling) of the polymer films upon exposure to the analyte. The mass of the absorbed ions as well as film properties are determined by applying a viscoelastic model[186] to the data.

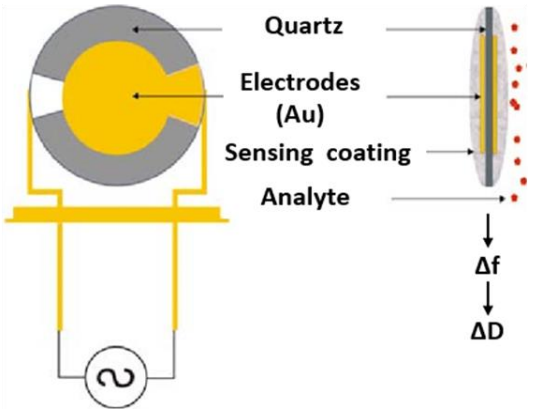

Figure 3.6. Illustration of polymer-coated QCM-D ion sensor.

In this thesis, dopamine-modified pGMA films (Chapter IV) were covalently immobilized onto QCM crystals and the measurements were obtained with Biolin Scientific Q-Sense E4 equipped with an Ismatec IPC peristaltic pump. Two types of experiments were performed:

1) Ex-situ characterization in air. A baseline for a blank crystal was established, and then, the response of the same polymer-coated crystal was measured to determine the thickness and viscoelastic properties of the deposited film in the dry state.
2) Real-time continuous measurements in aqueous media. The baseline signal for the films in flowing di-water was obtained, followed by monitoring the flow of measured media containing metal ions.

Initially, solutions with a single type of metal ion in concentrations ranging from 10^{-8} to 0.1 M were flowed until the response of the sensors reached a steady state. From these experiments, the response time, detection limit, and the trends in ion selectivity were established. The reversibility and reproducibility of the sensor response through at least 3 consecutive sorption/washing cycles was also studied. The ion-binding behavior of the films was modeled with appropriate sorption isotherms. Afterwards, a competitive ion sorption scenario using a mixture of metal ions commonly present in the target media was examined.

Differential Scanning Calorimetry (DSC)

DSC allows investigation of materials' phase transitions with temperature[187]. The technique measures the difference of heat absorption or release by a sample with respect to an inert reference as a function of time at constant temperature (isothermal mode) or as the temperature is increased/decreased at a certain rate (linear programmed mode)[188]. Based on measuring the enthalpy of exothermal cure reactions, DSC has become an industry standard for analysis of cure kinetics of epoxy resins[188,189].

In this thesis, measurements to characterize the cure kinetics of bisphenol A/F based epoxy - poly(oxypropylenediamine) hardener systems (Chapter VI) were performed with a TA Instruments Q200 DSC. Prior to each DSC test, a small amount of uncured epoxy (20 ± 3mg) was placed into a hermetic aluminum DSC pan and sealed with a lid. The sample was placed opposite to an empty reference pan in the DSC cell at a standby temperature of 25°C. The DSC cell was subsequently heated at a constant rate of 2, 5, 15, and 20 °C/min over a temperature range of 25 to 250 °C. The experiments were carried out under the constant flow of nitrogen at 50 mL/min. Measurements of the heat flow during the cure cycle were acquired and exported for further analysis.

Thermogravimetric Analysis (TGA)

TGA involves monitoring of the mass of a sample versus temperature or time in controlled inert (N_2) or oxidative (O_2, air) atmosphere[190]. The technique can provide information about phase transitions, oxidation, and thermal decomposition of the tested substance as well content of moisture, volatile and inorganic components in the sample. The key components of the thermogravimetric analyzer include a highly sensitive balance, which can measure the mass of samples of up to 1 g with 0.1 μg accuracy, microfurnace, heating chamber, temperature controller, gas feeding system, and data analyzer.

In this thesis, an Instrument Specialists TGA 1000 was used to characterize the thermal stability of free-standing polymer films described in the Chapter V. For each measurement, a sample was placed into a platinum heating pan and the mass of the sample was recorded prior to heating. Next, the temperature was increased from 25 °C to 900 °C at a constant rate of 10 °C/min and the % change in the sample mass were recorded. The measurements were conducted under the flow of nitrogen or air of 100 mL/min. In addition to the obtained mass change vs. temperature curves, the derivatives of the mass change $\frac{dm}{dt}$ vs. temperature were also calculated, which allows the point where weight loss is the most apparent as well as any overlapping thermal decomposition steps to be identified more clearly.

Ultraviolet–visible spectroscopy (UV-vis) Spectroscopy

UV-vis spectroscopy can be used for identification of compounds containing chromophores (i.e., molecules with valence electrons of low excitation energy) which absorb specific wavelengths of ultraviolet or visible light[169]. The absorption peaks in the UV-vis spectra correspond to the electronic transitions within the sample. The main components of a UV-vis spectrophotometer include a light source, a monochromator, and a detector. The monochromator houses an entrance slit (to narrow a beam of incoming light to a usable size), a dispersion device (usually a diffraction grating or prism that separates

polychromatic white light into bands of monochromatic light of a single wavelength), and an exit slit (to select the desired monochromatic wavelength).The instrument measures the amount of light transmitted through (or reflected from) a sample by ratioing the intensity of the incident light (I_0) to the intensity of the transmitted light (I), and the absorbance spectra are calculated as shown in equation 3.1 above. Using the Beer-Lambert law, the generated absorption spectra can be related directly to the concentration of the sample:

$$A = \log (I_0/I) = \varepsilon \cdot c \cdot l \tag{3.5}$$

where A is the measured absorbance (in arbitrary units (AU)), I_0 is the intensity of the incident light at a given wavelength, I is the transmitted intensity, l (in cm) the path length of the beam of light through the sample, and c the concentration of the absorbing species. For each species and wavelength, ε (in L/(mol·cm)) is a constant for a particular compound at a certain wavelength known as the molar absorptivity or extinction coefficient.

In this work, UV-vis spectroscopy using Varian Cary 5000 UV-VIS-NIR spectrophotometer was performed for determination of transition metal ions chelated by free-standing polymer films described in Chapter V.

Scanning Electron Microscopy with Energy-dispersive X-ray spectroscopy (SEM/EDS)

SEM allows for high-resolution (down to 1 – 20 nm) imaging of a sample by rastering a focused electron beam across the surface and detecting secondary or backscattered electron signal[191]. An EDS system integrated into an SEM instrument provides elemental identification and quantitative compositional information based on characteristic X-rays emitted by a sample upon excitation under the electron beam[192]. EDS detectors collect the photons as a function of their energy, and the photon intensity is analyzed to determine the chemical composition of the region of the sample under investigation. The

energy resolution of a typical commercial EDS system is limited to ~125 eV, which can result in overlap of the characteristic peaks in the X-ray signal generated by different chemical constituents in the sample[191].

In this work, SEM/EDS was employed for morphological and elemental analyses of epoxy-amine networks modified with 5, 10, 20, and 40 wt.% of [BMIM]BF_4 ionic liquid (Chapter VI). Prior to the analyses, the samples were sputter coated with Au to eliminate charging issues. SEM images were taken with a Zeiss Merlin Scanning Electron Microscope using an accelerating voltage of 10 kV, a working distance of 8.5 mm, and the HE-SE2 secondary electron detector. EDS spectra were collected using Oxford Instruments Silicon Drift Detector at the conditions specified above, and the data were analyzed using Aztec software.

Chapter IV

SURFACE-INITIATED, CATECHOL-CONTAINING POLYMER FILMS FOR EFFECTIVE CHELATION OF ALUMINUM IONS

Introduction

Molecules containing catechol (1,2-dihydroxybenzene) moieties are ubiquitous in nature. Catechol derivatives serve as essential neurotransmitters[193] and antioxidants[194], impart superior underwater adhesion properties to mussel byssus[195–197], and enable living organisms (e.g. bacteria) to scavenge iron from the surrounding environment[198], to name a few examples. Inspired by the utility and versatility of catechols observed in nature, researchers seek to incorporate catechol functional groups into synthetic polymers[158–160] to obtain advanced stimuli-responsive materials[199,200], adhesives[201], antimicrobial[202] and antifouling coatings[203,204], and metal-binding ligands[152].

Due to their outstanding metal complexing properties, polymers containing catechol groups have been applied for preconcentration and separation of metal ions[205–209] (including Fe^{3+}, Cr^{6+}, Cr^{3+}, Ni^{2+}, Zn^{2+}, Cu^{2+}, Cu^{+}, Cd^{2+}, Mn^{2+} and Pb^{2+}, lanthanides[210,211]), radionuclides[212,213], and germanium[214]. Aluminum is the third most abundant element found in earth's crust, and occurs naturally in the air, water, and soil as a persistent contaminant that cannot be fully biodegraded[215]. During the first half of the twentieth century, Al emerged as a crucial material in the transportation, aeronautics, electrical, construction, and other industries. Moreover, Al became ubiquitous in food products, medicine, animal feed, and consumer goods from packaging to cosmetics[216,217]. Mining and processing of Al increasingly contributes to the excess release of this metal into the environment, while recent investigations into its toxicity revealed that overabundance of Al presents a grave threat for the health of humans[217], animals[215], and plants[218]. Thus, catechol-containing polymers are of interest for enhancing removal, preconcentration, and detection of Al^{3+} ions.

In addition, sensing of metal ions using catechol ligands (for analyte binding) tethered to the surface of membranes[219] and carbon nanotubes[220] has been reported. Chelates of catechol-containing polymers with various metal ions account for an array of materials with unique properties, which can be employed, for instance, as self-healing, pH-responsive hydrogels[221–223], toughening elastomers[224], and hydrogel actuators[225].

The key strategies for obtaining catechol-functionalized polymers include attachment of catechol derivatives to existing polymer chains though reaction between complementary functional groups in the molecule and polymer (i.e. post-polymerization modification) and direct polymerization of catechol monomers[158]. In both cases, proper protection of catechol groups is often required[226]. The protecting groups must be stable under the reaction conditions and their subsequent removal (deprotection) should proceed to quantitative yields and have no adverse effect on the properties of the resulting polymer[226].

In this chapter, the author reports the introduction of catechol functionality into surface-grafted poly(glycidyl methacrylate) (pGMA) films, prepared by activator regenerated by electron transfer atom transfer radical polymerization (ARGET ATRP), through post-polymerization modification. I chose dopamine, which consists of a catechol group and an amine attached to it through an ethyl chain, as a modifying molecule due to its commercial availability at low cost in the form of shelf-stable hydrochloride salt. Currently, the predominant strategies to covalently bind dopamine to polymers or other surfaces involve protection and deprotection steps for the catechol group in dopamine and/or standard carbodiimide coupling of the amine to a carboxylic acid group on the surface[202,219]. We demonstrate high degree of functionalization of pGMA films with dopamine in a single step, with a tunable percent of modification depending on the duration of the reaction. In addition, we investigate the affinity of the resulting films to Al^{3+} and Zn^{2+} ions using quartz crystal microbalance with dissipation (QCM-D)[34].

Experimental Methods

Preparation of substrates functionalized with ATRP initiator

Silicon wafers were prepared and, subsequently, the initiator SAMs were deposited according to the procedure described in Chapter III.

QCM-D sensors (and Si substrates used as controls for the subsequent pGMA growth on the sensors) were placed into UV/ozone cleaner (Jelight M42) for 10 min, rinsed with water, ethanol, and toluene, dried in the stream of nitrogen, and placed into the silane initiator solution in anhydrous toluene for 2 h at room temperature. Next, the substrates were sonicated in toluene to remove any physically adsorbed material.

Preparation of pGMA Films by Si-ARGET ATRP

The reaction was performed in a solution containing purified GMA monomer, CuBr2 catalyst, PMDETA ligand, and reducing agent (ascorbic acid) with molar ratios of 5000:1:10:20, respectively, in an ethanol/water (4:1 v/v) mixture as a solvent. The substrates functionalized with initiator SAMs were placed into glass vials and sealed with rubber septa. A sealed round bottom flask, containing GMA and ascorbic acid in ethanol/water, and the vials with samples were purged with N_2 for at least 30 min to displace oxygen. The ethanoic solution of $CuBr_2$ and PMDETA was then added to the reaction mixture via syringe and allowed to purge for an additional 5 min. Next, ~5 mL of solution was transferred into each vial via syringe. The vials were sonicated for ~10 s to displace any gas bubbles from the surfaces of the substrates and placed in the dark for the desired duration (1– 24 h) at room temperature. Then, the polymerization was terminated by breaking the seal and exposing the solution to air[227]. The substrates were rinsed with ethanol and water, and sonicated in the ethanol/water mixture for 15 min to remove any physically adsorbed polymer. For control, pGMA films were also grown on Si/SiO_2 substrates with the initiator SAMs prepared by the simplified procedure used for QCM-D sensors. These films were of

comparable quality and thickness to the films obtained using piranha-cleaned substrates functionalized with thermally annealed SAMs.

Post-polymerization modification of pGMA with dopamine

After characterization, the obtained pGMA films on silicon were rinsed with water, ethanol, and DMF, dried in the stream of N_2, and placed into two-neck round bottom flasks equipped with water-cooled condensers and a nitrogen bubbler. The solutions of 0.1 M dopamine hydrochloride and triethylamine in anhydrous DMF were prepared, and the containers sealed with rubber septa. The vessels with the reaction solutions and the pGMA-coated substrates were purged with N_2 for 30 min. Then, the dopamine hydrochloride solution was injected into the flasks containing the substrates, and the triethylamine solution (1.5 molar equivalent of triethylamine to dopamine hydrochloride) was added to each flask, using a separate syringe. The flasks were capped with glass stoppers, immersed into a pre-heated oil bath, and maintained at 53 ± 3 °C for up to 190 h under nitrogen atmosphere. The samples were removed from the flasks at predetermined time intervals for characterization.

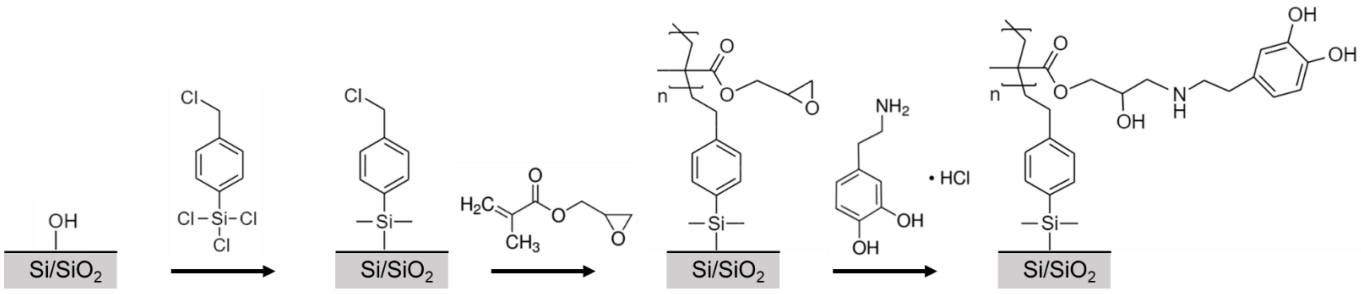

Figure 4.1. Preparation and post-polymerization modification of pGMA films.

Characterization

The thicknesses of the initiator SAMs, pGMA, and dopamine-modified pGMA films on silicon substrates were determined using a Gaertner LSE ellipsometer according to the procedure described in

Chapter III. A J.A. Woollam M-2000VI variable angle spectroscopic ellipsometer was used to determine the thickness of the films deposited on QCM-D sensors. Thicknesses and refractive indices were obtained from fits to data taken at 60° and 70° angles of incidence. The optical properties of blank QCM-D sensors were determined prior to the film growth and used in the subsequent data analysis[228]. The film thicknesses and optical parameters were obtained by regression analysis (CompleteEase software) by applying appropriate theoretical models. The best fit corresponds to the lowest root mean square error value between the measured data and the model. The optical properties of the blank QCM-D (QSX303) sensors (Fig. 4.2) were parametrized: quartz substrate, ~10-nm-thick chromium adhesion layer, ~100-nm-thick gold layer, and ~10-nm-thick titanium layer were modelled with B-splines, and a ~50-nm-thick silica top coating was modelled by Cauchy dispersion $n(\lambda) = A + B/\lambda^2 + C/\lambda^4$, where A = 1.451, B =0.049, C = -0.0001. The thickness of the deposited polymer films was determined by regression analysis using the data obtained for the blank sensor substrates (as fixed values) and a Cauchy model for a transparent film ($n(\lambda) = A + B/\lambda^2$, where A = 1.5 and B = 0.01).

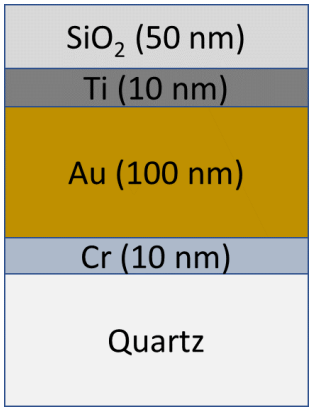

Figure 4.2. Layers of the standard QSX303 QCM-D sensor.

Water contact angle goniometry was conducted according the procedure provided in the Chapter III to confirm the surface modifications by the initiator SAMs (Table 4.1) and to characterize the wetting properties of the polymer films (discussed below).

The chemical composition of pGMA and dopamine-modified pGMA films was analyzed by attenuated total reflectance Fourier transform infrared spectroscopy (ATR-FTIR) using Thermo Nicolet 6700 FT-IR Spectrometer (see Chapter III for details).

The QCM-D measurements were obtained with Biolin Scientific Q-Sense E4 equipped with an Ismatec IPC peristaltic pump. Two types of experiments were performed. First, for ex-situ characterization in air, a baseline for a blank crystal was established, and then, the shifts in resonant frequency and dissipation of the same crystal after deposition of pGMA films and after their modification with dopamine were measured to determine the thickness and viscoelastic properties of the films in the dry state. Second, for real-time continuous measurements in aqueous media, the baseline signal for the films in flowing di-water was obtained, followed by measurements during the flow of solutions containing metal ions. To determine the thicknesses of the films before and after the modification (in air), as well as the mass of ions absorbed into the films (in aqueous solutions), shifts in frequency and dissipation of the odd overtones (j = 3,5,7,9,11) were modeled using the QTools™ software. The Voigt-Voinova model for one homogeneous viscoelastic layer with a fixed density of 1.25 g/cm^3 was applied, and the tabulated values for fluid viscosity and density of the appropriate medium (air or water) at 23 °C were inputted as fixed parameters.

Ion sorption isotherm data modeling

The pseudo-equilibrium values for mass of ions retained within the dopamine-pGMA films during QCM-D experiments were calculated by the Voigt-Voinova model for ion concentrations of 10^{-4} – 0.1 M.

The data were fitted to the Freundlich equilibrium model using Curve Fitting Toolbox™ in MATLAB software.

Results and Discussion

For each experiment, before proceeding to the polymer film synthesis, the quality of the deposited initiator monolayers was evaluated (Table 4.1). The procedure used in this work yielded consistent results: the thickness of the monolayers was slightly higher than the theoretical estimate based on the average C–C bond length of 0.142 nm, likely due to the silane undergoing vertical polymerization. The samples typically exhibited low water contact angle hysteresis values (< 25°), which is indicative of largely uniform surface coverage with the monolayers.

Table 4.1. Properties of the (chloromethyl)phenyl trichlorosilane-modified Si substrates.

Ellipsometric thickness, nm	Water contact angle, °	
	Advancing (θ_A)	Receding (θ_R)
2.0 ± 0.6	86 ± 4	61 ± 7

Polymer Film Growth

Si-ARGET ATRP of GMA yielded uniform, smooth polymer films with thicknesses reaching ~200 nm after 24 h of polymerization (Fig. 4.3). Although the pGMA films are transparent (n = 1.5), the substrates showed characteristic colors, depending on the thickness of the deposited film, due to the interference effect[229]. During the initial 4 h, polymerization appears to be well controlled, as evident from a nearly linear increase of the thickness with time[230] until the asymptotic thickness is reached. The decrease in polymerization rate observed for longer durations is likely caused by chain transfer into the solution[231], which became more viscous and opaque.

The chemical composition of pGMA films was confirmed by ATR-FTIR (Fig. 4.4). The spectrum shows characteristic absorption bands due to υ_s-C=O of the ester (1727 cm^{-1}), symmetric (863 cm^{-1}) and asymmetric (908 cm^{-1}) deformation of the oxirane ring, υ_s-C−H (2995 cm^{-1}) and υ_{as}-C−H (3058 cm^{-1}) of the oxirane[232].

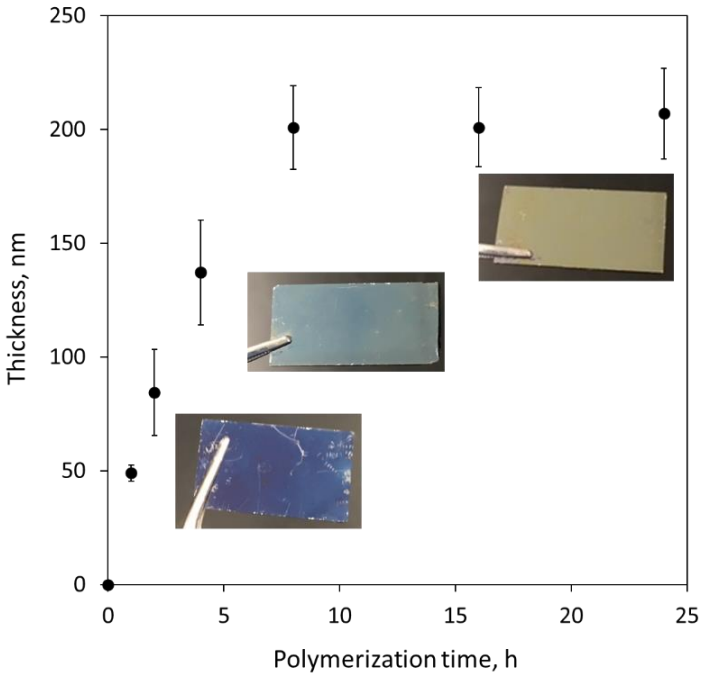

Figure 4.3. Thickness of pGMA films at different times of polymerization.

Data points and error bars represent the average and standard deviation, respectively, from 5 or more independent experiments. Photos of pGMA films on Si/SiO_2, film thicknesses (bottom to top): ~100 nm, ~155 nm, ~200 nm

Post-polymerization modification

The reaction of pGMA with dopamine results in the opening of the oxirane ring to yield the attached dopamine group, which is evidenced by the appearance of a broad band (3100 – 3600 cm^{-1}) in the FTIR spectra of modified films indicative of O-H and N-H stretching (Fig. 4.4). The intensity of the oxirane absorbance peak at 908 cm^{-1} diminishes, corresponding to the extent of post-polymerization

conversion, while the peak due to the ester carbonyl at 1727 cm^{-1} should remain unaffected (however slight broadening of the peak is observed with the progression of modification due to increased propensity for inter- and intrachain hydrogen bonding[233] upon ring opening of the oxirane groups and introduction of the catechol moieties). The area under the OH and NH stretching peaks increased with the increased duration of modification. To rule out conversion of oxirane due to hydrolysis, control samples were analyzed: pGMA films were unreactive in similar conditions (in the solution of triethylamine in DMF at ~50 °C for > 100 h) when no dopamine was added, as evidenced by the identical ATR-FTIR spectra before and after the reaction and unaltered film thickness (Fig. 4.5). No broadening of the carbonyl peak was observed in control samples.

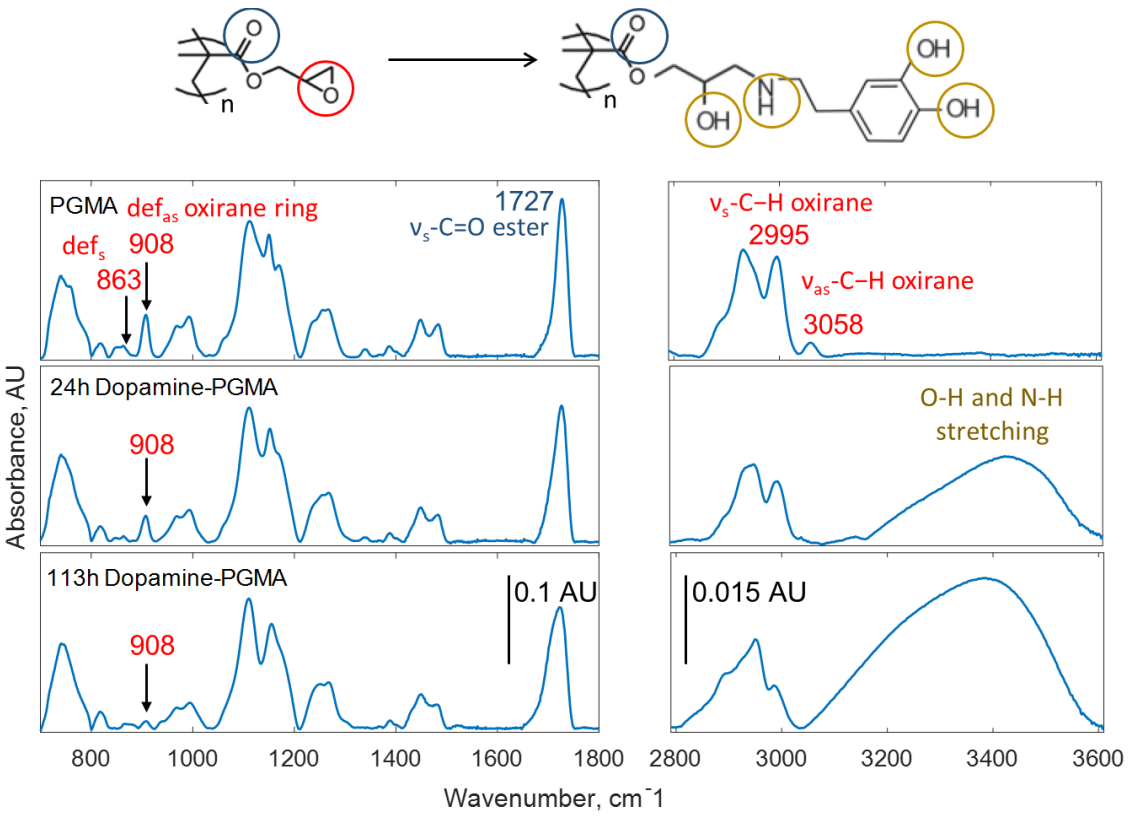

Figure 4.4. ATR-FTIR spectra of ~190-nm-thick pGMA film and the same film after 24 and 113 h of exposure to the post-modification reaction solution.

The wetting properties of pGMA films were examined before and after the modification. The measured advancing (θ_A) and receding (θ_R) water contact angles for as-synthesized pGMA, 60°±3 and 42°±3, respectively, are consistent with previously reported values[234]. No change in the θ_A values was observed after the reaction with dopamine, which is not unexpected as the reported values for dopamine-modified surfaces[235,236] are similar. The θ_R, however, decreased to <5°. Such a dramatic increase in contact angle hysteresis is likely a result of increased chemical heterogeneity after the modification and/or water intrusion into the film. Fox example, the water droplet dispensed for the θ_A measurement could saturate the modified film (due to its enhanced propensity for hydrogen bonding), and, subsequently, when the θ_R is measured, the three-phase contact line recedes to the position of water-saturated polymer, resulting in low observed θ_R values.

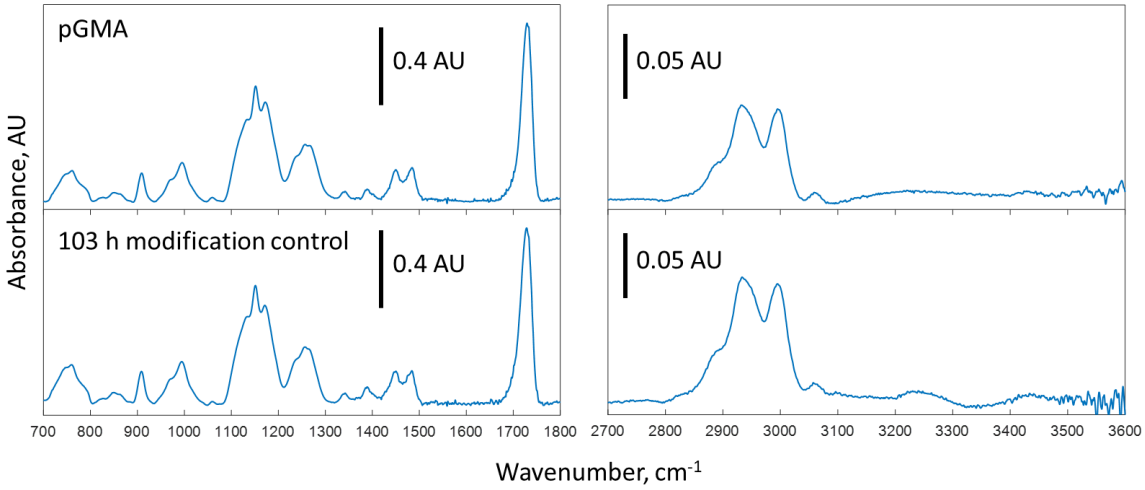

Figure 4.5. Normalized ATR-FTIR spectra of a 224-nm-thick pGMA film before and after 103-h-long exposure to the DMF and triethylamine reaction solution with no dopamine added. No change in the spectra and sample thickness was observed.

To estimate the extent of oxirane group conversion, the area under the oxirane peak relative to the area under the carbonyl peak was compared before and after the reaction[234] (see Fig. 4.4). The extent of oxirane group conversion was calculated by[234]:

$$\% \, Conversion = 100 - \left(\frac{A_{908,t}}{A_{1727,t}} / \frac{A_{908,t_0}}{A_{1727,t_0}}\right) \quad (4.1)$$

where $A_{908,0}$ and $A_{908,t}$ are the areas under the oxirane peak at 908 cm^{-1}, $A_{1727,0}$ and $A_{1727,t}$ are the areas under the carbonyl peak at 1727 cm^{-1} observed in unmodified films and the films after the *t* h of modification, respectively.

Figure 4.6 shows the kinetics of modification of pGMA films, in which the extent of modification was determined using Eq (1). The modification of up to 100-nm-thick films proceeded to completion, while ~10 – 20% of oxirane groups in ~200-nm-thick films remained unmodified even after increasing the duration of the reaction to more than a week. This result suggests that the reaction of dopamine with the oxirane groups becomes limited by diffusional access of the dopamine molecules to oxirane sites well below the outer surface of the film.

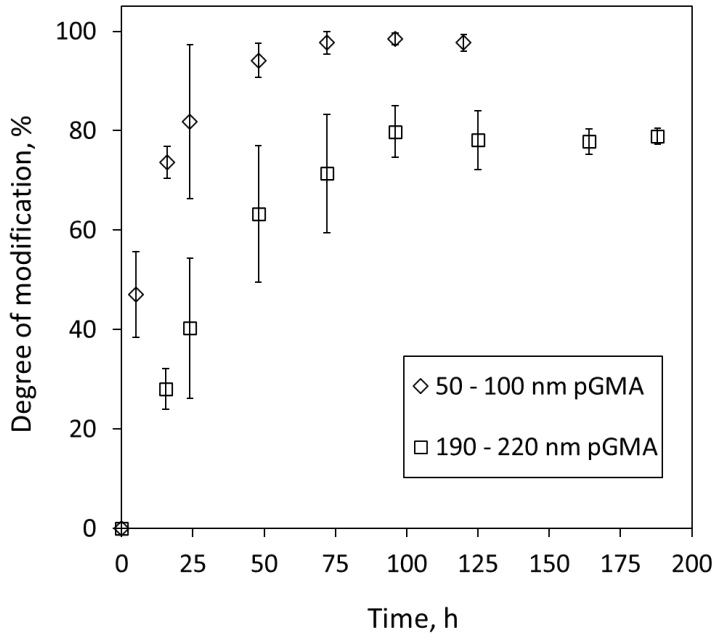

Figure 4.6. Kinetics of pGMA modification with dopamine. Datapoints and error bars represent average values and standard deviations from at least 3 independently prepared films.

Assuming that 80% of the oxiranes reacted with dopamine (Figure 4.6) and the increase in film thickness is proportional to the molecular volume of the repeat unit (determined using molinspiration.com), an increase in thickness of ~66% would be expected for the 80% conversion. However, the average increase of ellipsometric thickness was only 31(± 6) % for ~200-nm-thick pGMA films modified to 80 (± 4) % conversion (average and standard deviations based on 26 samples). As a possible explanation of the lower-than-expected thickness increase, some amines may have reacted with more than one oxirane group, resulting in tertiary amine intra-and interchain cross-links[231]. The increased steric hindrance could prevent the access of new dopamine molecules to unreacted oxirane groups at the later stages of modification, while the close proximity of the neighboring oxiranes within the dense pGMA films would facilitate cross-linking.

We also analyzed the thickness and viscoelastic properties of the pGMA and dopamine-modified pGMA films using the QCM-D technique. The deposition of pGMA and subsequent modification of the films with dopamine were performed ex-situ, and the shifts in resonant frequency and dissipation of the modified QCM crystals were recorded in air after each step (Fig. 4.7). From these data, the thicknesses of the pGMA and dopamine-pGMA films were determined using the Voigt viscoelastic model. In addition, the thicknesses of the films on QCM crystals were determined by spectroscopic ellipsometry. The values obtained for the film thicknesses and percent increase in thickness upon modification, as well as the degree of modification estimated from FTIR spectra (Fig. 4.8) using eq. 1 above, are presented in Table 4.2. Based on eight independently prepared QCM sensors with an average degree of modification of 94 ± 2% as determined by FTIR, the average increase in film thickness after modification by QCM-D is 22 ± 4 %, which is in good agreement with that obtained from ellipsometry at 24 ± 5 % for the same sensors.

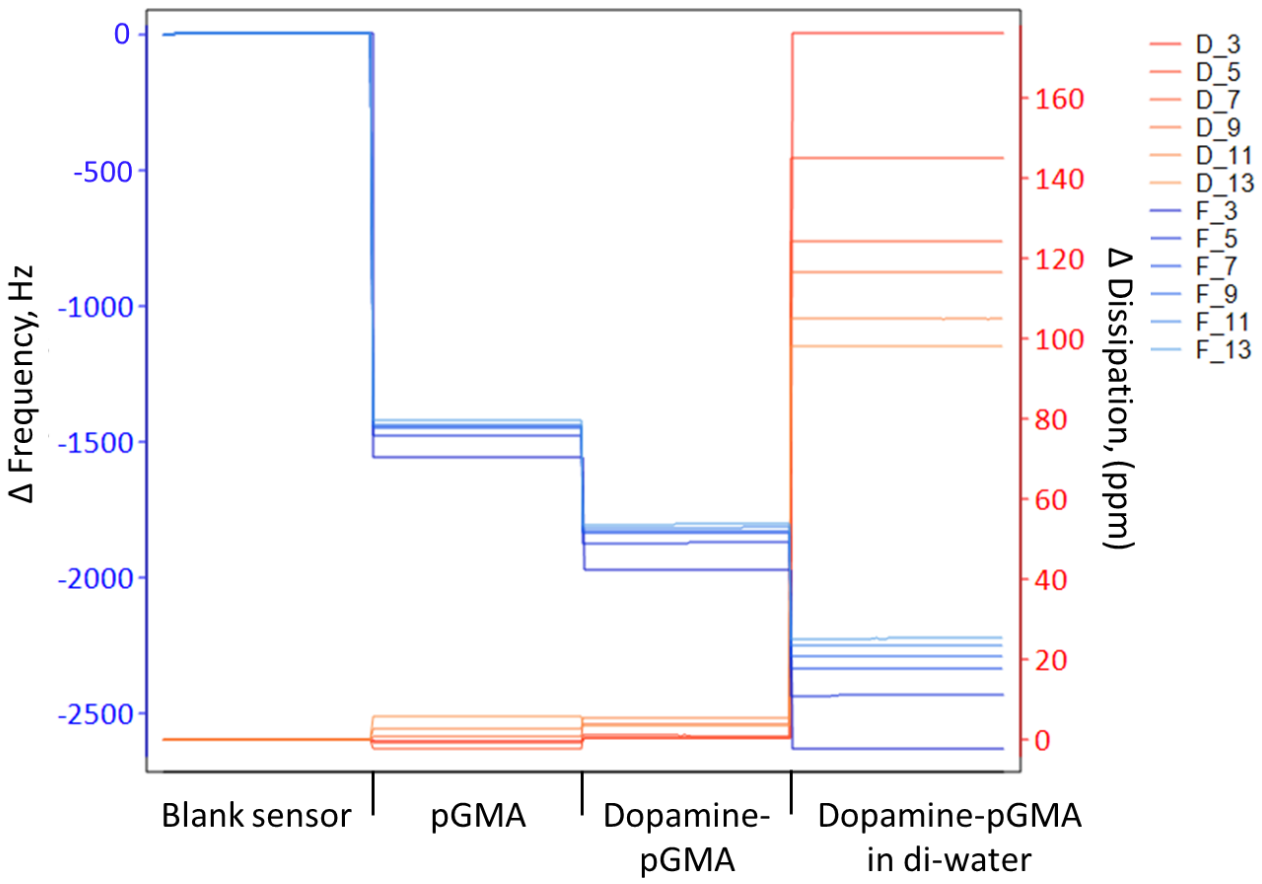

Figure 4.7. Changes in frequency and dissipation (3^{rd} – 13^{th} overtones) of a QCM-D sensor upon deposition of a pGMA film and its subsequent modification with dopamine (measured in air). The decrease in frequency upon film deposition and modification is due to the added mass. The spread in the frequency and dissipation shifts for different overtones are indicative of non-rigid character of the films. As di-water is flowed into the QCM-chamber, the increase in frequency and dissipation is observed due to swelling of the film.

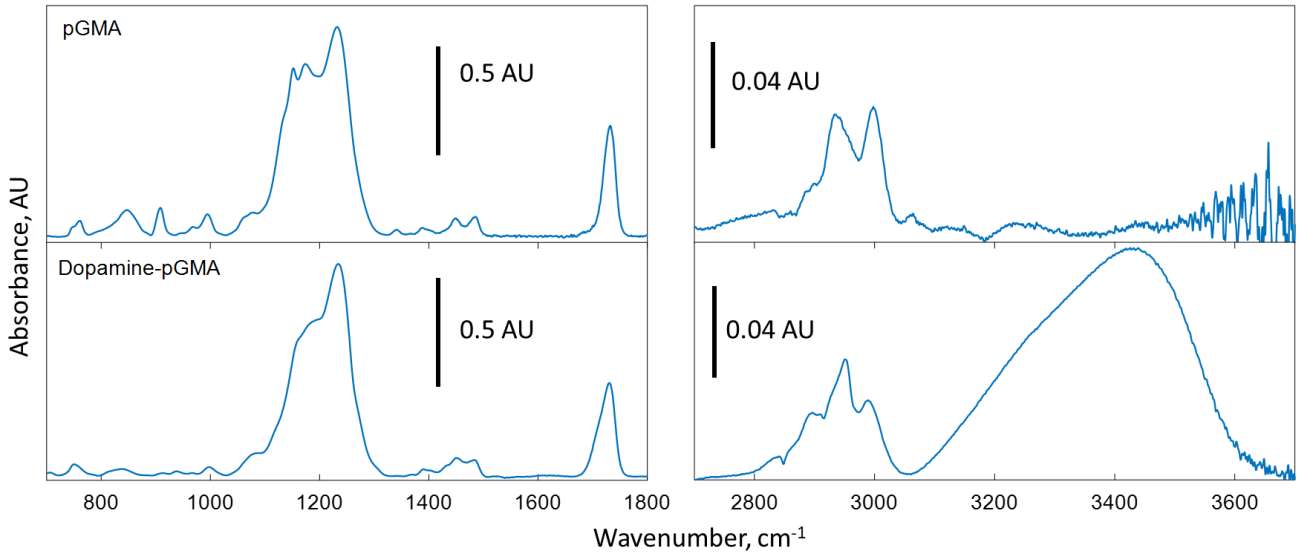

Figure 4.8. Normalized ATR-FTIR spectra of a 207-nm-thick pGMA film on a QCM-D sensor before and after 96-h-long exposure to the modification reaction solution. The degree of modification calculated using eq. 1 is 95%.

Table 4.2. Thickness of the films deposited onto QCM-D sensors as measured by ellipsometry and determined from QCM-D data modeling (Voigt viscoelastic model).

Sample	% modification (from FTIR)	Ellipsometric thickness, nm			QCM-D thickness, nm (from Voigt model)		
		pGMA	Dopamine-pGMA	% increase	pGMA	Dopamine-pGMA	% increase
1	95	193	231	20	213	246	15
2	95	184	235	28	202	252	25
3	95	207	245	18	222	268	21
4	95	211	254	20	221	261	18
5	98	200	246	23	209	264	26
6	91	227	297	31	231	287	24
7	92	234	298	27	237	280	18
8	94	239	294	23	233	289	24

Chelation Studies

We evaluated the sorption of Al^{3+} and Zn^{2+} ions by the dopamine-modified pGMA films via continuous flow QCM-D measurements. Figure 4.9 demonstrates an example of the shifts in resonant frequency and dissipation typically observed for sensors coated with dopamine-pGMA films when the 10^{-4} – 0.1 M aqueous solutions of $AlCl_3$ were flowed into the QCM-D cell. With increasing concentration of $AlCl_3$, the resonance frequency decreases and the dissipation increases. The observed response is primarily a mass loading effect, as the changes in resonant frequency (Δf) are substantial, while the shifts in dissipation per Δf are low[34]. Notably, simply by flowing di water though the cell, the desorption of ions was achieved, which is advantageous for regeneration of the films and recovery of sorbed metal ions. To ascertain that the ion uptake was enhanced by modification of pGMA with dopamine, we simultaneously measured the response of a sensor coated with an unmodified pGMA film (Fig. 4.10). In response to 0.1 M $AlCl_3$, a shift in resonant frequency of only ~20 Hz was observed. However, the shifts in dissipation were quite similar to the sensors coated with dopamine-pGMA, which indicates that the dissipation measurement was primarily affected by the properties of the solution flowed through the chamber as the viscosity of the ion solution increases with an increase in solute concentration (this is termed "bulk effect"[237]).

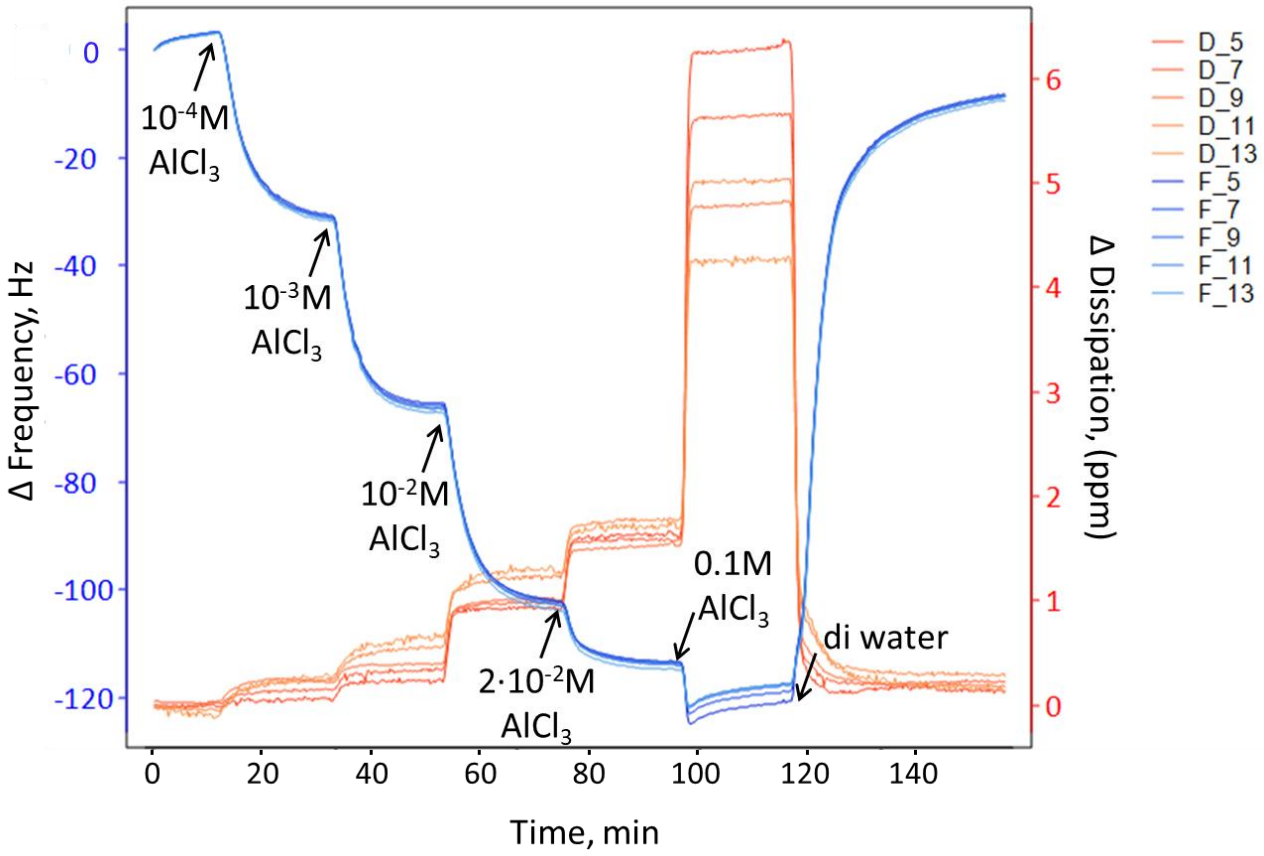

Figure 4.9. Typical response (changes in frequency and dissipation (5th – 13th overtones)) of a QCM-D sensor coated with a 297-nm-thick dopamine-pGMA film to various concentrations of $AlCl_3$. The sensor was equilibrated in di water (pH 5.5) prior to the flow of the Al ion solutions.

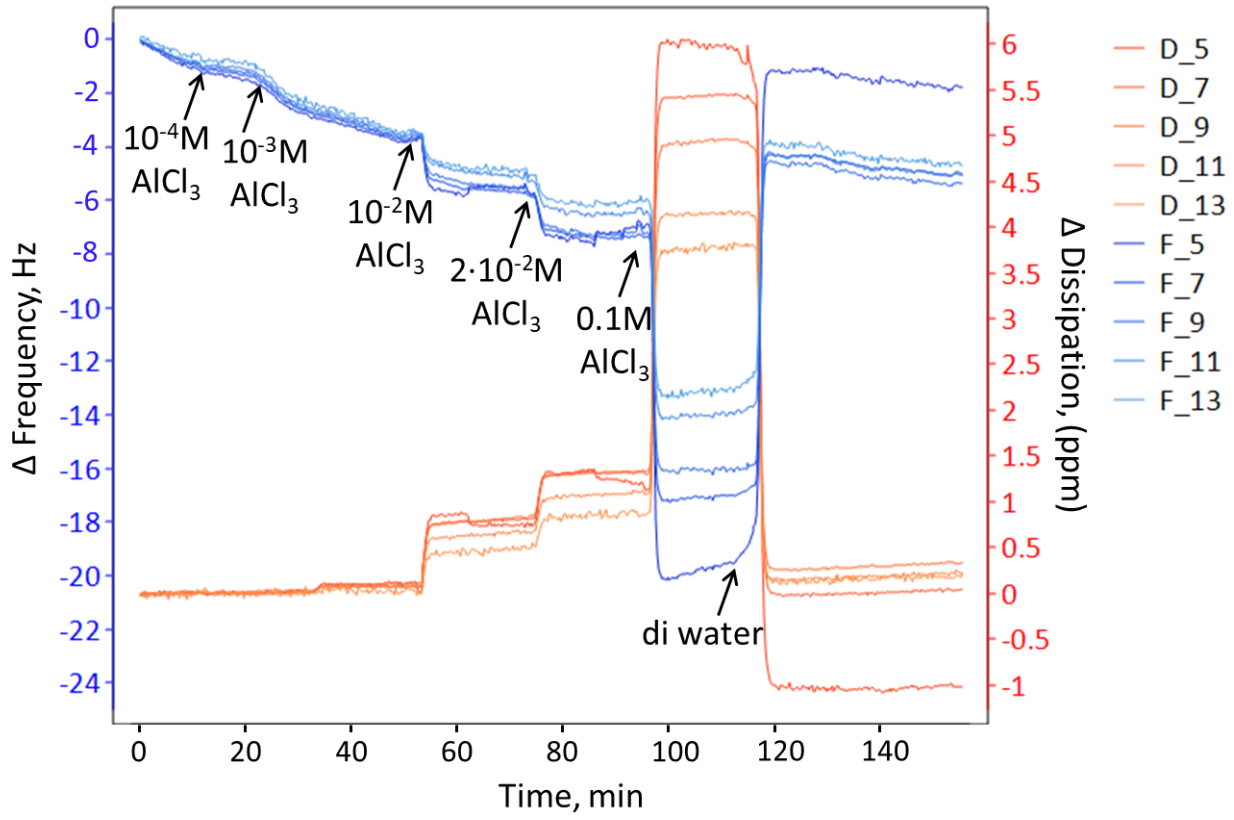

Figure 4.10. Response (changes in frequency and dissipation (5^{th} – 13^{th} overtones)) of a QCM-D sensor coated with a pGMA film without dopamine modification (ellipsometric thickness 222 nm) to various concentrations of $AlCl_3$ (pH of the solutions (pH 4.2 ± 0.2). The sensor was equilibrated in di water (pH 5.5) prior to the flow of the Al ion solutions.

Next, we alternated the flow of 10^{-2} M $AlCl_3$ and deionized water to estimate the reversibility and reproducibility of the response of dopamine-pGMA-coated sensors over multiple measurement cycles (Fig. 4.11). The shifts in the resonant frequency of ~60 Hz were observed upon exposure of the sensor to the ion solution for each cycle. Additionally, to estimate the effect of changes in solution pH on the response, we performed the same experiment using di water of pH 4 (adjusted by HCl). In this case, a similar response was observed but the shifts in frequency decreased to ~47 Hz (Fig. 4.12). As shown in the literature[145,156,238], coordination of metal ions by catechol ligands depends on the pH of the

environment. This phenomenon is attributed, in part, to the more facile deprotonation of hydroxyl groups with increasing alkalinity and interference from protons that compete with cations for binding to catechols in acidic conditions[239].

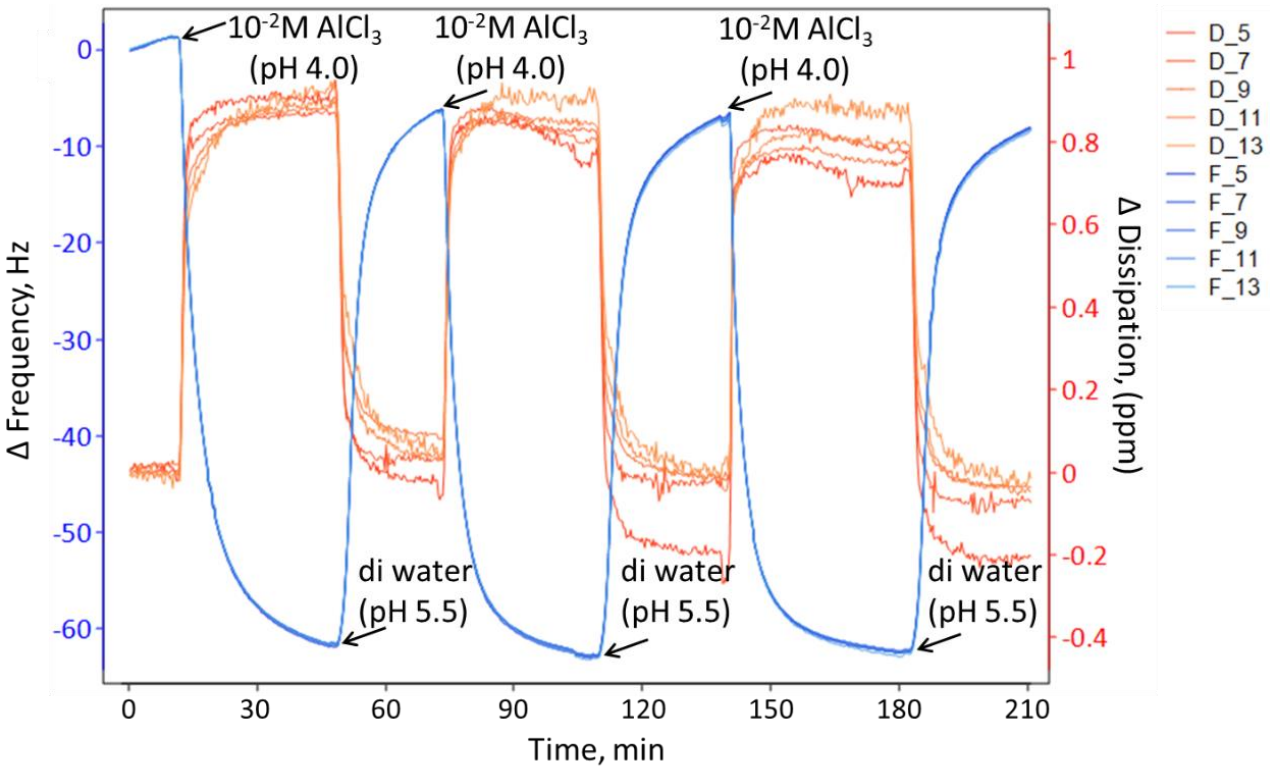

Figure 4.11. Response (changes in frequency and dissipation (5th – 13th overtones)) of a QCM-D sensor coated with a dopamine-pGMA film (ellipsometric thickness 297 nm) upon cycling between deionized water and a 10^{-2} M $AlCl_3$ solution.

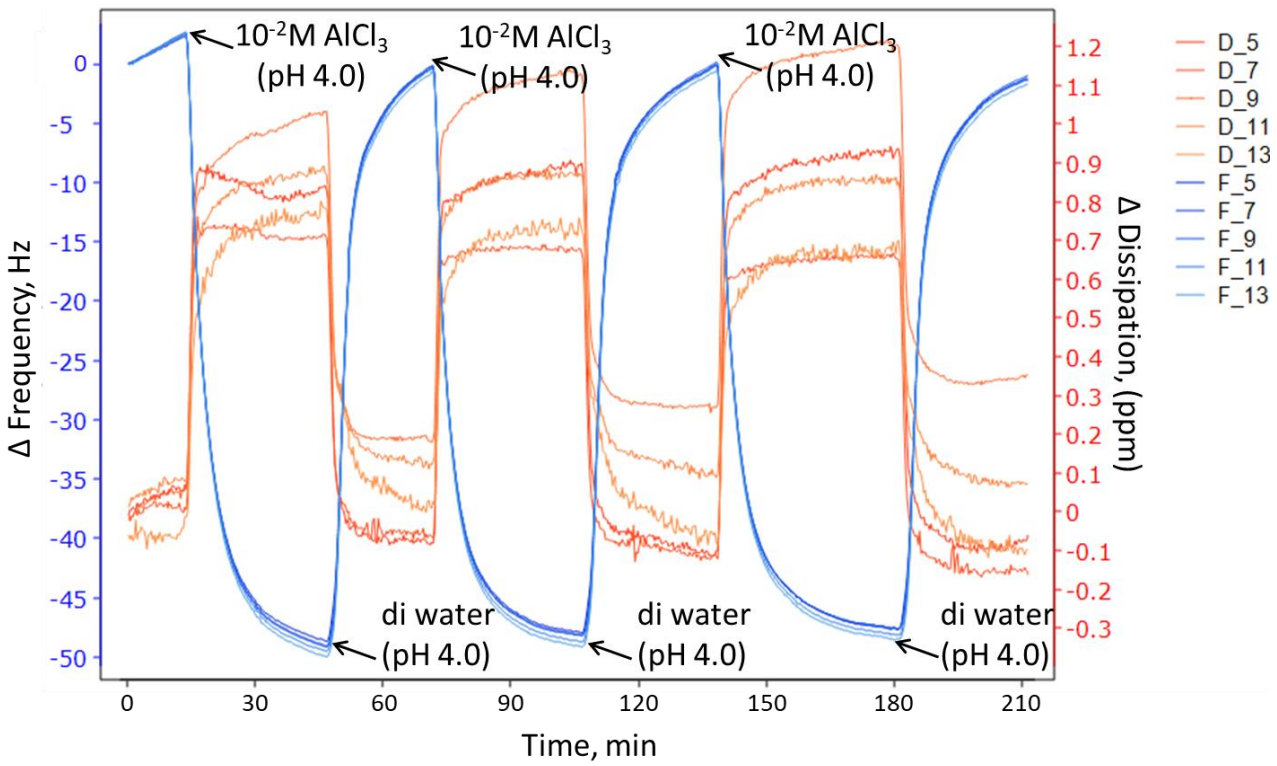

Figure 4.12. Response (changes in frequency and dissipation (5^{th} – 13^{th} overtones)) of a QCM-D crystal coated with a dopamine-pGMA film (ellipsometric thickness 297 nm) upon cycling between deionized water (pH 4.0, adjusted by adding HCl) and a 10^{-2} M $AlCl_3$ solution (pH 4.0).

To assess the selectivity of QCM sensors coated with dopamine-pGMA in the presence of an interfering lower affinity ion, we conducted experiments in which various concentrations of $AlCl_3$ were added to the solution containing a high concentration (10 mM) of $ZnCl_2$ (Fig. 4.13).

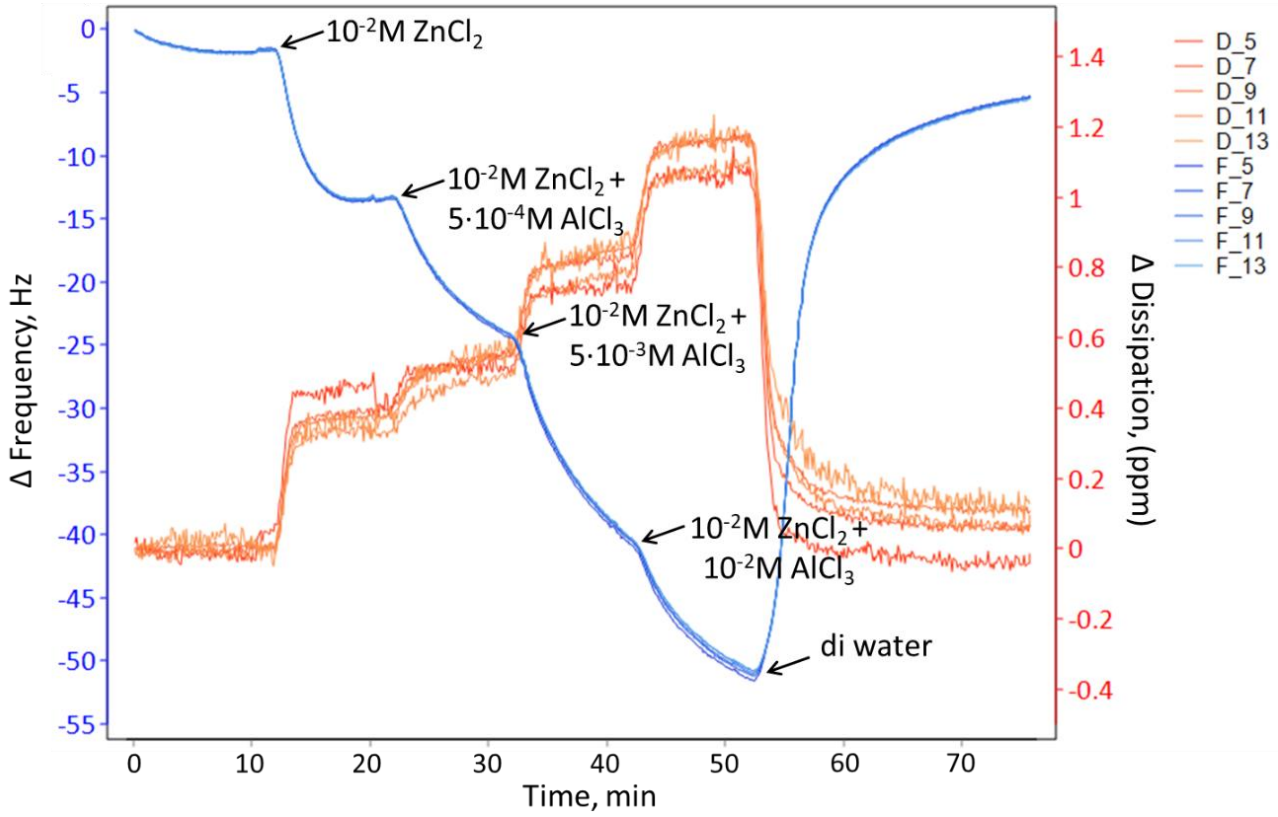

Figure 4.13. Response (changes in frequency and dissipation (5th – 13th overtones)) of a QCM-D sensor coated with a dopamine-pGMA film (ellipsometric thickness 298 nm) upon exposure to 10 mM aqueous solution of $ZnCl_2$ and the same solution with the addition of increasing concentrations of $AlCl_3$. The sensor was equilibrated in di water prior to introducing the ion solutions into the QCM-D cell.

The mass of the ions retained by the film can be derived from QCM-D data using the Sauerbrey equation[240] or by applying the Voight-Voinova model[186]. The Sauerbrey equation is valid for rigid films, but tends to underestimate the mass loading when shifts in dissipation are non-negligible[241,242]. Therefore, we determined the ion uptake by modeling: 1.6 ± 0.2 mmol/g (or 43 ± 4 mg) of Al^{3+} per g of film was retained from 10^{-2} M solutions (based on two independent measurements using dopamine-pGMA films with ellipsometric thickness of 297 and 294 nm). In contrast, a 298-nm-thick dopamine-pGMA film (Fig. 7) retained only ~0.4 mmol/g (~ 25 mg/g) of Zn^{2+} from a 10 mM solution of $ZnCl_2$.

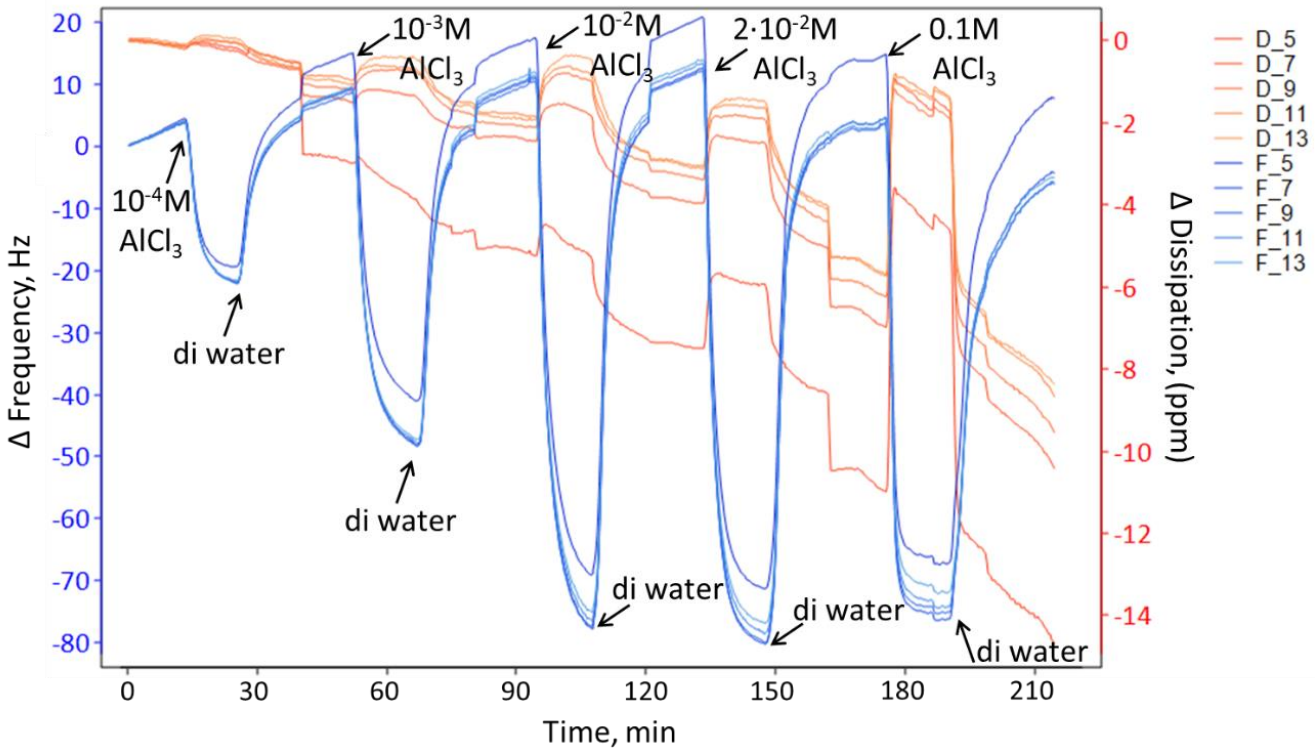

Figure 4.14. Response (changes in frequency and dissipation (5^{th} – 13^{th} overtones)) of a QCM-D sensor coated with a dopamine-pGMA film (ellipsometric thickness 294 nm) upon exposure to $AlCl_3$ solutions of various concentrations followed by di water washes. The data were for each concentration were recorded separately and stitched using QTools software.

Additionally, for equilibrium modeling of the ion uptake, we performed the measurements where the sensors were consecutively equilibrated in 10^{-4} – 0.1 M $AlCl_3$ solutions, followed by di-water rinses (Fig. 4.11). To fit the experimental data, we chose the Freundlich model[243,244] suitable for non-ideal and reversible sorption (eq. 2), which assumes an energetically heterogeneous surface with simultaneous sorption from multiple active sights well beyond a monolayer, when the stronger binding sites are occupied first and the enthalpies of sorption of the active sites decrease exponentially upon completion of the process[245]:

$$q_e = K_F C^{1/n} \tag{4.2}$$

where q_e (mol/g) is the concentration of ions retained within the film at equilibrium with a solution of a certain ion concentration C (mol/L), K_F in (mol/g)·(L/mol)$^{1/n}$ is a constant indicative of sorption capacity, n is a constant characterizing the energetic heterogeneity of the surface in the sorption process (1/n value ranges between 0 and 1; the more heterogeneous surface, the closer the value is to 0)[246].

As several papers reported issues with the linearization of eq. 4.2 that may result in violation of the theories behind the isotherm[245], we performed non-linear fitting. Figure 4.15 presents the data obtained empirically and modelled by the Freundlich sorption isotherm. The values of the Freundlich isotherm constants (K_F and n) determined as fitting parameters with 95 % confidence bounds are presented in Table 4.3.

Based on the ellipsometric thickness of the film used in the experiment (294 nm) and the film conversion estimated from ATR FTIR as 94%, assuming that each catechol group chelates one Al^{3+}, the maximum Al loading of 77.2 mg/g (or ~2.86 mmol/g) would be expected. This result is in a close agreement with the value of 77.6 mg/g (or ~2.88 mmol/g) for the Al^{3+} retained by equilibration with 0.1 M

$AlCl_3$ solution in the QCM-D experiment. The chelation data supports the high % modification of pGMA films obtained from FTIR spectra.

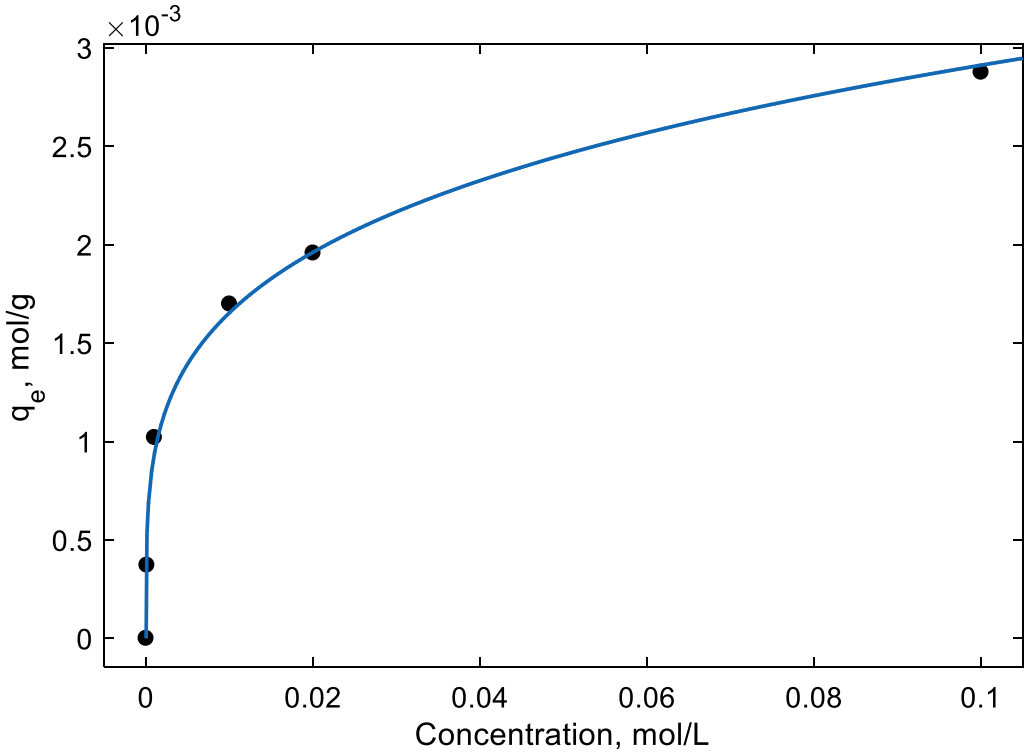

Figure 4.15. Sorption of Al^{3+} by a dopamine-pGMA film (ellipsometric thickness 294 nm, % modification via ATR-FTIR 94%). Points on the plot are experimental values (obtained from QCM-D) and the line represents the Freundlich model fitted to the data (R^2 = 0.9937, Sum of Squares Due to Error (SSE) = $3.606 \cdot 10^{-8}$).

Table 4.3. Values for the Freundlich model constants (for Al^{3+}).

The Freundlich Model Parameter	Value	95 % confidence interval
K_F, $(mmol/g)\cdot(L/mol)^{1/n}$	5.122	(4.274, 5.970)
n	4.076	(3.343, 4.809)

Conclusions

In this chapter, I have presented a new route for obtaining surface-tethered polymer films containing pendant catechol functional groups via ARGET ATRP of GMA and post-polymerization modification of pGMA with dopamine. The concentration of the catechol groups within the film can be adjusted based on the reaction conditions for post-polymerization modification.

I synthesized the dopamine-pGMA films on the surfaces of QCM-D sensors, which subsequently showed concentration-dependent response to Al^{3+} and Zn^{2+} ions. The ions could be desorbed from the films by rinsing them with pure di-water, resulting in regeneration of the sensors' surfaces. The response of the dopamine-pGMA coated QCM-D sensors to the same concentration of Al^{3+} ions was reproducible over multiple measurement/rinse cycles. Based on the QCM-D measurements, the dopamine-pGMA films were 4 times more selective to Al^{3+} over Zn^{2+} (i.e., sorbed 4 times more moles of Al^{3+} than Zn^{2+} from a 10 mM aqueous solution of the corresponding ion).

The Al^{3+} mass loading from a 0.1 M aqueous $AlCl_3$ solution obtained from QCM-D experiments is consistent with the theoretical calculations based on the assumption of monocatecholate complexes within the film, and supports the high % conversion of oxirane groups in pGMA with dopamine as determined based on ATR-FTIR spectroscopy.

Chapter V

FUNCTIONAL FREE-STANDING POLYMER FILMS AND COATINGS PREPARED BY SPIN COATING AND SURFACE-INITIATED ROMP

Introduction

Surface-initiated polymerization (SIP) techniques (also known as "grafting from") enable preparation of polymer films covalently attached to a substrate, while controlling the thickness, grafting density, and chemical functionality of the films with almost molecular level accuracy[65,101]. SIP involves in situ polymerization from an initiator immobilized onto a surface (usually via a self-assembled monolayer (SAM)). The main SIP approaches are based on well-known polymerization techniques, including ring-opening metathesis polymerization (ROMP)[120,126,247].

I have developed a fabrication method based on the combination of spin-coating and surface-initiated ROMP (Si-ROMP) techniques, which, depending on the surface functionalization prior to spin coating, can yield polymer films that are either robustly attached to the surface or free-standing. The advantages of the method over Si-ROMP alone are as follows: 1) the films can be made much thicker in a faster process; 2) the film may be removed from the substrate if desired; 3) for liquid monomers, no dissolution is required, which reduces use of organic solvents.

The advantages over spin coating alone include: 1) the coatings produced are chemically anchored to the substrate (if desired); 2) the polymer synthesis occurs during the deposition process, negating the need for bulk polymer synthesis and subsequent dissolution; 3) coatings with unique properties that are not obtainable by traditional spin coating can be prepared (e.g. solvent resistant coatings, precise polymer architectures); 4) post-polymerization modification of the coatings is significantly facilitated (separation of reaction byproducts is based on simple rinsing of the film).

In this chapter, I showcase the capabilities of the spin coating/Si-ROMP method to produce a range of functional polymer films with a focus on obtaining reactive scaffolds from poly(norbornene diacyl chloride) (pNBDAC). As our group has shown, the acid chloride pendant groups in pNBDAC films can be quantitatively modified to a virtually limitless number of functionalities[248] simply by dipping the substrates into a solution containing alcohols, amines, or thiols. This approach presents an advantage over traditional synthesis/modification of polymers in solution, as it eliminates the need for separation and purification of the desired product from the byproducts of the reaction.

The Jennings' research group has demonstrated synthesis of pNBDAC films via Si-ROMP[249], which were further modified to yield metal-chelating[249] and pH-responsive[23] polymer films. The initial goal for the development of the alternative process to Si-ROMP was to scale up the thickness of pNBDAC films: we had previously obtained ~500-nm-thick pNBDAC films (with the average roughness of 11 ± 6 nm) after 30-min-long Si-ROMP in 0.5 mol/L solution of NBDAC (unpublished data). In comparison, spin-coating/ROMP of NBDAC yields much thicker films (up to ~20 μm with roughness of < 50 nm), and the volume of the monomer required to obtain such films is more than 40% lower than that used in the Si-ROMP process for substrates of the same size.

In the previous work[249], we have shown that pNBDAC films modified to contain hydroxamic acid functional groups (HA-pNBDAC) can chelate a variety of divalent metal ions, including Fe^{2+}. This chapter highlights the capability of free-standing HA-pNBDAC films, the fabrication of which has been enabled by this new process, for chelation of Fe^{3+} in acidic (pH = ~2.5) environments, unveiling new possibilities for metal ion separation and detection.

Experimental section

Preparation of polymer films

Free-standing polymer films and coatings were prepared by the procedure depicted in Figure 5.1. A Si/SO_2 substrate (cleaned and optionally modified with the norbornene-terminated silane monolayer) was placed onto the vacuum chuck of the spin-coater, and 200 μL of 5 mM solution of Grubb's 3rd generation catalyst in DCM was dispersed by a micropipette into the center of the substrate, while rotating at 1000 rpm, and spun for 30 s. Then, to obtain a polymer coating of a desired thickness, a selected volume of a neat liquid monomer or monomer solution was dispensed into the center of the substrate rotating at a certain speed from 1300 – 6000 rpm, and spun for 60 s. The resulting polymer films were dried in vacuo at room temperature for at least 2 h prior to their characterization. The polymer films synthesized for this work are as follows: 1) pNBDAC from 100 or 200 μL of neat NBDAC monomer; 2) pNBOH films from 200 μL of neat NBOH monomer; 3) $pNBC_6F_{13}$ from of neat NBC_6F_{13} monomer; 4) pDCPD from 200 μL of 4 M solution of DCPD in DCM; 5) pDCPD-co-pNBDAC from 200 μL of solution containing 4 M DCPD and 3.5 M of NBDAC. Except for pNBDAC, all other films were synthesized with a spin speed of 3000 rpm.

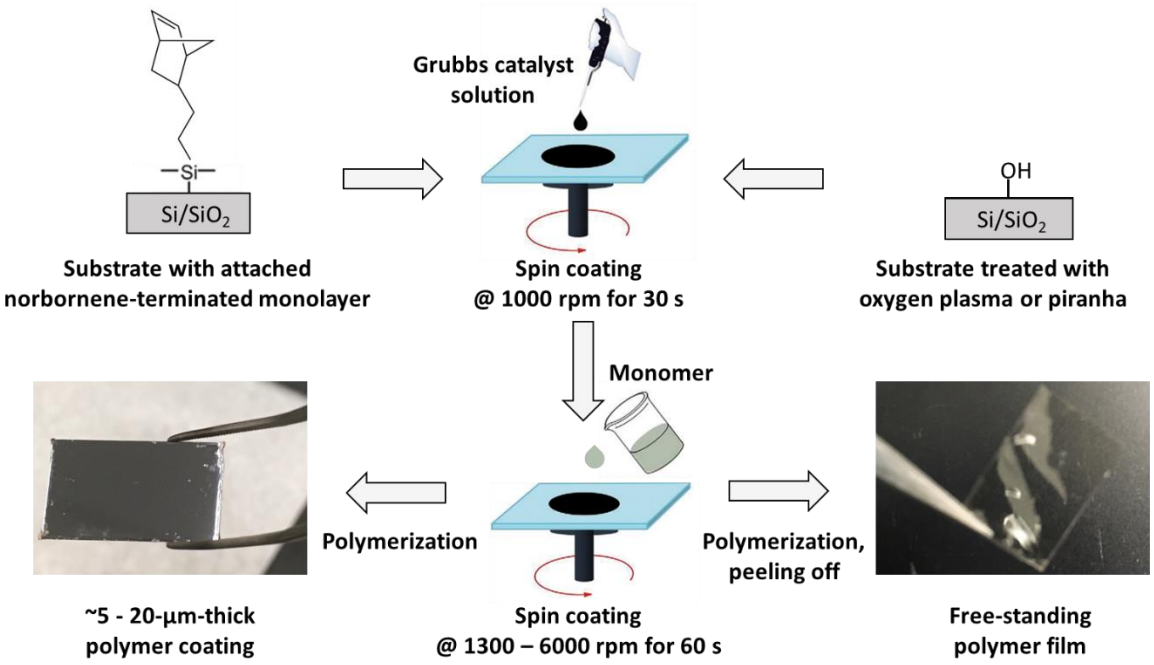

Figure 5.1. Schematics of the fabrication process for pNBDAC coatings and films. The same process was applied using other monomers.

Post-polymerization modification of pNBDAC films

pNBDAC films were immersed into a pure solvent (methanol, ethanol, or water) overnight to achieve full conversion of the acid chloride groups to ester or carboxylic acid. The full modification of pNBDAC films with amines (isopropylamine, diethylethylenediamine, and tetrahydropyrrole) was achieved after 3 h in 1M solution of the corresponding amine in DCM. The modification of pNBDAC with trifluoroethylamine hydrochloride was performed by immersion of the films into 1M solution of the compound in water containing a molar equivalent of triethylamine, and the full conversion of acid chloride groups was achieved in 1 h. To fully convert acid chlorides of pNBDAC to hydroxamic acid functional groups, the pNBDAC films were incubated for 20 h in 1M hydroxylamine hydrochloride in water. The

pH of the solution was adjusted to 6.2 by adding triethylamine. Regardless of the type of modification, all the films were extensively rinsed with the corresponding solvent, dried in the stream of N_2, and dried in vacuo at room temperature for at least 2 h prior to characterization.

Characterization

Sessile drop water contact angle measurements, ellipsometry of $NbSiCl_3$-modified substrates (Table 5.1), ATR–FTIR spectroscopy, and profilometry were performed according to the procedures described in Chapter III.

Table 5.1. Properties of the $NBSiCl_3$ monolayers deposited onto Si/SiO_2 (the average values for thickness and water contact angles with standard deviations from more than 5 independently prepared samples).

Ellipsometric thickness, nm	Water contact angle, °	
	Advancing (θ_A)	Receding (θ_R)
0.8 ± 0.2	90 ± 4	75 ± 3

Ultraviolet–visible spectroscopy (UV-vis) using a Varian Cary 5000 UV-vis-NIR spectrophotometer was performed to record the changes in the light absorption properties of free-standing HA-pNBDAC films upon chelation of metal ions. The films were immersed into 10 mM aqueous solutions of $FeCl_3$ and $ZnCl_2$ or di-water (for reference) for 2 h, rinsed with di water, dried in vacuum at room temperature for 30 min, and analyzed via UV-vis absorption for the wavelengths of 300 – 800 nm. Next, the films were incubated in 0.1M EDTA aqueous solution for 2 h to remove the ions, rinsed with di water, and dried in vacuum at room temperature for 30 min prior to acquiring the UV-vis absorption spectra.

An Instrument Specialists TGA 1000 was used to characterize the thermal stability of free-standing HA-pNBDAC films. For each measurement, a sample was placed into a platinum heating pan, and the

mass of the sample was recorded prior to heating. Next, the temperature was increased from 25 °C to 900 °C at a constant rate of 10 °C/min and the % change in the sample mass was recorded. The measurements were conducted under the flow of nitrogen or air of 100 mL/min. In addition to the obtained mass change vs. temperature curves, the derivatives of the mass change $\frac{dm}{dt}$ vs. temperature were also calculated, which allows the point where weight loss is the most apparent, as well as any overlapping thermal decomposition steps, to be identified more clearly.

Results and Discussion

The developed polymer film fabrication process consists of the following steps (Figure 5.1): 1) substrate preparation (cleaning and deposition of a monolayer, if an attached film is desired); 2) spin coating of the ROMP catalyst solution; 3) spin coating of a cyclic olefin monomer. The polymerization of the monomer/catalyst combinations tested to date proceeded "in situ," and a smooth solid film was obtained after 60 s of spinning. Although the films did not require drying, they were placed into a vacuum chamber and kept at room temperature for 2 h before characterization to remove any lingering volatile components before further handling outside of a fume hood.

The thickness and other properties of the polymer films (e.g., polydispersity, molecular weight of the polymer chains) can be controlled by varying the process parameters, such as the relative amounts of catalyst and monomer dispensed onto the substrate, speed and duration of spinning, choice of the catalyst, solvents, and surface modification of the substrate. In this paper, for the synthesis of pNBDAC films, we have varied the monomer volume and spin speed, while the type and amount of catalyst and the time of spinning were kept constant for all the experiments. To ascertain that our process is applicable to a range of functional monomers, we synthesized films from two other liquid norbornene monomers (NBOH and

NBC_6F_{13}) and from a concentrated (4 M) solution of DCPD, which is a solid at room temperature. Additionally, as a proof of concept, we prepared a copolymer film from a solution containing 4 M DCPD and 3.5 M of NBDAC. The photos of the samples and the schematics of the chemical structures of their repeat units are given in Figure 5.2, and the values of the average film thickness and roughness are given in Tables 5.2 and 5.3. The chemical composition of the films was confirmed by ATR-FTIR (Fig. 5.3).

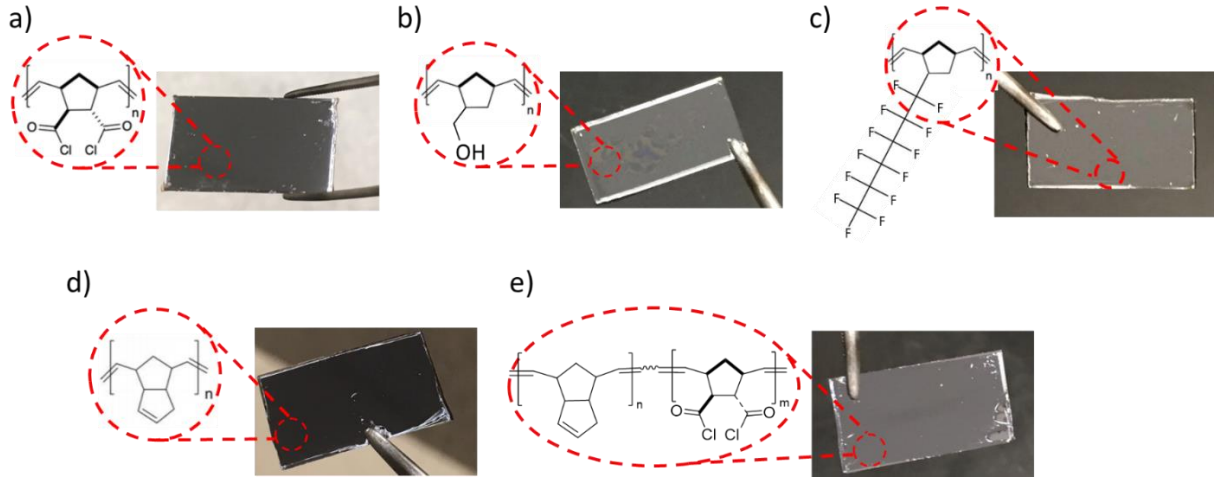

Figure 5.2. Photographs and schematic chemical structures of a) ~20µm-thick pNBDAC, b) ~8-µm-thick pNBOH, c) ~9-µm-thick $pNBC_6F_{13}$, d) ~ 6-µm-thick pDCPD, and e) ~14-µm-thick random copolymer pDCPD-co-pNBDAC films on Si/SiO2. All the films were obtained using 200 µL of the corresponding neat monomer or monomer solution in DCM and spin speed of 3000 rpm.

Table 5.2. The average thickness and roughness (R_a) (with standard deviations) of polymer films obtained by spin coating/ROMP*.

Type of polymer	Number of samples	Thickness, µm	R_a, nm
pNBOH	3	8.9 ± 1.2	20 ± 9
$pNBC_6F_{13}$	3	5.7 ± 3.1	15 ± 9
pDCPD	2	6.0 ± 1.5	45 ± 13
pDCPD-co-pNBDAC	1	14.3	140

* prepared from 200 µL of neat monomer of monomer solution, 3000 rpm spin speed

Table 5.3. The average thickness and roughness (with standard deviations) of pNBDAC films prepared by spin coating/ROMP (dispensed monomer volume (V_{NBDAC}) 100 or 200 µL).

Spin speed, rpm	V_{NBDAC} = 100 µL		V_{NBDAC} = 200 µL	
	Thickness, µm	R_a, nm	Thickness, µm	R_a, nm
1300	17.4 ± 2.8	19 ± 17	18.3 ± 1.4	28 ± 14
2000	13.1 ± 2.4	28 ± 17	16.3 ± 1.9	13 ± 6
3000	9.9 ± 2.2	14 ± 7	12.6 ± 0.8	17 ± 15
4000	9.3 ± 1.9	22 ± 20	12.4 ± 2.2	27 ± 11
5000	4.4 ± 1.5	10 ± 4	10.9 ± 1.9	55 ± 42
6000	3.3 ± 0.7	10 ± 11	8.9 ± 1.1	53 ± 28

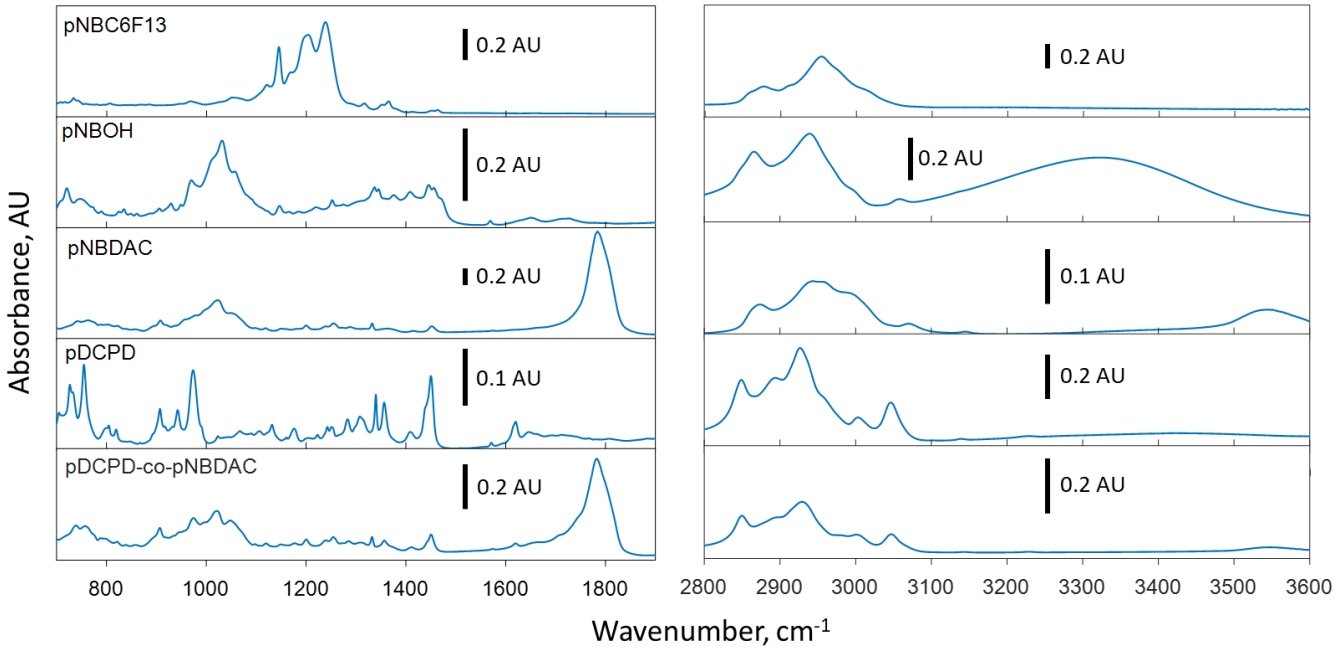

Figure 5.3. ATR-FTIR spectra of pNBDAC, pDCPD, pDCPD-co-pNBDAC, pNBOH, and $pNBC_6F_{13}$.

Next, I will briefly discuss results for each type of polymer film mentioned above, and then address preparation, post-polymerization modification, and potential applications of pNBDAC films in more detail.

pNBC$_6$F$_{13}$

Fluorinated polymers represent a unique class of materials that combine multiple valuable properties, such as outstanding chemical and thermal stability along with low critical surface energy, water absorptivity, and dielectric constant[43,50]. Fluoropolymers are utilized in many fields of industry as barrier[106], dielectric, antifogging and antifriction coatings[250], membranes[251], and biomaterials[252].

Our group has previously[43] synthesized an assortment of poly 5-(perfluoro-n-alkyl) norbornene films, including pNBC$_6$F$_{13}$, on gold-coated Si substrates via Si-ROMP. The thickness of the films ranged from tens of nm to ~1.5 μm, depending on the monomer concentration in the polymerization solution. The method described in this paper can yield much thicker films (~5.7 ± 3.1 μm with the roughness of 15 ± 9 nm) (Table S4), and is adaptable to a variety of substrates. Moreover, pNBC$_6$F$_{13}$ is insoluble in organic solvents or water. Thus, direct spin coating of the pNBC$_6$F$_{13}$ would present a challenge, as high solubility of the polymer in the solvent used for spin coating is a must for obtaining quality films[51,60].

As expected for perfluorinated compounds[232], the IR spectra of pNBC$_6$F$_{13}$ films (Fig. 5.3) exhibited a series of absorbance peaks associated with the C$_6$F$_{13}$ pendant group: CF stretching and deformation of CF$_3$–CF$_2$– at 1367 cm^{-1} and 734 cm^{-1}, respectively; CF$_2$– asymmetric stretching[253] at 1235 and 1204 cm^{-1}; CF$_2$– asymmetric stretching[253] at 1145 cm^{-1}; CF stretching of –CF$_3$ at 1168 and 1052 cm^{-1}. Additionally, we observed a number of bands characteristic for ROMP-type norbornene polymers[44]: the peak at 968 cm^{-1}corresponds to trans C=CH out of plane bending of the olefin functionality along the backbone[254], the doublet at 1451/1463 cm^{-1} is due to CH$_2$ scissoring deformation, the peaks at 2955 and 2879 cm^{-1} are due to stretching of cyclic CH$_2$, stretching of acyclic CH$_2$ corresponds to the peak at 2862 cm^{-1}, and a shoulder at 2913 cm^{-1} is due to CH stretching.

We utilized contact angle goniometry to evaluate the wetting properties of $pNBC_6F_{13}$ films (Table 5.4). As evidenced by the dynamic contact angle values for water and hexadecane, $pNBC_6F_{13}$ films are omniphobic, i.e., repel both water and oil, due to perfluorohexyl groups that dominate the surface of the film. This is most evident when comparing the values for hexadecane contact angle of $pNBC_6F_{13}$ with that of polynorbornene (θ_A < 15°, θ_R <15°)[44] and poly(hexyl-norbornene) ($pNBC_6H_{13}$) (θ_A= 23 ± 5, θ_R <15°)[44].

Table 5.4. Wetting properties of polymer films (average and standard deviation values for three independently prepared samples).

Polymer	**Contact Angle Water, °**		**Contact Angle Hexadecane, °**	
	Advancing, θ_A	Receding, θ_R	Advancing, θ_A	Receding, θ_R
$pNBC_6F_{13}$	115 ± 3	85 ± 3	63 ± 3	38 ± 3
pNBOH	73 ± 2	30 ± 3	< 10	< 5
pDCPD[a]	86 ± 3	45 ± 3	12 ± 3	< 5
pDCPD-co-pNBDAC[b]	86 ± 1	< 10	14 ± 2	< 5

[a] 2 samples; [b] 1 sample

<u>pNBOH</u>

pNBOH films are of interest because they possess hydroxyl functional groups that can be modified via multiple routes following the film preparation, and unlike pNBDAC, pNBOH films are stable at ambient conditions for prolonged periods of time. Notably, to obtain uniform substrate coverage with pNBOH films, the monomer had to be dispensed statically (to cover most of the wafer) followed immediately by spinning. The values for the film thickness of 8.9 ± 1.2 μm and roughness of 20 ± 9 nm were observed based on 3 independently prepared films.

The ATR-FTIR spectra of pNBOH (Fig.5.3) show a strong absorbance band at 3000 – 3500 cm^{-1} due to the hydroxyl functionality, and the broadness of the peak indicates the presence of intermolecular hydrogen bonding[232]. The peaks at 2864 and 2938 cm^{-1} are attributed to cyclic and acyclic CH_2 stretching of the backbone, respectively. The two small shoulders at 2846 and 2997 cm^{-1} are due to symmetric and asymmetric CH_2 stretching, respectively, of the pendant group. In the fingerprint region of the IR spectrum, the prominent peaks are located at: 968 cm^{-1} (CH_2 twisting), 1010 and 1058 cm^{-1} (C–O stretching), and 1031 cm^{-1} (C–C–O stretching) of the pendant ($R_1R_2CHCH_2OH$) group[232].

pDCPD

pDCPD is one of the most commercially important polymers prepared by ROMP to date. It is synthesized from a low-cost readily available DCPD monomer – a byproduct from the production of ethylene[255]. ROMP of DCPD results in a cross-linked polymer characterized by high temperature and chemical resistance and excellent mechanical properties (e.g., high impact strengths)[255,256].

Our group demonstrated synthesis of pDCPD polymer films via Si-ROMP from vaporized neat monomer with thicknesses of up to ~400 nm[257] (and roughness ranging from ~10 – 50 nm) achieved after 1 min of polymerization. The films possessed high stiffness and good barrier properties[257]. In this work, we prepared pDCPD films with thickness of ~6.0 ± 1.5 μm (roughness of 45 ± 13 nm) by spin coating/ROMP of a 4 M DCPD solution in DCM as solvent (Fig. 5.2).

In agreement with the previous report[257], the ATR-FTIR spectrum of pDCPD (Fig. 5.3) shows the characteristic peaks at 1620 cm^{-1} due to C=C stretching, 1450 cm^{-1} due to a C_{sp3}–H scissoring ($\delta_s CH_2$), 1409 cm^{-1} due to a C_{sp2}–H scissoring (δ_s=CH_2); multiple C_{sp3}–H wagging and twisting ($\omega,\tau CH_2$) in the region 1356 −1150 cm^{-1}, multiple C_{sp2}–H out-of-plane bending vibration absorption bands between 1000 – 650 cm^{-1} and a band at 727 cm^{-1} due to C_{sp3}–H rocking ($\delta_s CH_2$). The peaks in the hydrocarbon

stretching region of the FTIR spectrum correspond to the C_{sp2}–H stretching at 3003 and 3046cm^{-1}, the C_{sp3}–H asymmetric stretching ($\nu_{as}CH_2$) at 2849, 2894, and 2926 cm^{-1}.

pDCPD-co-pNBDAC

Copolymerization of DCPD with other functional monomers allows tailoring of mechanical, thermal, and rheological properties of the resulting material[255]. Here, we demonstrate synthesis of a random copolymer from solution of DCPD and NBDAC monomers in DCM. This monomer configuration is particularly interesting for enabling the adjustment of the amount of modifiable acid chloride groups within the films.

The ATR-FTIR spectrum of the film (Fig. 1) indicates successful copolymerization, as evidenced by the presence of peaks characteristic for both pDCPD and pNBDAC. Interestingly, the roughness of this 14.3-µm-thick pDCPD-co-pNBDAC film was much higher (140 nm) than that of the homopolymer films of either pDCPD or pNBDAC of comparable thickness (Tables 5.2 and 5.3), but still roughness was less than 1 % of the film thickness.

pNBDAC

pNBDAC is a highly reactive polymer, and is unstable in ambient conditions for prolonged periods of time due to hydrolysis of the acyl chlorides by water vapor. The process of preparing pNBDAC by conventional spin coating would require synthesis of the polymer and its purification under inert atmosphere (to prevent loss of the acid chloride functionality). To prepare functional polymer films using pNBDAC as a scaffold, pNBDAC would have to first be modified with desired functional groups in bulk solution, purified, and then spin coated using a suitable solvent. The method described in this paper allows preparing pNBDAC films as an intermediate product, which can be stored in vacuum or under inert atmosphere until further modification is desired. When pNBDAC films are robustly attached to the

substrate, the modification procedure is substantially simplified and accelerated. This base pNBDAC film can then be used to prepare a countless number of polymer film compositions based on simple modification of the acyl chlorides in amines, alcohols, thiols, or water.

The main feature of ATR-FTIR spectra of pNBDAC films (Fig. 5.3) in the fingerprint region is the absorption band at 1784 cm^{-1} due to C=O stretching of acid chloride. The bands in the hydrocarbon stretching region of the spectrum include: the C_{sp3}–H asymmetric stretching at 2872 cm^{-1}, the C_{sp3}–H asymmetric stretching at 2949 and 2996 cm^{-1}, and the C_{sp2}–H stretching at 3070 cm^{-1}.

To estimate the impact of the spin speed and volume of the monomer on the properties of the resulting pNBDAC films, we spin coated either 100 or 200 µL of NBDAC at spin speeds ranging from 1300 to 6000 rpm (Fig. 5.4). As seen in Figure 2, illustrating the film thickness vs spin speed, the error bars for the samples obtained from 100 and 200 µL of the monomer at spin speeds of 1300 – 4000 rpm largely overlap. The 3rd generation Grubbs' catalyst we used in this process is known for its remarkably fast initiation rate (k_{init} (at 5 °C) > 4 s^{-1}). Likely, at low spin speeds, the monomer is polymerized into a stable film before its shear thinning and spin off of larger volume of the monomer can occur. The values for the film thicknesses for the two types of samples differ substantially at higher rpm: the films obtained from 100 µL of NBDAC are, on average, ~2.5 and 3 times thinner (for 5000 and 6000 rpm, respectively) than those obtained from 200 µL (Table 5.3), suggesting that the rate of spin off is more balanced with the polymerization reaction rate than that at slower spin speeds.

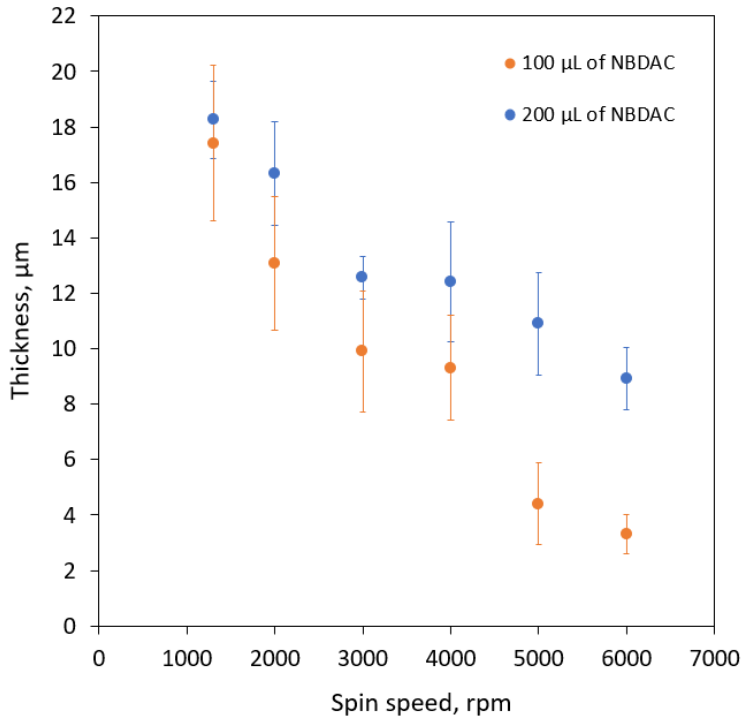

Figure 5.4. Thickness (measured by profilometry) of pNBDAC films on Si/SiO_2 obtained by spin coating either 100 or 200 µL of NBDAC monomer at various spinning rates. The data points and error bars represent the average and standard deviation values measured from at least three independently prepared samples (see Table 5.3 for the values).

Post-polymerization modification of pNBDAC

To illustrate the capabilities of the post-polymerization modification process for pNBDAC films with thicknesses of up to 20 µm, we performed a number of modifications by immersing the substrates coated with pNBDAC into the corresponding solutions.

Figure 5.5 presents the ATR-IR spectra of ~20 µm-thick pNBDAC films modified in alcohol or di-water to obtain carboxylic acid and ester functionalities, respectively. The full conversion of the acid chloride groups was achieved after an overnight (~ 16 h-long) reaction, as evidenced by the loss of the

peak corresponding to the carbonyl stretching in acid chloride at ~1784 cm^{-1} and emergence of C=O stretching peaks corresponding to the ester (1724 and 1726 cm^{-1}) and carboxylic acid (1693 cm^{-1}). The broad band seen at 3200 – 3600 cm^{-1} in the samples modified to contain carboxylic acid groups is due to the hydrogen bonding of OH groups, the bands at ~1409 and 1290 cm^{-1} correspond to CO stretching coupled with OH in-plane bending[258], and absorbance at 2700 − 2500 cm^{-1} is caused by the overtones and combinations of bands near ~1409 and 1290 cm^{-1} enhanced by Fermi resonance with the broad OH stretching peak[258].

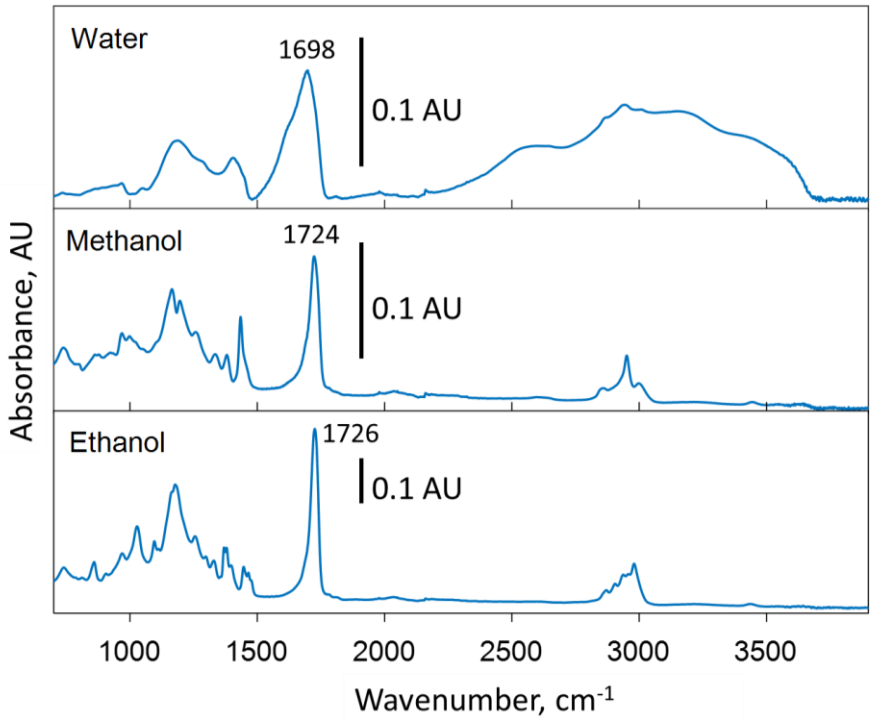

Figure 5.5. ATR-FTIR spectra of pNBDAC films modified to contain carboxylic acid or ester pendant groups by immersion into water, methanol, and ethanol overnight.

Next, we demonstrated quantitative modification of pNBDAC films with various free amines (Fig. 4) to obtain potentially temperature-responsive films. Recently, Zhao et. al[20] have synthesized

polymers with the same chemical structures by ROMP in solution by another route: template polymers with two pentafluorophenyl ester side groups were prepared and subsequently modified with various amines. The polymers demonstrated thermal response with lower critical solution temperature (LCST) (i.e., switching of their solubility in water from soluble to insoluble) depending on the type of the pendant group. For example, polymers modified with isopropylamine were insoluble in water in the tested temperature range (0 – 99 °C), polymers with diethylaminoethylamine had a cloud point of T_{cp} = 24.4 °C, and those modified with tetrahydropyrrole showed T_{cp} = 31.1 °C.

In this work, the full conversion of acid chloride groups in pNBDAC films to amides was achieved after 3 h in 1 M amine solution in DCM (other amine concentrations and shorter exposure times have not yet been tested). The peaks at 1630, 1641, and 1647 cm^{-1} correspond to amide I and those at 1547 and 1550 cm^{-1} to amide II stretching vibrations.

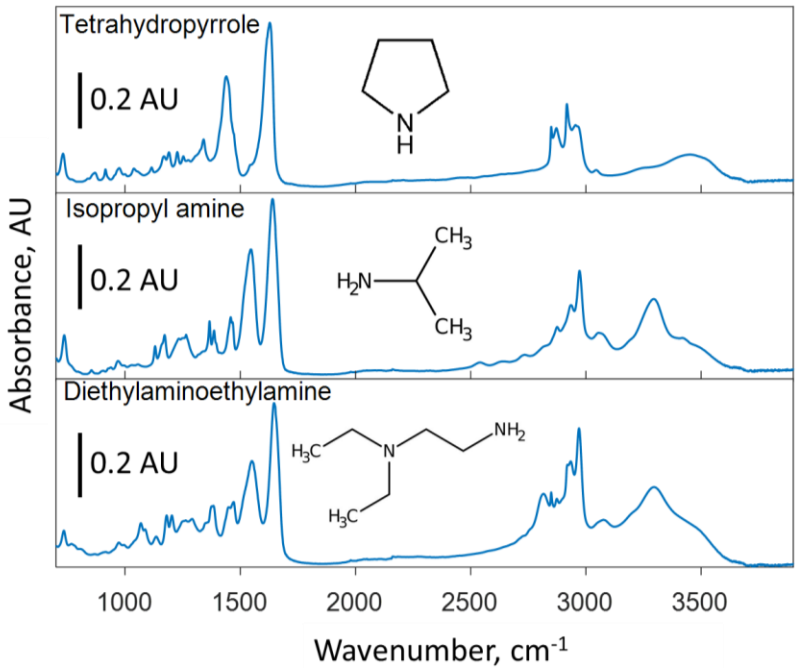

Figure 5.6. ATR-FTIR spectra of pNBDAC films modified with 1M solution of tetrahydropyrrole, isopropyl amine, and diethylaminoethylamine in DCM.

To realize hydrophobic/oleophobic functionality, pNBDAC films were modified to contain trifluorocarbon groups. The coated substrates were immersed into 1M aqueous solution of trifluoroethylamine hydrochloride salt containing a molar equivalent of triethylamine (to deprotonate the amine), and the full conversion of acid chloride groups was achieved in 1 h. Even though we used water as a solvent, no carboxylic acid side product was observed in the FTIR spectra (Fig. 5.7) of the films, as the amine reacts with acid chloride >10^7 times faster than water does[259].

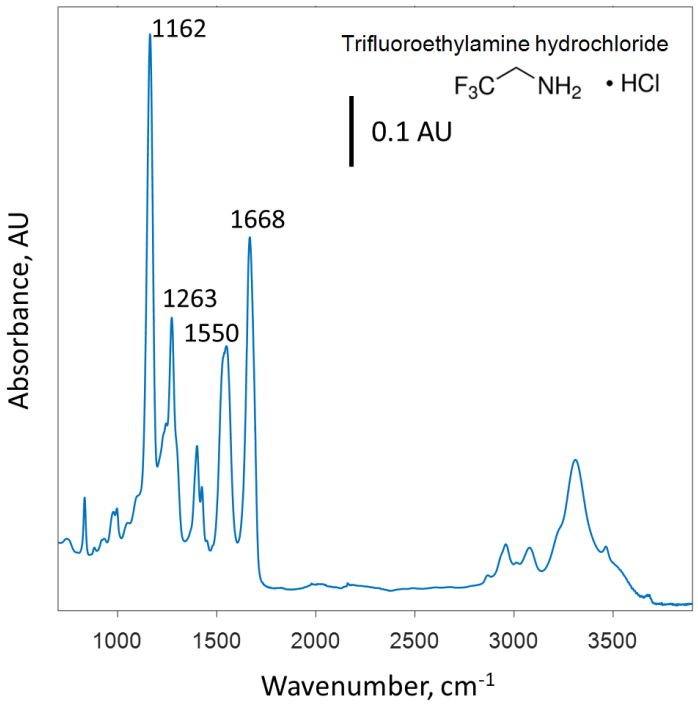

Figure 5.7. ATR-FTIR spectra of pNBDAC films modified with 1M solution of trifluoroethylamine hydrochloride in water. The peaks correspond to the following bands: 1668 cm^{-1} and 1550 cm^{-1} are due to amide I and amide II, respectively; 1263 and 1162 cm^{-1} correspond to CF_3 stretching.

The wetting properties of the F_3CNH-pNBDAC films are presented in Table 5.5.

Table 5.5. Wetting properties of F_3CNH-pNBDAC (average values and standard deviations based on three independently prepared samples).

Contact Angle Water, °		**Contact Angle Hexadecane, °**	
Advancing, θ_A	Receding, θ_R	Advancing, θ_A	Receding, θ_R
75 ± 1	43 ± 2	39 ± 1	33 ± 2

To obtain metal-complexing[249] hydroxamic acid functionality, pNBDAC-coated substrates were immersed into a 1M solution of hydroxylamine hydrochloride in water (pH adjusted to 6.2[259] by adding triethylamine). Although the complete conversion of acid chlorides in ~20 μm-thick films was evident from their FTIR spectra after 1 h of reaction, initially about 1/3 of the acid chlorides were modified to O-acylhydroxylamine (an ester side product), which could only be fully converted to hydroxamic acid groups after a 20-h reaction (a small peak at 1740 cm^{-1} can still be seen after 3 h) (Fig. 6).

In 1958, Jencks[259] reported that reaction of hydroxylamine with acid halides or anhydrides proceeds in two stages:

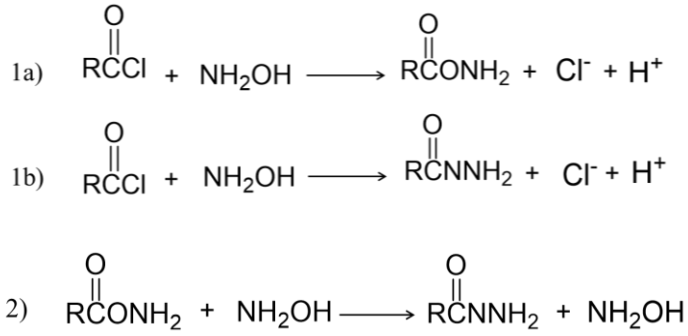

first, in addition to hydroxamic acid ("N-acylhydroxylamine") (1b) an unstable O-acylhydroxylamine is largely formed (1a) (up to 92%, increasing with the increasing electron-donating character of the leaving group[260]). O-acylhydroxylamine, in turn, reacts more slowly with hydroxylamine to from hydroxamic

acid (2). The author identified that the second reaction achieves its optimum kinetics at pH 6.2, which was corroborated by our experiments.

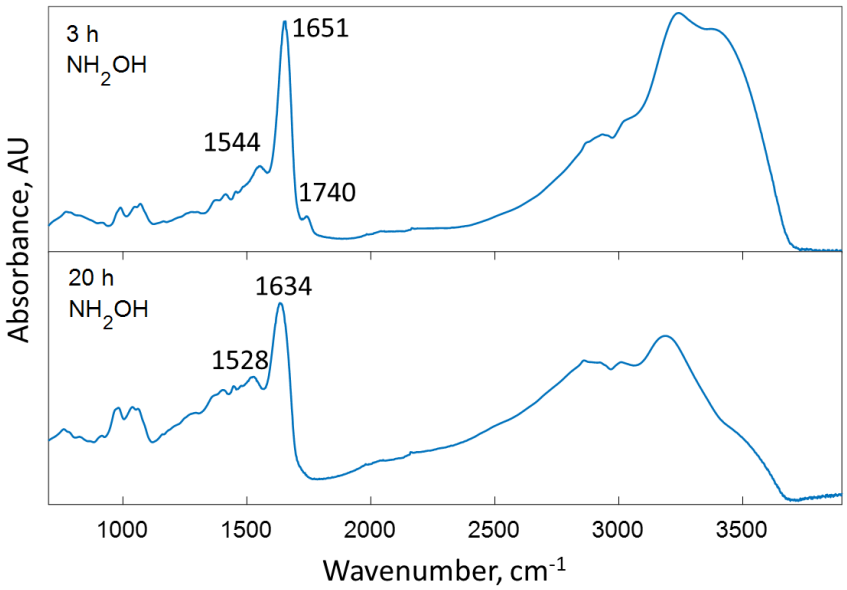

Figure 5.8. ATR-FTIR spectra of a pNBDAC film after 3 h (top) and 20 h (bottom) of immersion into 1M solution of hydroxylamine hydrochloride in water.

Reversible metal chelation with free-standing HA-pNBDAC films

Free-standing HA-pNBDAC films, which are inherently transparent, demonstrated visible color change (red hue) upon chelation with metal ions (Fig. 5.9a). Figure 5.10 presents the UV-vis spectra of HA-pNBDAC films after chelation in 10 mM unbuffered aqueous solutions of $FeCl_3$ and $ZnCl_2$, compared to the sample that was incubated in pure di water. The films incubated in the ion solutions demonstrate absorption peaks at ~450 nm, which is consistent with the values found in the literature[261]. The ions could be completely removed from the films by immersion into a 0.1 M EDTA solution for 2 h (Fig.5.9b), as evidenced by the UV-vis spectra measured afterwards (Fig. 5.11).

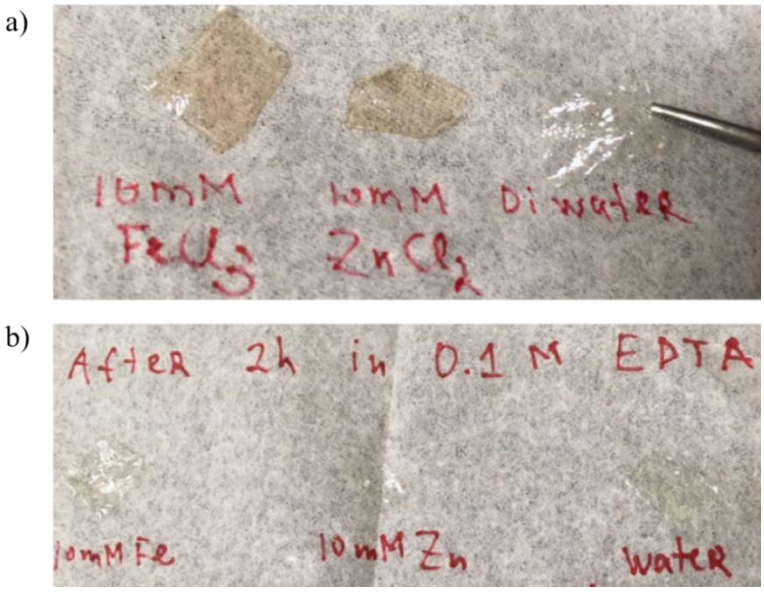

Figure 5.9. Photographs of: a) HA-pNBDAC films after immersion into the corresponding ion solutions or deionized (DI) water (for reference); b) the same HA-pNBDAC films after immersion into 0.1M EDTA solution for 2 h: as the ions were removed from the films, the films became transparent; a reference sample (only exposed to di water) is included for comparison.

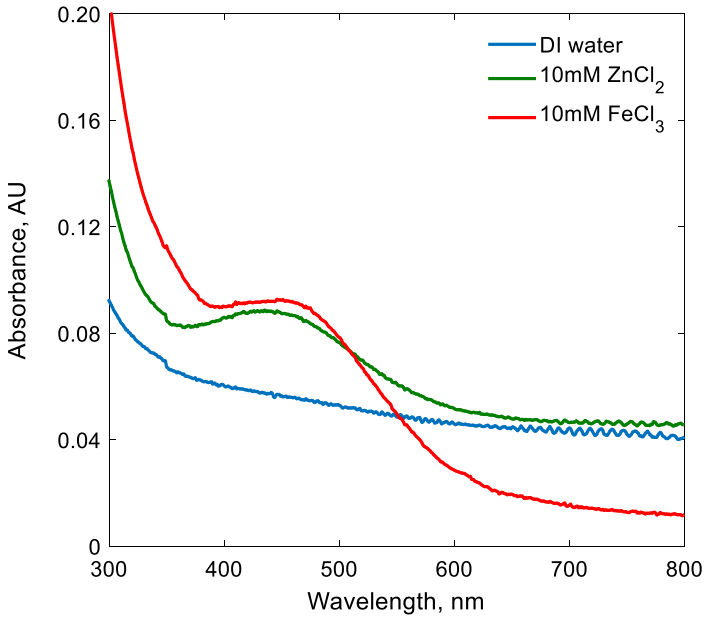

Figure 5.10. UV-vis absorbance of the HA-pNBDAC films after immersion into the ion solutions vs the control sample (incubated in DI water).

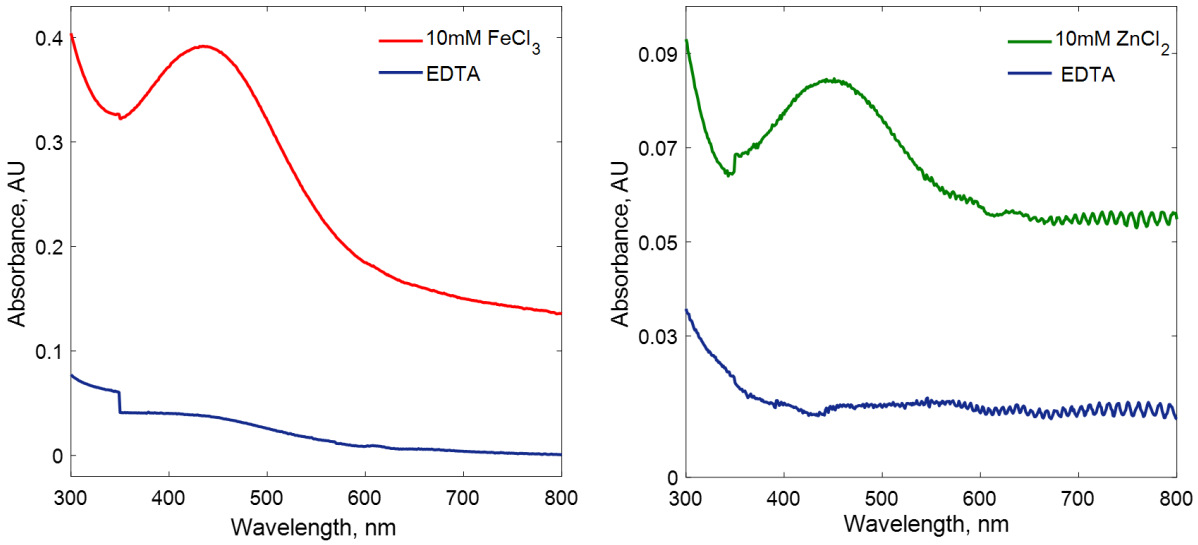

Figure 5.11. UV-vis spectra of the HA-pNBDAC films after immersion into the ion solutions and EDTA, showing the disappearance of the peaks upon removal of the ions from the films.

To characterize the thermal stability of as-synthesized and chelated HA-pNBDAC films, we conducted TGA analysis in air (Fig. 12). At the onset of the measurement, a weight loss of ~10% is observed due to the release of moisture bound within the films. The thermograms indicate that the polymer undergoes degradation in two stages. The first, between ~170 and 280 °C (corresponding to the weight loss of ~22 %), was the degradation of the pendant hydroxamic acid groups. This is supported by the ATR-FTIR spectrum obtained for a sample that had been previously heated to 270 °C within the TGA instrument's furnace (Fig. 13), which shows loss of the amide peak (initially located at ~1640 cm^{-1}). Similar temperatures of decomposition have been reported for HA functional groups in other polymers[262–264]. The polymer backbone decomposed between ~450 and 550 °C, proceeding to full pyrolysis by ~ 590 °C (practically no residue was left behind).

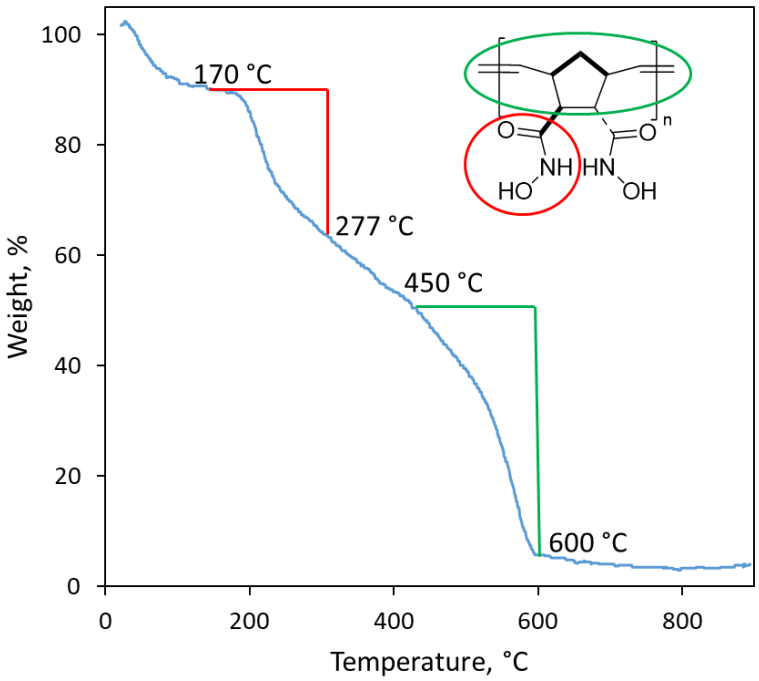

Figure 5.12. Thermogram of a free-standing HA-pNBDAC film depicting the % loss of the total mass of the sample as a function of temperature (measured in air).

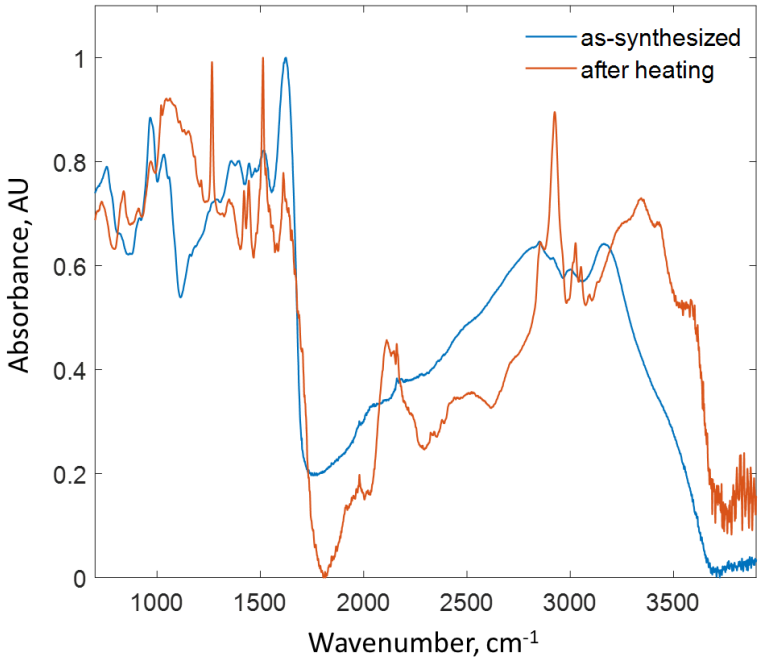

Figure 5.13. Normalized ATR-FTIR spectra for a free-standing HA-pNBDAC film acquired before and after heating to 270 °C.

Next, we chelated a HA-pNBDAC film in 10 mM $FeCl_3$ solution for 2h, then separated a portion of the chelated film and immersed it into 0.1 M EDTA solution to remove the ions. Subsequently, we used both samples for TGA analysis (Fig. 5.14). The thermal decomposition curve of the sample containing metal ions showed a similar two-stage process to the one described above, but did not culminate in full pyrolysis: the inorganic residue (likely Fe_2O_3) after the decomposition of this sample amounted to ~65% of the total sample mass. Assuming that each HA group in the film chelated one Fe^{3+} ion, from which the Fe_2O_3 residue was ultimately formed, the mass of the residue was estimated to be ~50%. The sample that was incubated in 0.1 aqueous EDTA solution after chelation to remove the ions demonstrated the thermal decomposition profile similar to the one of the as-synthesized film (Fig. 12).

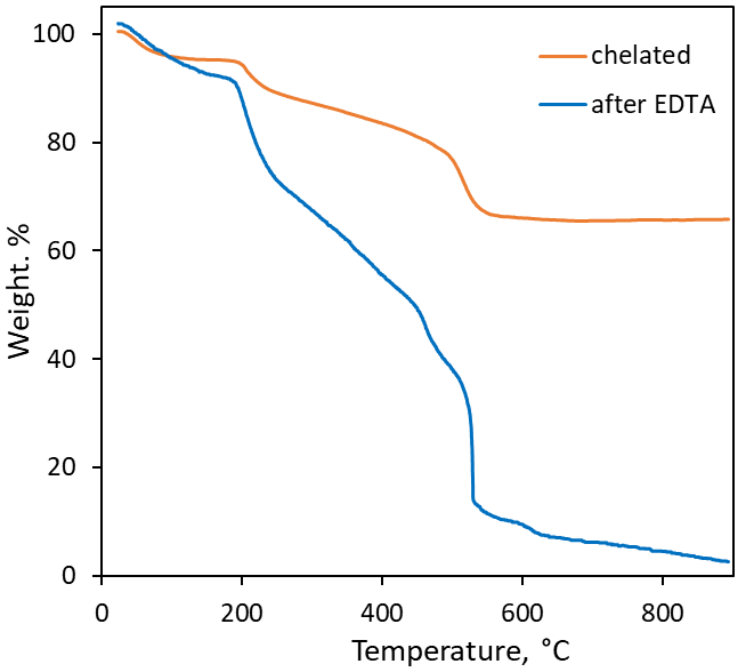

Figure 5.14. Thermograms (recorded in air) of a free-standing HA-pNBDAC after chelation of Fe^{3+} and after chelation of Fe^{3+} and subsequent removal of the ions by immersion into 0.1 M EDTA for 2h.

Conclusions

We developed a new method for fabrication of ROMP-type polymer films and demonstrated its capabilities for preparation of surface-bound and free-standing films with thicknesses of up to ~20 μm and various functionalities, including perfluorinated side chains, pDCPD, reactive pNBOH and pNBDAC scaffolds for further modification, and a random copolymer of pDCPD and pNBDAC.

We illustrated a number of post-polymerization modification procedures for pNBDAC to obtain polymers of practical importance, focusing on the synthesis of metal-chelating hydroxamic acid functional groups by reaction of pNBDAC with hydroxylamine. Inherently transparent free-standing HA-pNBDAC films exhibited a visible color change upon chelation with Fe^{3+} and Zn^{2+}, and the peaks corresponding to the HA complexes with these ions could be detected via UV-vis spectroscopy. The ion complexation could be reversed by incubation of the films in 0.1 M EDTA solution. The HA groups attached to the cyclic olefin backbone decomposed at ~200 °C, which is in agreement with the reports on thermal decomposition of HA moieties within other polymers. Based on the TGA of HA-pNBDAC films chelated with Fe^{3+}, the maximum ion loading is estimated as two ions per the repeat unit of the polymer (i.e., each HA group can chelate one Fe^{3+}).

Chapter VI

CURE MONITORING AND CHARACTERIZATION OF EPOXY/AMINE NETWORKS, MODIFIED WITH 1-BUTYL-3-METHYLIMIDAZOLIUM TETRAFLUOROBORATE IONIC LIQUID

Introduction

ILs possess multiple attractive properties such as thermochemical stability, low volatility, nonflammability, high ionic conductivity, catalytic activity, and recyclability[265–267]. A wide range of anions and cations can be combined to synthesize potentially at least a million different binary and 1018 ternary ILs[267]. This means that the properties of ILs are very versatile and can be tuned for specific purposes, which makes them remarkable as functional additives for modification of polymers.

Epoxy/IL systems are desired in various capacities for industrial applications. ILs can be used as curing agents for epoxies[268–270], while the addition of only a few wt. % of IL to epoxy resins can modify the resulting morphologies and enhance thermomechanical behavior[271], ionic conductivity[269,272,273], and scratch resistance[274]. Epoxy/IL compositions have also demonstrated remarkable potential for developing structural electrolytes[275–277] due to their improved mechanical performance combined with high thermal and chemical stability. In order to facilitate the practical applications of epoxy/IL systems, researchers need to better understand the interactions of different epoxies and ILs and their effect on cure kinetics, and mechanical and electrical properties of the resulting materials.

The morphology and properties of resulting epoxy/IL compositions are largely determined by the preparation process parameters. Curing is a crucial step in fabrication of epoxy-based products. By varying curing conditions, significant versatility for preparation of epoxy/IL networks can be achieved[272,278,279], while inadequate curing will result in inferior product properties. The curing reactions are complex processes evidenced by changes in viscosity[280–282], conductivity[283], and dielectric properties[282,284] of epoxy

networks. Cure monitoring is necessary for selection of appropriate curing conditions and optimization of the materials' performance.

Miscellaneous analytical methods have been developed for cure reaction characterization and cure monitoring. The differential scanning calorimetry (DSC) technique, based on measuring the enthalpy of exothermal cure reactions, has become an industry standard for analysis of cure kinetics[188,189]. Reaction kinetics are characterized based on the assumption that the heat of reaction is directly proportional to the extent of the reaction. This assumption is reasonable for simple reactions but not obviously valid for the complex crosslinking reactions that occur as epoxies polymerize[188]. Despite the significance of DSC, difficulty in distinguishing between cure reactions and other heat-related phenomena is an inherent drawback of the method. The usage of DSC is confined to laboratories for analyzing small samples under ideal conditions.

Spectroscopy methods, such as Raman[189,285] and infrared (IR)[285,286], can be suitable for in situ cure monitoring. Both qualitative and quantitative information can be obtained by these techniques, although their use in epoxy systems is quite restricted because the location and intensity of the spectral peaks are influenced by refractive index, color, and fluorescence characteristics of a sample, and ambient conditions. Peak attribution can also be challenging as some phenomena do not correspond exclusively to perturbations in epoxy networks[286]. Data interpretation gets even more complicated with addition of an IL due to possible overlapping of the IL cation peak and the epoxy peak.

Dielectric analysis (DEA) is one of the most convenient methods for in situ cure monitoring of thermosets developed to date. Numerous dielectric studies of epoxy-amine systems have been published[189,282]. The change in dielectric properties during cure is attributed to the following processes: (1) decrease of ionic conductivity as a result of diminishing ion mobility in the medium due to increasing viscosity; (2) orientation and oscillation of permanent dipoles in the electric field; and (3) decrease of

dipolar moment per unit volume due to the increase of chain length, the increase of crosslink density, and the replacement of dipolar moments of amine and epoxy groups by those of new OH dipoles emerging during the reaction[284,287]. Complex dielectric permittivity (ε*) is determined by applying an AC potential at a variable frequency (ω) and measuring output current through the sample. From the amplitude change and phase shift, the dielectric properties of permittivity, ε′, and loss factor, ε″, can be obtained, and ε∗ can be calculated[189]:

$$\varepsilon^*(\omega) = \varepsilon' - j\varepsilon'' \quad (1)$$

The expression (2)[189] was proposed to relate the dielectric properties of the material to its degree of cure (α) and is based on the assumption is that the conductivity should always decrease due to the changes in viscoelastic properties as the curing progresses.

$$\alpha(t) = \frac{\log(\varepsilon_0'') - \log(\varepsilon_t'')}{\log(\varepsilon_0'') - \log(\varepsilon_\infty'')} \quad (2)$$

where ε_∞'', ε_t'', and ε_0'' correspond to the dielectric loss factors of a sample at infinity, time *t*, and at the beginning, respectively.

This prevalent assumption can be erroneous. In some cases[288,289], the interplay between the extrinsic and intrinsic charge carrier contributions can reverse the expected trend. However, the reports of such phenomena are rare. In general, viscosity is considered to be the key factor influencing conductivity, especially in cross-linking polymers. Kranbuehl et al.[290] have established that under isothermal conditions, the logarithm of conductivity followed the progress of the curing reaction closely, whereas the dependence of the estimated degree of cure on the viscosity was strong up to the gelation of the resin. Hence, DEA is regarded as a more sensitive method for cure monitoring than other common techniques[189].

Fundamentally, electrochemical impedance spectroscopy (EIS) and DEA are conducted following the same operational principles and can be referred to as subsets of a universal broadband electrochemical impedance spectroscopy (UBEIS)[180]. The same data can be converted between the dielectric and impedance domains using expressions based on Maxwell equations. However, historically, the “dielectric" and "impedance" spectroscopies are distinguished from one another and have different resolving capabilities[180,291]. DEA uses higher AC voltage amplitudes and often operates at frequencies above 1 kHz, while EIS utilizes low AC voltage (≤ 10 mV) to maintain linearity of signal response, and its operating frequencies range from MHz to μHz. The main advantage of DEA over EIS is its ability to resolve the relaxation processes at a microscopic level. For heterogeneous dielectric medium, EIS should be the method of choice as conductance and capacitance contributions from different elements in a nonhomogeneous medium or from different physicochemical processes are hardly ever resolved by DEA[291].

Similar to complex permittivity, complex impedance (Z^*) is expressed as:

$$Z^*(\omega) = Z' - jZ'' \tag{3}$$

where Z' is the real component and Z'' is the imaginary component. The impedance may also be expressed in an alternative form through its magnitude, $|Z|$, and phase angle, φ:

$$Z^*(\omega) = |Z|e^{j\varphi} \tag{4}$$

Equations (3) and (4) form the basis of the two common methods of impedance data representation, Nyquist diagram (Z'' versus Z') and Bode plane ($\log|Z|$ versus $\log(\omega)$). Both representations are used as they display different features of the data[292].

Electrical equivalent circuits (EEC) are the most widely used tool for EIS data integration. These circuits are analogs rather than models as they do not pretend to describe the physio-electrochemical properties of the system, but simply reproduce the properties[292]. By adding a sufficient number of elements in the appropriate combination, EEC can be made to closely fit any impedance locus, which represents both the great convenience and the great interpretational danger of equivalent circuit analysis. EEC should be selected on the basis of the chemical and physical properties of the system and should not contain arbitrarily chosen circuit elements[180].

EIS may allow the determination of kinetic constants of diffusive, electrochemical, and chemical processes, and has proven to be extremely valuable for investigations of corrosion phenomena[293], catalytic reaction kinetics[294], charge carrier-transport processes, and structure-property relationships in solid polymeric electrolytes[295,296]. Compared to DEA, researchers employ impedance formalism in the studies of cure reactions much less frequently. In my opinion, EIS merits a closer look for applications in cure monitoring, especially in case of nonhomogeneous systems, such as composites or polymer electrolytes. Several research groups have reported studies on cure kinetics of epoxy/amine systems using EIS [288,297–299]. To the best of my knowledge, no reports on cure monitoring of IL modified epoxy/amine networks by EIS, had been published when this work was in progress.

In this chapter, I report an EIS method for cure monitoring of bisphenol A/F based epoxy resin-polyoxypropylenediamine hardener systems modified with various concentrations of 1-butyl-3-methylimidazolium tetrafluoroborate ([BMIM]BF_4). The systems were found to phase-separate during network formation. The main objective was to observe the curing in ‘real-time’ and study the different processes that occur, such as cross-linking, evolution of conductivity, IL confinement in the epoxy/amine network, and phase separation. The cure kinetics of the epoxy resin were characterized by differential scanning calorimetry (DSC) and the data were used to create a model for comparison with the EIS results.

A phenomenological model was employed to describe the cure kinetics based on EIS data. Mechanical compression testing revealed the impact of IL loading on load bearing properties of the resulting composites. SEM/EDS analyses provided additional insights concerning morphology and phase separation of epoxy/IL systems.

Experimental Methods

Sample preparation

Commercially obtained bisphenol A/F based Super Sap CCR epoxy resin was mixed with the corresponding CCF fast hardener (polyoxypropylenediamine) in the manufacturer's recommended volume ratios (2:1). For epoxy/IL samples, a certain quantity of 1-butyl-3-methyl-imidizolium-tetrafluoroborate ([BMIM]BF_4) was added (5, 10, 20, 40 or 50 wt.%). The samples were mixed for 5 min at 2000 rpm and degassed in a planetary mixer (Thinky mixer, ARE250). The combination of Super Sap CCR/CCS epoxy resin system and [BMIM]BF_4 has been previously utilized in preparation of water-resistant electrolytes for composite structural supercapacitors[277] as [BMIM]BF_4 was observed to yield the best isotropic mixtures with the resin.

Cure monitoring via EIS

EIS was employed to investigate the curing processes of epoxy and epoxy/IL systems at room temperature (23 °C). EIS measurements were performed using two electrode electrochemical cells, as described in Chapter III. The cells were composed of two parallel copper plates (50×20×1mm in dimensions) placed on glass slides and separated by a 50μm layer of insulating Kapton (polyimide) tape (DuPont), called the working electrode (WE) and the counter electrode (CE), respectively. A drop of uncured sample was filled into the 0.28 cm^2 opening punched in the tape (Fig. 6.1). The reference measurement was performed on a cell composed of two electrodes and spacer only and the cell

demonstrated purely capacitive behavior, as expected. The EIS spectra for the samples were measured at different curing times, and at least two samples of each kind were tested.

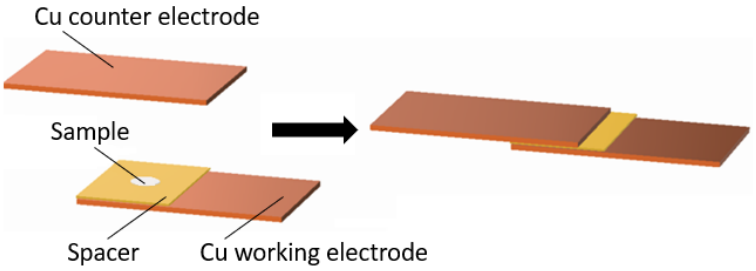

Figure 6.1. The two-electrode cell setup used in EIS experiments.

Cure kinetics characterization by DSC

Measurements to characterize the resin cure kinetics were performed as described in Chapter III. Briefly, the aluminum DSC pan containing 20 ± 3mg sample was placed opposite to an empty reference pan in the DSC cell at a standby temperature of 25°C. The DSC cell was then heated at a constant rate of 2, 5, 15, and 20 °C/min over a temperature range of 25 to 250 °C. The experiments were carried out under the constant flow of nitrogen at 50 mL/min. Measurements of the heat flow during the cure cycle were acquired and exported for further analysis.

Characterization of sample morphology by SEM/EDS

Morphological and elemental analyses of epoxy-amine networks modified with 5, 10, 20, and 40 wt.% of [BMIM]BF_4 ionic liquid were performed as described in Chapter III. Prior to imaging, the samples were mechanically polished in multiple steps, using 240, 320, 400, 600 grit silicon carbide papers, and 5 µm and 1 µm aluminum oxide slurries.

Mechanical Compression Testing

The tests to determine compression strength of epoxy/ionic liquid compositions were conducted on an MTS 810 Test System using the procedure described in ASTM D695 standard[300]. The specimens of pure epoxy, and epoxy with 5, 10, 20, 40, and 50 wt.% of ionic liquid loading were prepared by casting. The samples were poured into molds, cured at room temperature for 24 hours, and subsequently post-cured at 50 °C for 2 hours. After demolding, the samples were deburred and cut to the standard dimensions (right cylinders with diameter of 12.74 ± 2.46 mm and length of 25.61 ± 0.34 or 50.78 ± 0.17 mm). The samples modified with 50 wt.% of ionic liquid did not maintain their structural integrity and, therefore, could not be tested. Four specimens of each composition (5 – 40 wt.%), two longer and two shorter, were tested. The samples were loaded incrementally until the point of fracture, and the maximum load carried by each specimen during the test was recorded.

Results and Discussion

DSC Analysis

Dynamic DSC measurements capture the kinetics at the beginning and the end of the reaction better than isothermal DSC. Complex reaction mechanisms can be more easily interpreted by comparing measurements at different heating rates. The kinetic parameters obtained from the modeling with dynamic DSC data can be further used to describe the isothermal curing processes[301].

The curing of epoxy resin is represented by broad exothermic peaks in dynamic DSC heat flow data, the magnitudes of which increase with increasing heating rate. The baseline adjusted data used to characterize the cure kinetics are presented in Figure 6.2. The baseline offset was determined by fitting a line to the sections before and after the exothermal peaks. The total enthalpy of the reaction (H_T) corresponds to the area under the exothermic curves. For each heating rate, total enthalpy was calculated

by trapezoidal numerical integration of the heat flow over the entire exothermic peak. The H_T values of 278, 285, 288, and 323.55 J/g were found for the heating rates of 2, 5, 15, and 20 °C/min, respectively.

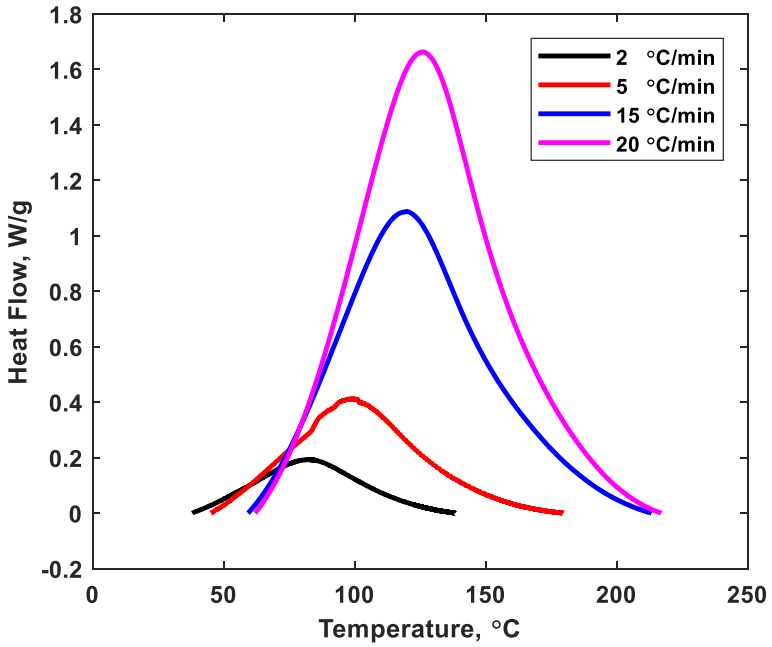

Figure 6.2. Dynamic DSC data selected for analysis after adjustment for the baseline.

The Prout-Tompkins autocatalytic model[189] with four kinetic parameters was found to be in good agreement with the cure behavior of the studied epoxy resin. The differential equation relating the degree of cure to these parameters is as follows:

$$\frac{d\alpha}{dt} = Ae^{\frac{-E_\alpha}{RT}}\alpha^m(1-\alpha)^n \quad (5)$$

where α is the degree of cure of the sample at a given moment of time *(t)*, *A* is the pre-exponential factor, E_α is the activation energy, *R* is the gas constant, *T* is the absolute temperature, m and n are the reaction orders.

The parameters of the model (1) were found by linear least-squares analysis. To optimize the parameters for adequate description of the epoxy cure kinetics at any curing conditions, the DSC data for various heating rates, 2, 5, 15, and 20 °C/min, were used. The R^2 value for fitting to the four datasets was 0.8233. The obtained kinetic parameters (Table 6.1.) were subsequently utilized to predict the cure behavior of the epoxy resin under isothermal conditions at room temperature.

Table 6.1. Kinetic parameters for Super SAP CCR epoxy resin.

Eα, kJ/mol	A, s^{-1}	n	m
44.200	8.3977	1.1556	- 0.0069

EIS Analysis

The examples of evolution of EIS spectra as a function of curing time for epoxy and epoxy/IL samples in the form of Bode plots are presented in Figure 6.3 and 6.4, respectively. The most prominent features of all plots of the type shown below are the systematic variation of characteristic parameters and a good reproducibility of the measured data.

The magnitude of the impedance shows a clear trend of a steady increase with the increasing duration of curing. Such a trend is consistent with most observations of epoxy resins' curing[189,282] and can be explained by diminishing mobility of intrinsic and extrinsic charge carriers as the cross-linking progresses. Therefore, the degree of curing of the samples can be calculated from an empirical relation analogous to (2), which was first reported by Keinle[302] and Race, and later successfully employed by other researchers[298,303]:

$$\alpha(t) = \frac{\log(\rho_t) - \log(\rho_0)}{\log(\rho_\infty) - \log(\rho_0)} \quad (6)$$

where ρ_∞, ρ_t, ρ_0 correspond to the electrical resistivity of a sample at infinity, time t, and at the beginning, respectively.

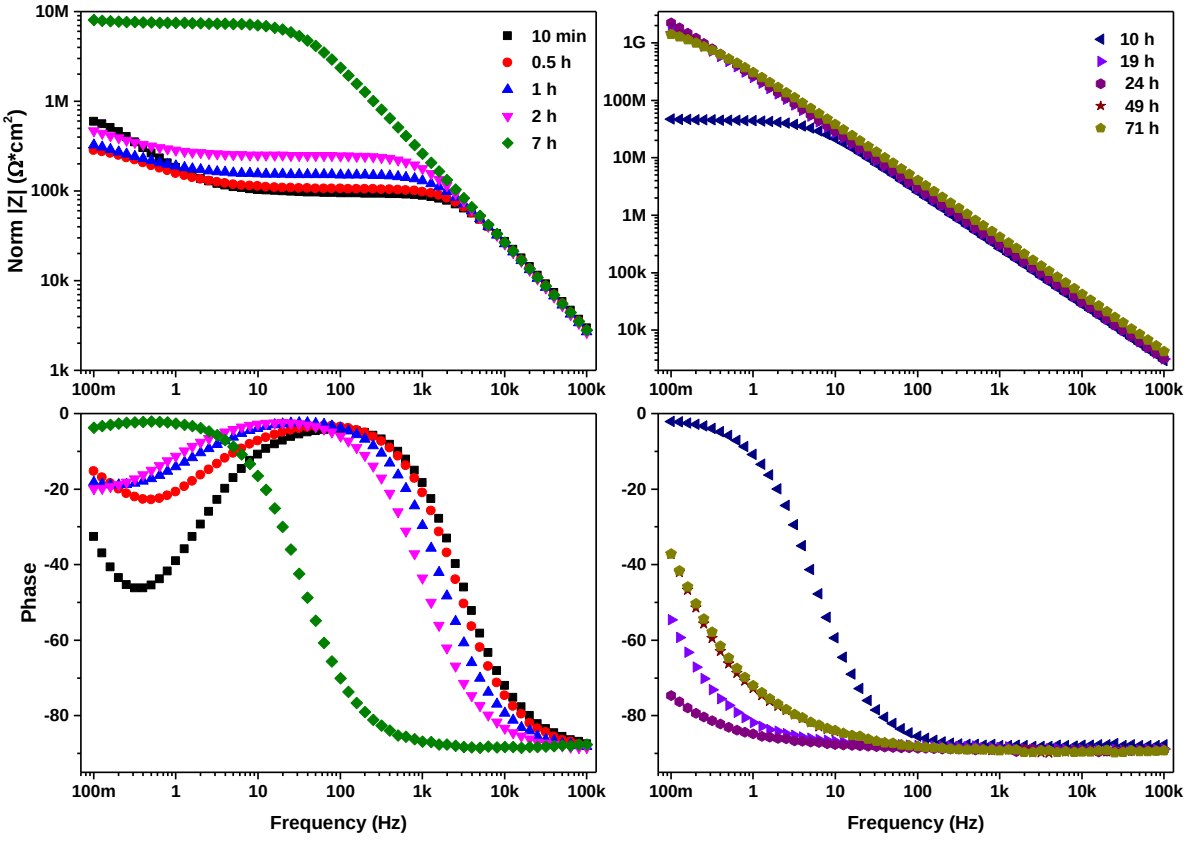

Figure 6.3. Bode plots of unmodified epoxy/amine as a function of curing time.

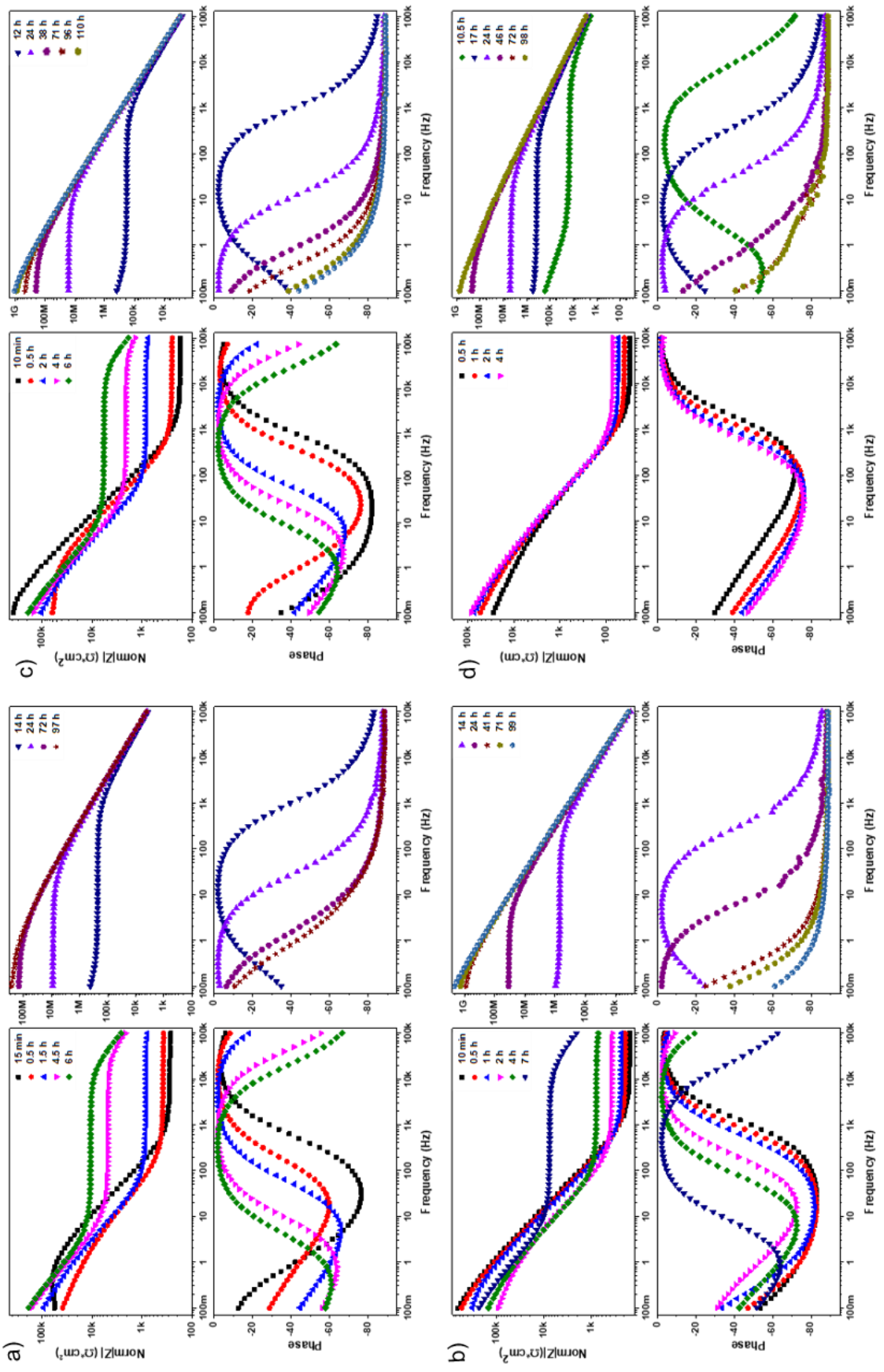

Figure 6.4. Bode plots of epoxy/[BMIM]BF_4 IL compositions as a function of curing time: a) 5 wt.% IL, b) 10 wt.% IL, c) 20 wt.% IL, d) 40 wt.% IL.

Impedance spectra of IL modified epoxy/amine samples displayed high frequency plateau regions of low impedance, indicative of ion migration, which gradually shifted to higher values and lower frequencies as the curing progressed. The value of impedance modulus of the plateau regions, as expected, was inversely proportional to the wt.% of IL loading at initial stages of curing. As the cross-linking increased, the effect of added amount of IL on conductivity of the samples drastically diminished. This can be explained by IL confinement in the epoxy/amine network and formation of bicontinuous structures via polymerization induced phase separation[275,276,279,304]. There is no simple method to predict the phase behavior. The interplay of multiple factors, such as solubility, type, molecular weight, and the amount of the additive, as well as the epoxy/amine ratio and the curing temperature, must all be considered[275]. The studies of dual-phase structures of epoxy/ILs[275,276,304] have demonstrated that ionic conductivity, mechanical strength, and morphology of the materials strongly depend on the IL content. The epoxy studied in the present work was unable to confine 50 wt.% [BMIM]BF_4 loading, as was also reported for a different type of IL and epoxy resin mixture[304]. The absence of IL confinement in the epoxy network is evidenced on Bode plots for this sample (Fig. 6.5) by the presence of two relaxations[305], which are clearly pronounced on the phase angle plots.

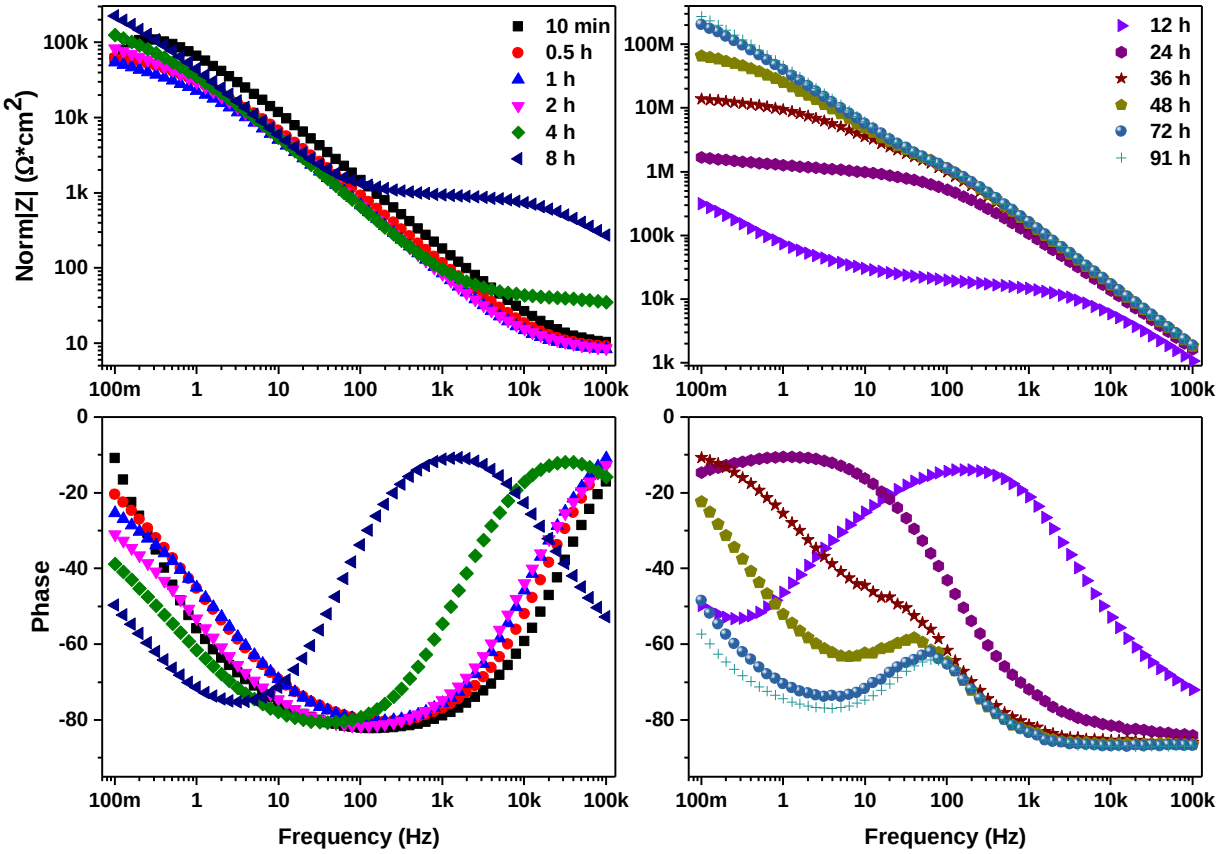

Figure 6.5. Bode plots of epoxy/amine modified with 50 wt.% of IL as a function of curing time.

The changes in impedance spectra with curing in Figures 6.3 – 6.5 represent the evolution of local conduction processes in the sample media, which can be quantitatively described by a suitable, analogous EEC. The EEC shown in Figure 6.6 serves as a good initial model for the systems studied in this work. A sequence of two parallel resistance-capacitance loads represents both bulk and interfacial processes and also accounts for the existence of conductive and insulating phases in heterogeneous materials. The interfacial kinetics, dominating the circuit at low frequencies, is simplified as a parallel combination of Faradaic interfacial resistance R_{int} and a constant phase element CPE_{dl}. Ri_{nt} represents combined effects of charge transfer, adsorption, and diffusion-related resistances, while nonideal double-layer capacitive charging effects are modeled by CPE_{dl}[180]. The impedances of contacts and cables to the electrochemical

cell were found to be negligible in my experiments. The total impedance of the analogous EEC is the sum of bulk and interfacial impedances, the expressions for which are given in Lvovich[180].

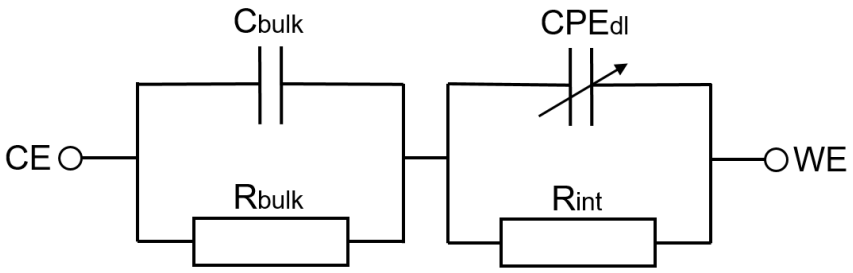

Figure 6.6. EEC model used for EIS data analysis.

In neat epoxy/amine samples (Fig. 6.3) at high frequencies, the dielectric-material resistance rejects the current flow, and the current is almost entirely capacitive, which is reflected by C_{bulk} with a corresponding -90° phase angle. Early in the curing process (10 min–2 h, Fig. 6.3), the samples exhibit a region at medium frequencies separating the bulk media and the interfacial impedance segments. Here, the current flow is dominated by the resistor R_{bulk} the phase angle changes to low absolute values approaching 0°. This region shifts to lower frequencies as the samples cure and become more insulating. At medium to low frequencies the double-layer contribution to the impedance through CPE_{dl} is apparent, with a corresponding increase in the absolute value of the phase angle. At the lowest frequencies, the finite charge-transfer resistor R_{int} becomes pronounced where the phase angle again starts approaching 0°. The magnitude of impedance modulus on Bode plots at low frequencies is the sum of the bulk resistance and the interfacial resistance $R_{bulk}+R_{int}$[180]. At the latest stages of curing, the epoxy/amine samples become highly insulating, the current flow is dominated by C_{bulk} at a wide frequency range with a single low-frequency relaxation and high values of the measured impedance.

In IL-modilied samples (Fig. 6.4), initially the ionic migration process controls the bulk-media conduction, and the bulk resistance exceeds the bulk capacitive impedance at high frequencies, where the impedance response is represented solely by small R_{bulk}.. Later in the curing process, the capacitive current flow, C_{bulk}, dominates increasingly wider frequency ranges, and at the final stages of cure, similar to unmodified samples, only a single low-frequency relaxation is present. For the samples with 50 wt.% of IL (Fig. 6.5), for which the phase separation takes place, the unconfined liquid phase allows for residual bulk ion conductivity, which results in movement of charges through the bulk and their accumulation at the interface and the formation of the double-layer capacitance CPE_{dl}. At frequencies below 1 Hz, R_{int} becomes pronounced.

To determine values of the circuit element parameters, the EEC in Fig. 6.6 was fitted to the obtained impedance spectra using the Simplex algorithm. The analogous EEC had a much better fit (chi-square values on the order of 10^{-4}) for the unmodified epoxy amine system. For ILs the goodness of fit was on the order of 10^{-3} and for a few sampling times 10^{-2}. The inferior fit for the IL-modified system reflected on the quality of modeling of the degree of cure.

Once R_{bulk} values had been determined, the conductivity and resistivity of the bulk material were calculated from the following equation:

$$\sigma = \frac{1}{\rho} = L/R_{bulk}A \qquad (7)$$

where A is the working area of the electrodes in cm^2, L is the spacing between the electrodes in cm, σ is conductivity in S/cm, and ρ is resistivity in Ω cm. Model estimated and calculated parameters for the samples at selected cure durations are presented in Table 6.2. The values of uncertainty in estimations are listed with each corresponding parameter, and for the calculated data, the values of the propagating errors resulting from the uncertainties are given.

Using the calculated electrical resistivity at different time points of the curing process, the degree of cure was estimated from the equation (6). The comparison between the degree of cure determined using EIS and DSC is shown in Figure 6.7. While DSC predicts much faster curing during the initial period, both techniques are in better agreement at the later stages of cure, indicating the degree of cure of 0.98 (DSC) and 0.92 (EIS) at 20 h and 0.99 and at 24 h. Interestingly, the model-estimated bulk resistance of epoxy/amine samples dropped after 24 h. This phenomenon requires further investigation.

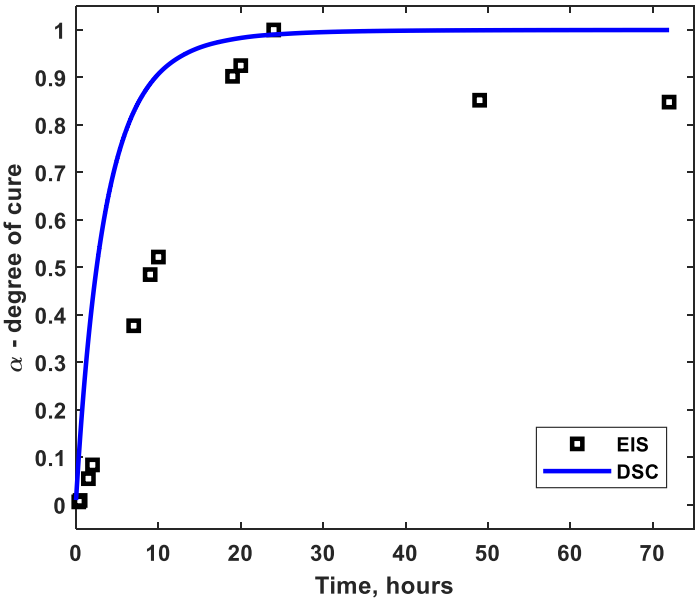

Figure 6.7. Degree of cure under isothermal curing of epoxy/amine system at room temperature (25°C) estimated from EIS and modeled based on DSC data.

Table 6.2. EEC parameters estimated by model fitting and calculated properties of epoxy/amine networks

Epoxy/Amine										
Cure Duration	0.5 h		10 h		24 h		49 h		72 h	
	Value	± Error	Value	± Error	Value	± Error	Value	± Error	Value	± Error
Rbulk, Ω cm2	1.04E+05	7.2E+02	3.84E+07	2.7E+06	9.51E+09	9.0E+08	1.73E+09	3.4E+07	1.65E+09	3.3E+07
Cbulk, F/cm2	5.75E-10	4.4E-12	6.95E-10	4.2E-11	6.77E-10	1.3E-11	6.53E-10	1.4E-11	6.88E-10	1.8E-11
Rint, Ω cm2	2.64E+05	1.3E+04	7.58E+06	2.6E+06	8.83E+07	2.3E+07	8.84E+07	9.8E+06	1.15E+08	1.2E+07
CPEdl, S·s^α/cm^2	3.23E-06	1.2E-07	1.15E-08	8.1E-09	3.47E-09	3.3E-10	1.29E-09	5.7E-11	1.14E-09	4.9E-11
α	7.22E-01	1.9E-02	8.79E-01	4.0E-02	9.46E-01	5.6E-03	9.69E-01	3.2E-03	9.71E-01	2.9E-03
Goodness of Fit	7.70E-05		4.95E-05		2.28E-04		5.96E-04		7.63E-04	
σ, S/cm	4.87E-08	3.4E-10	1.32E-10	9.4E-12	5.34E-13	5.1E-14	2.94E-12	5.8E-14	3.08E-12	6.2E-14
ρ, Ωcm	2.06E+07	1.4E+05	7.56E+09	5.4E+08	1.87E+12	1.8E+11	3.40E+11	6.7E+09	3.25E+11	6.5E+09
Epoxy/Amine + 5wt.% [BMIM]BF4										
Cure Duration	0.5 h		14 h		24 h		72h		97h	
	Value	± Error	Value	± Error	Value	± Error	Value	± Error	Value	± Error
Rbulk, Ω cm2	3.59E+02	2.4E+00	5.16E+05	3.0E+04	6.34E+06	3.4E+05	1.08E+08	2.1E+06	1.96E+08	2.8E+06
Cbulk, F/cm2	5.28E-10	8.6E-11	4.90E-06	1.2E-07	1.21E-09	1.2E-10	1.34E-09	6.2E-11	1.32E-09	3.9E-11
Rint, Ω cm2	4.23E+04	7.2E+02	2.29E+05	1.2E+03	2.27E+06	3.5E+05	2.93E+07	2.1E+06	3.58E+07	1.9E+06
CPEdl, S·s^α/cm^2	1.36E-05	2.0E-07	1.58E-09	5.8E-11	1.36E-09	1.1E-10	9.51E-10	2.9E-11	9.47E-10	2.3E-11
α	7.55E-01	3.1E-03	9.02E-01	3.3E-03	9.34E-01	4.0E-03	9.52E-01	2.2E-03	9.53E-01	2.2E-03
Goodness of Fit	6.48E-03		7.83E-04		6.73E-04		1.27E-03		2.17E-03	
σ, S/cm	1.41E-05	9.3E-08	9.85E-09	5.8E-10	8.01E-10	4.3E-11	4.69E-11	9.2E-13	2.59E-11	3.7E-13
ρ, Ωcm	7.07E+04	4.7E+02	1.02E+08	6.0E+06	1.25E+09	6.6E+07	2.13E+10	4.2E+08	3.86E+10	5.4E+08
Epoxy/Amine + 10wt.% [BMIM]BF4										
Cure Duration	0.5 h		12 h		24 h		71 h		96 h	
	Value	± Error	Value	± Error	Value	± Error	Value	± Error	Value	± Error
Rbulk, Ω cm2	2.48E+02	1.7E+00	5.16E+05	2.5E+04	1.22E+07	7.5E+05	4.39E+08	7.2E+06	1.09E+09	2.3E+07
Cbulk, F/cm2	6.82E-10	1.2E-10	4.56E-06	9.5E-08	1.47E-09	1.6E-10	1.09E-09	3.9E-11	1.12E-09	3.3E-11
Rint, Ω cm2	6.46E+04	6.5E+02	1.84E+05	1.0E+03	3.82E+06	7.7E+05	4.43E+07	6.0E+06	8.99E+07	9.9E+06
CPEdl, S·s^α/cm^2	2.92E-06	4.2E-08	1.65E-09	5.9E-11	1.84E-09	2.1E-10	1.92E-09	1.1E-10	1.76E-09	7.7E-11
α	8.99E-01	2.6E-03	9.27E-01	3.2E-03	9.47E-01	4.3E-03	9.57E-01	3.1E-03	9.61E-01	2.7E-03
Goodness of Fit	5.37E-03		9.55E-04		5.00E-04		6.11E-04		8.22E-04	
σ, S/cm	2.05E-05	1.4E-07	9.84E-09	4.8E-10	4.16E-10	2.6E-11	1.16E-11	1.9E-13	4.68E-12	9.9E-14
ρ, Ωcm	4.88E+04	3.3E+02	1.02E+08	4.9E+06	2.40E+09	1.5E+08	8.64E+10	1.4E+09	2.14E+11	4.5E+09
Epoxy/Amine + 20wt.% [BMIM]BF4										
Cure Duration	0.5 h		14 h		24 h		71 h		96 h	
	Value	± Error	Value	± Error	Value	± Error	Value	± Error	Value	± Error
Rbulk, Ω cm2	1.88E+02	1.3E+00	6.14E+05	4.5E+03	1.12E+06	1.9E+05	1.61E+09	3.3E+07	4.53E+09	2.0E+08
Cbulk, F/cm2	5.24E-10	1.6E-10	6.57E-10	4.8E-12	2.42E-09	2.1E-10	7.47E-10	2.0E-11	6.63E-10	1.5E-11
Rint, Ω cm2	8.18E+05	1.7E+04	1.70E+09	5.4E+11	3.26E+07	2.8E+05	8.33E+07	1.3E+07	1.13E+08	2.2E+07
CPEdl, S·s^α/cm^2	1.67E-06	1.5E-08	3.08E-06	1.9E-07	9.16E-10	2.3E-11	1.89E-09	1.2E-10	2.27E-09	1.7E-10
α	9.27E-01	1.7E-03	4.42E-01	6.7E-03	9.60E-01	2.4E-03	9.50E-01	3.6E-03	9.49E-01	4.2E-03
Goodness of Fit	2.16E-03		9.51E-03		4.43E-04		5.05E-04		3.55E-04	
σ, S/cm	2.70E-05	1.9E-07	8.27E-09	6.1E-11	4.54E-09	7.7E-10	3.16E-12	6.5E-14	1.12E-12	4.9E-14
ρ, Ωcm	3.70E+04	2.6E+02	1.21E+08	8.9E+05	2.20E+08	3.7E+07	3.16E+11	6.5E+09	8.91E+11	3.9E+10
Epoxy/Amine + 40wt.% [BMIM]BF4										
Cure Duration	0.5 h		12 h		24 h		72 h		96 h	
	Value	± Error	Value	± Error	Value	± Error	Value	± Error	Value	± Error
Rbulk, Ω cm2	2.63E+01	2.3E-01	2.65E+05	6.9E+03	4.29E+05	6.4E+04	9.17E+08	2.0E+07	4.70E+08	7.7E+06
Cbulk, F/cm2	1.62E-16	1.3E-09	6.21E-06	7.8E-08	2.31E-09	1.8E-10	1.41E-09	2.4E-11	1.56E-09	3.2E-11
Rint, Ω cm2	2.52E+04	3.5E+02	3.60E+04	2.0E+02	4.35E+06	6.4E+04	5.87E+07	3.0E+06	4.68E+07	2.4E+06
CPEdl, S·s^α/cm^2	1.71E-05	2.1E-07	5.35E-09	2.8E-10	1.90E-09	9.7E-11	1.42E-09	3.3E-11	1.35E-09	3.1E-11
α	7.95E-01	2.0E-03	8.53E-01	4.3E-03	9.33E-01	3.5E-03	9.63E-01	2.3E-03	9.64E-01	2.2E-03
Goodness of Fit	1.89E-02		6.08E-03		9.37E-04		1.54E-03		1.62E-03	
σ, S/cm	1.93E-04	1.7E-06	1.92E-08	5.0E-10	1.18E-08	1.8E-09	5.54E-12	1.2E-13	1.08E-11	1.8E-13
ρ, Ωcm	5.19E+03	4.5E+01	5.21E+07	1.4E+06	8.44E+07	1.3E+07	1.80E+11	3.9E+09	9.26E+10	1.5E+09
Epoxy/Amine + 50wt.% [BMIM]BF4										
Cure Duration	0.5 h		12 h		24 h		72 h		97 h	
	Value	± Error	Value	± Error	Value	± Error	Value	± Error	Value	± Error
Rbulk, Ω cm2	8.29E+00	1.0E-01	3.29E+05	5.7E+03	4.51E+05	1.1E+04	8.93E+05	2.8E+04	7.80E+05	2.6E+04
Cbulk, F/cm2	2.28E-11	4.3E-09	2.84E-06	3.0E-08	2.02E-09	3.1E-11	2.04E-09	4.5E-11	2.05E-09	4.8E-11
Rint, Ω cm2	6.00E+04	6.5E+02	2.36E+04	1.7E+02	9.59E+05	1.4E+04	9.02E-01	2.1E-03	9.12E-01	2.1E-03
CPEdl, S·s^α/cm^2	4.30E-06	4.8E-08	6.32E-08	2.8E-09	4.73E-08	2.9E-09	4.73E-09	4.2E-11	4.13E-09	3.5E-11
α	8.69E-01	1.5E-03	7.11E-01	3.9E-03	7.48E-01	4.8E-03	9.02E-01	2.1E-03	9.12E-01	2.1E-03
Goodness of Fit	9.10E-03		3.71E-02		1.12E-02		3.05E-03		2.03E-03	
σ, S/cm	6.13E-04	7.6E-06	1.54E-08	2.7E-10	1.13E-08	2.8E-10	5.69E-09	1.8E-10	6.51E-09	2.2E-10
ρ, Ωcm	1.63E+03	2.0E+01	6.48E+07	1.1E+06	8.87E+07	2.2E+06	1.76E+08	5.5E+06	1.54E+08	5.2E+06

The cure kinetics estimated for IL-modified samples based on the EIS data (Fig. 6.8) indicates that the samples with 5 – 40 wt.% IL loadings cured slower compared to unmodified epoxy, which is explained by the plasticizing effect of IL. The samples achieved the maximum cross-linking at 72 h after mixing. A significant dependence of the curing rate on the amount of added IL was not detected as the data points for the samples containing 5, 10, 20, and 40 wt.% practically fall on the same curve. The cure kinetics estimated for the sample with 50 wt.% IL loading was much different from that of the other samples. While according to the model this sample also reaches its fully cured state at 72 h, the degree of cure at 12 h is estimated at 0.9. There are several possible reasons for such a result. First, equation (6) has questionable validity for the estimation of the curing degree of the 50 wt.% IL-modified samples because there is no straightforward dependence of the ionic conductivity on the material's viscosity due to the insufficient confinement of IL. Second, the modeling precision with the simplified EEC was lower for these samples (10% error) due to their more complex dielectric response. However, there is a strong possibility that the samples containing 50wt.% of IL had a limited ability for cross-linking that resulted from the failure to confine the IL, and these samples approached their maximum network density much earlier in the process.

Overall, given that no attempt to control the ambient room temperature and humidity during the EIS measurements was made, the performance of the technique in cure monitoring is impressive, which underlines the applications of this method for in situ cure monitoring.

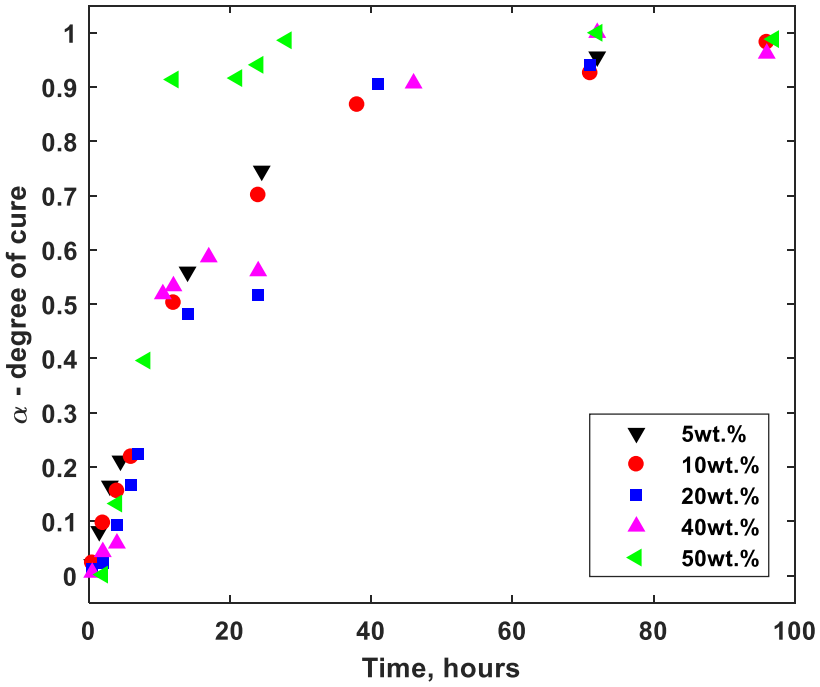

Figure 6.8. Degree of cure of samples modified with various wt.% of IL estimated from EIS data.

IL-loading dependent conductivity and compression strength

The dependence of bulk conductivity and compression strength of the fully cured samples on the amount of IL loading is presented in Figure 6.9. The casted 50 wt.% IL-modified samples for compression testing did not achieve structural integrity during curing, and therefore, the data point for these samples could not be obtained. The compression strength of the epoxy/amine decreased with the increasing wt.% of added IL. The amount of IL loading had a slightly unexpected effect on the ionic conductivity of epoxy/amine networks. The addition of 5 wt.% of [BMIM]BF_4 resulted in an order-of-magnitude increase in the ionic conductivity of the epoxy/amine (from 10^{-12} to 10^{-11} S/m), while 10 – 40 wt.% IL loadings yielded less conductive products.

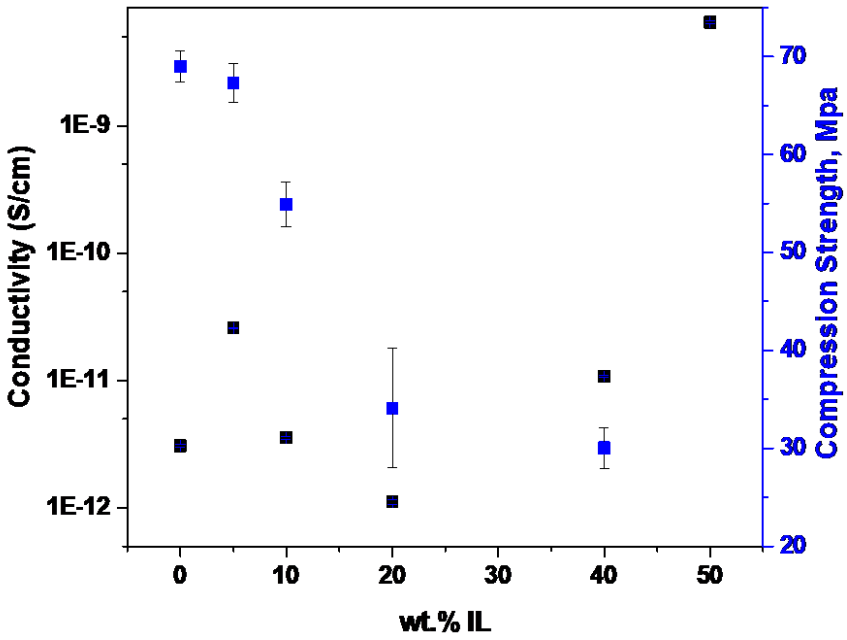

Figure 6.9. The conductivity (black) and compression strength (blue) of the fully cured samples as a function of IL content.

This seemingly abnormal behavior could be explained by the limited miscibility of [BMIM]BF_4 with the selected epoxy. While 5 wt.% of IL could form a more evenly distributed percolating network, the larger IL loadings could result in phase separation and accumulation of IL into clusters separated by epoxy/amine network, which would in turn decrease the overall materials' ability for ion conduction. SEM/EDS studies of the samples' morphology were conducted to gain more insight into this phenomenon.

IL-loading dependent morphology of cured epoxy/IL blends

Figure 6.10 demonstrates SEM images for unmodified epoxy and epoxy/IL systems containing various wt.% of IL. The addition of IL significantly affects the morphology of the epoxy/amine network: phase separation is taking place, resulting in microstructures that contain IL droplets dispersed in the bulk epoxy phase. All the IL-modified samples have closed pore structures, and the density and size of the pores demonstrate a steady increase with the increasing content of IL. The pore diameter reaches ~ 0.6 μm,

~ 1-1.3 μm, and ~ 1.5 μm for the samples containing 5 wt.%, 10 wt.%, and 20 wt.% of IL, respectively. With the addition of 40 wt.% of IL the diameter of the pores increases dramatically up to ~ 65 μm.

Using EDS elemental analysis, the IL domains can be distinguished by the fluorine (F) signature, F is present only in samples modified with [BMIM]BF_4. The full elemental maps are presented in Figure 6.11. Notably, Al is present in the samples with pores 1 μm in diameter or larger due to the alumina slurry particles that were entrapped in the pores during polishing. In epoxy networks containing 5wt.% of [BMIM]BF_4, the IL is well-distributed, and no IL agglomeration is observed. The samples with 10wt.%, 20wt.%, and 40 wt.% of [BMIM]BF_4 demonstrate some dispersion of the IL through the bulk of the epoxy, but spherical clusters of the IL can be clearly distinguished by the F signature.

The revealed morphology provides an explanation for the loss of the mechanical properties from the microstructural point of view. The size and density of the pores increases with the increasing content of IL, which in turn causes the observed decrease in compressional strength.

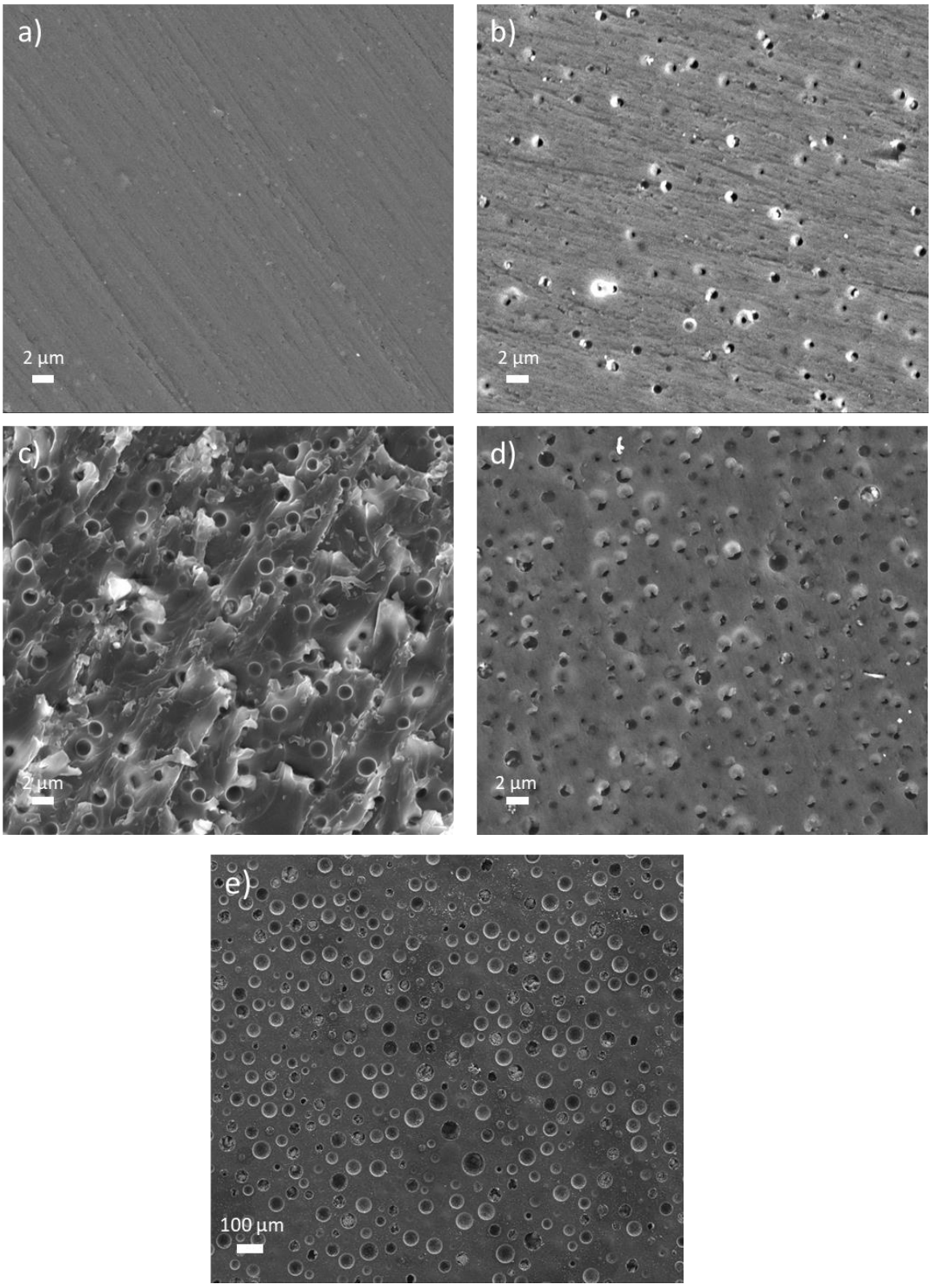

Figure 6.10. SEM micrographs of: a) unmodified epoxy and epoxy modified with various amounts of [BMIM]BF_4 IL b) 5 wt.%, c) 10 wt.%, d) 20 wt.%, e) 40 wt.%.

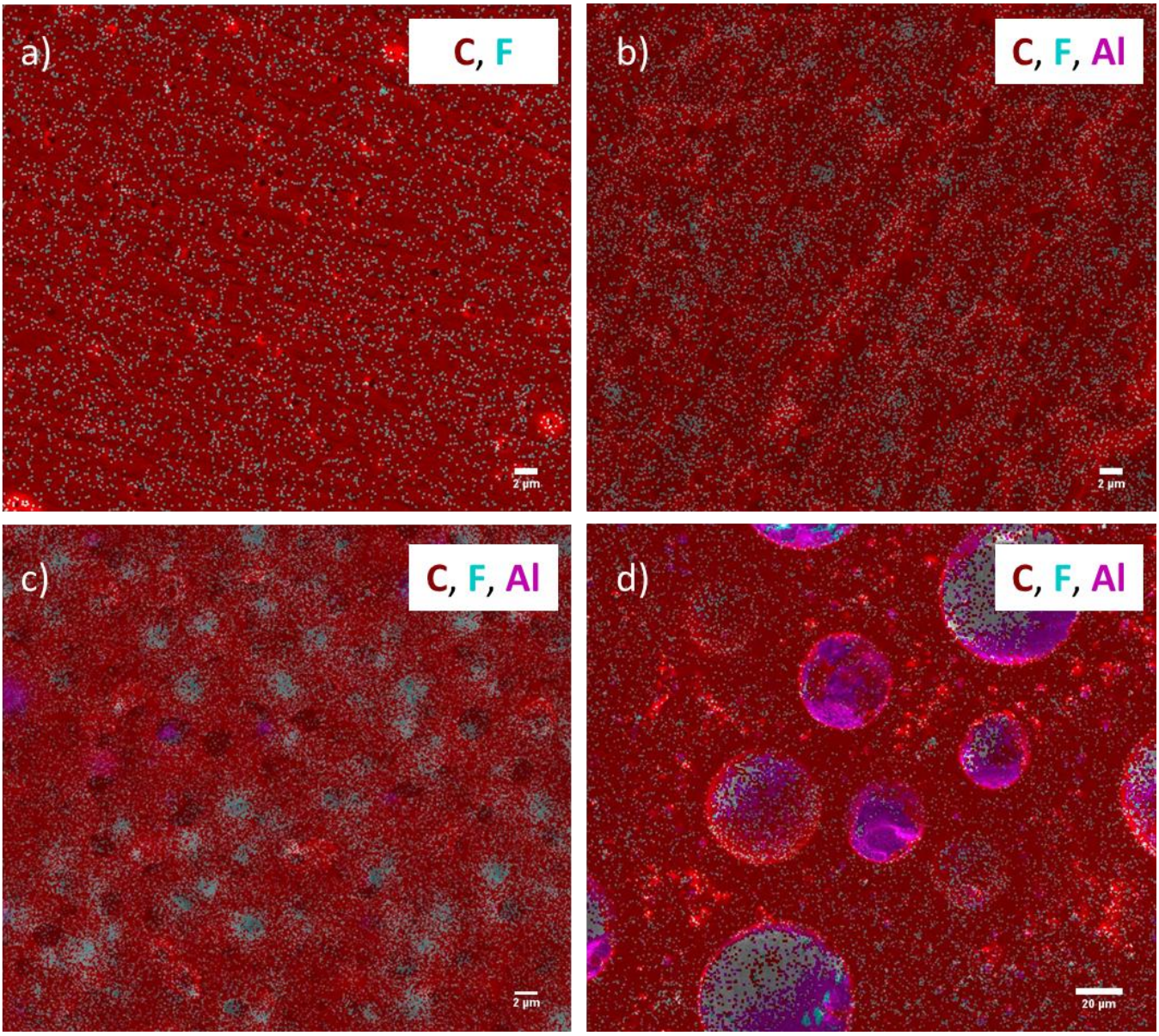

Figure 6.11. Complete EDS elemental maps of epoxy modified with various amounts of [BMIM]BF_4:

a) 5 wt.%, b) 10 wt.%, c) 20 wt.%, d) 40 wt.%.

Conclusions

Epoxy/amine networks containing various amounts of [BMIM]BF_4 were prepared by curing epoxy/amine in the presence of the IL. The studied epoxy system was able to confine up to 40 wt.% of the IL. The samples with 50 wt.% of [BMIM]BF_4 could not develop sufficient cross-link density for the IL confinement and did not fully solidify.

The loading of 5 wt.% of the IL improved the ionic conductivity of epoxy/amine by an order of magnitude, while reducing its compression strength only by 2.5%. A seemingly abnormal trend in conductivity was observed: the conductivity of the samples with 5 wt.% of [BMIM]BF_4 was higher than that of other samples with 10, 20, and 40 wt.% of the IL. The investigations into the samples' morphology provided explanation for this phenomenon: in the sample containing 5 wt.% of [BMIM]BF_4, the IL was randomly dispersed throughout the bulk, providing small conductive grains with relatively low grain boundary resistance. The conductivity of the 10 wt.% [BMIM]BF_4-modified sample approaches that of the pure epoxy. The conductivity of the epoxy with 20 wt.% [BMIM]BF_4 sample drops below the pure epoxy value due to the increased sizes of pores as well as the increase in size and density of IL agglomerates. The large clusters result in higher grain boundary resistance: here, the current has to travel across the larger insulating grain boundaries, while a larger quantity of small IL clusters provides a somewhat "shortened" path for the current. So, even the 40 wt.% [BMIM]BF_4-modified sample conductivity, while better than that of 10 wt.% [BMIM]BF_4/epoxy sample, does not surpass that of the sample containing only 5 wt.% of the IL. The significant increase in conductivity is observed only for 50 wt.% [BMIM]BF_4/epoxy, where a continuous conductive path is established, as epoxy/amine networks failed to confine the IL and from a cross-linked 3D network.

DSC and EIS techniques were employed for characterization of epoxy/amine cure kinetics and cure monitoring. While DSC predicted higher curing rates during the initial curing stage, the two

techniques exhibited a good correlation later in the process. EIS is a versatile tool for real time monitoring of reactive processes and dielectric measurements and can also provide valuable information for optimization of materials formulations. At the moment, the nature of estimated cure kinetics remains phenomenological, and the development of fundamental scientific correlations between dielectric and chemo-rheological phenomena is required to realize the full potential of the technique in cure monitoring. The utilization of EIS for complex systems can be hindered by a lack of understanding and ability to differentiate between the multiple molecular-level dielectric phenomena occurring in such systems. Therefore, it is highly recommended to gain some insight into the properties of the studied materials with other complementary techniques prior to EIS analysis.

Chapter VII

SUMMARY AND FUTURE WORK

Summary

The year 2020 marks a century since Hermann Staudinger first published[306] his concept of polymers as long chains of covalently linked molecules[307]. Staudinger's revolutionary insights engendered the era of rational development of functional polymeric materials[308], which have become essential in modern civilization. Through human creativity, synthetic polymers attained performance characteristics far superior to their natural counterparts: we can design polymers on the molecular level, tailoring their chemical structure, chain topology, architecture, and tacticity to achieve the desired thermal, mechanical, electrical, barrier, and stimuli-responsive properties for advanced applications[4].

A crucial task of finding new techniques for obtaining functional polymers and improving the simplicity, efficiency, environmental safety, and commercial applicability of the existing methods stands for the foreseeable future. The current technological and societal challenges persistently call for polymeric materials with enhanced properties and functions. My hope is that this work has made a useful, even if tiny, contribution to the magnificent field of functional polymers.

Most immediately, the facile methods proposed in this work contribute to the pool of techniques that can be utilized in a commercial setting for preparation of functional polymer films with tunable properties.

In Chapter IV, I have described the synthesis of catechol-functionalized methacrylate-type polymer films (dopamine-pGMA) directly from the silicon surfaces. The advantages of the presented route include simplified synthesis procedure (due to elimination of product separations and catechol protection/deprotection steps) and ability to adjust the concentration of the functional groups via post-

polymerization reaction conditions. I also showed a proof-of-concept application of the films for metal ion sorption and sensing.

In Chapter V, I have presented a new method for obtaining a wide range of functional poly(norbornene)-type films, including polymers with omniphobic wetting properties and reactive scaffolds for further modification. I have emphasized the method's capability for facile preparation of both free-standing polymer films and coatings that are robustly bound to the substrates. I showcased a number of post-polymerization modification reactions with polynorbornene containing acid chloride functional groups (pNBDAC), focusing on preparation of hydroxamic acid functionalized free-standing films and their application for chelation of Fe^{3+}.

The Pint's research group had previously utilized the blends of Super Sap CCR/CCS epoxy resin system and 30 – 60 % $[BMIM]BF_4$ ionic liquid (IL) as water-resistant electrolytes for composite structural supercapacitors[277]. In Chapter VI, I have examined the cure kinetics of the epoxy resin containing 5 – 50 wt. % of $[BMIM]BF_4$ and established the trends for electrical conductivity and compression strength versus IL content. Investigations into the morphology of the cured samples helped corroborate the results. Contrary to the initial expectations, the conductivity did not increase linearly with the increasing wt.% of IL, as IL formed separate domains within the bulk epoxy resin upon curing. Among the studied samples, epoxy containing 5 wt.% of IL exhibited the optimum combination of properties.

Future work

The results demonstrating selective sorption of Al^{3+} over Zn^{2+} with dopamine- pGMA (Chapter IV) beg further experiments with an extended range of metal ions and pH conditions. The efficacy of this polymer for selective ion sorption from complex mixtures, e.g., ocean water, would be of interest, especially if the polymer film were grown from porous substrates (with high surface area). I illustrated

the feasibility of the films for ion sensing using the QCM-D technique. Integrating the films into a device with an alternative (to QCM) signal transducer (e.g., microcantilevers, transistors, optical fibers) may result in higher sensitivity and detection limit for the analyte binding.

The advanced goal of this project is to implement a sensor based on the chelating polymer films for early detection of corrosion inside cooling water pipes at nuclear power plants. Such a sensor is feasible with further refinement of the presented technology, and would help extend the lifecycle of the plants, reduce the cost of maintenance, and lower the risk of accidents, which, in turn, could alter the unfavorable public perception of nuclear energy.

In addition, dopamine-pGMA films are potentially useful for applications in energy devices[309–311], and, when chelated with metal ions, could serve as self-healing coatings[221,312] and biopolymers (e.g. antibacterial[313], antimicrobial[202], and antifouling[204] coatings, bio adhesives[201]).

The method for polymer film preparation via spin coating and ROMP presented in Chapter V has prospective applications in an array of industries. However, the mechanisms underlying the process require further elucidation and may provide valuable insights for controlling the properties of the resulting polymer films. The potential capability of the process for obtaining high-quality block copolymer films is exciting and needs to be investigated. Additionally, the environmental impact of the chemical synthesis has not been considered as seriously as it is now. Thus, the ability to regenerate and reuse the excess organometallic ROMP catalyst solution is of crucial importance, as is the ability to prepare biodegradable polymers by this method.

I synthesized polymer films with potentially thermally switchable wetting properties (Chapter V) (based on the report describing polymers with the same structure synthesized in solution by an alternative route[20]), and it would be interesting to characterize their behavior across a broad range of temperatures.

Such thermoresponsive coatings could be useful as smart biomaterials[314], e.g., for controlling cell adhesion[19], in nanomedicine and disease therapy[315].

Free-standing HA-pNBDAC films (Chapter V) demonstrated potential for colorimetric ion sensing applications; therefore, a quantitative analysis of ion chelation through spectroscopy and optical sensing would be beneficial for the further development of this technology. The characterization of ion sorption by HA-pNBDAC polymers is necessary to assess their potential for applications in environmental remediation and analytical application (i.e., ion preconcentration for quantitative determination).

Moreover, other binding (e.g., for specific biomolecule recognition) and signaling moieties (e.g., fluorescent functional groups) could be incorporated into pNBOH and pNBDAC films (Chapter V) via post-polymerization modification, which would expand the scope of sensing applications.

Currently, the development of "smart" polymer films is trending toward multifunctionality[17,316], i.e. independent and simultaneous response to diverse stimuli, for example, temperature and pH[21]. Polymer films discussed in Chapters IV and V excite scientific curiosity as complex multifunctional materials with remarkable physio-chemical versatility imparted by pendant moieties.

Outlook

The future without polymers is unimaginable. What comes to mind when thinking about the polymers of the future? Environmental sustainability[317] is one of the main challenges facing polymer science: obtaining polymers from renewable resources with performance and costs competitive with the current commodity polymers, expansion of green synthesis and processing techniques (consuming less energy and fewer organic solvents), improvements in polymer waste management and recycling procedures (e.g., digital passports for polymer recycling analogous to the one Oak Ridge scientists recently proposed for lithium-ion batteries[318]) will be important.

Integration of multiple stimuli-responsive functions into a single polymer system could ultimately lead to autonomous sensing robots combining energy generation, harvesting, and storage, along with sensory and signal transduction functions. The multifunctionality of such polymers can eventually begin to mimic the wide-spectrum bioresponsiveness of many organic tissues like skin or cellular membranes. Applied in the field of robotics, such materials can begin to expand the overall industrial and social functions of automated systems. The computational applied abilities of robotic systems will be enhanced by a much wider array of input data sourced from smart polymers that can adapt to multiple scenarios and environments rather than relying on a dedicated sensor for each limited function.

Polymers also have a place in the rapidly expanding realm of space exploration. The extreme environments and incredible possibilities of that seemingly limitless frontier dictate an entirely new, multi-functional, and robust family of polymer materials. High vacuum, high radiation, and extreme temperature variance are all major considerations for any material that leaves Earth's atmosphere. This is where self-healing and "rad-hard" materials could extend the operational lifespan of deep space probes and orbital satellite systems. Polymer films with varied sensing capabilities can miniaturize life-sustaining equipment on manned craft, reducing overall mass and growing payload capacity. Alien worlds, once the provenance of science fiction, are now within reach. Analyzing new and hostile environments on other planets will be critical to the development of life sustaining systems for eventual human settlement.

A more down to Earth application of advanced polymers is in healthcare. The global population is growing, and one of the fastest growing demographics is the elderly. Lifespans are longer, due in part to improvements in medical technology. With an aging population, adaptable polymers can create new solutions for blood filtration, selective delivery of pharmaceuticals, respiratory treatments, and other medical innovations. Air quality is of primary concern during times of widespread airborne pathogens.

Polymer sensors can be applied in high-risk environments like nursing homes, schools, and hospitals to clearly display the level of contamination in a particular space.

In the service of research itself, tunable polymers can create huge advantages in laboratory applications. New, miniaturized, multi-sensor instruments, scaffolds for fast throughput reagent screening could make research more streamlined, efficient, and affordable for academia and the private sector. This could have one of the most beneficial effects, shortening the distance between theory and the realization of tomorrow's most impactful concepts.

APPENDIX

SELF-ASSEMBLY AND CHARACTERIZATION OF SURFACTANT-INTERCALATED POLYELECTROLYTE THIN FILMS USED AS ACTIVE LAYERS IN LOOSE NANOFILTRATION MEMBRANES

Introduction

Loose nanofiltration (LNF) membranes with pore sizes of ~ 5 – 10 nm are desirable in applications requiring removal of natural organic matter[319], pharmaceuticals[320], hormones[321], and pesticides[322]. While more effective than ultrafiltration (UF) membranes in separation of small organic molecules[323], LNF membranes have significantly higher permeability, and, therefore, operate at lower pressure gradients than tight nanofiltration (NF) membranes[324].

Compared to conventional methods for preparing active layers of nanofiltration (NF) membranes, layer-be-layer assembly of polyelectrolytes has numerous advantages, including high water permeability[325], low fouling propensity[326], and chlorine resistance[327] of the resulting thin films, as well as elimination of toxic organic solvents from the fabrication process. Integration of an anionic surfactant, sodium dodecyl sulfate (SDS), into the polyethylenimine (PEI)/polystyrenesulfonate (PSS) active layer of LNF membranes was shown[328] to enhance water permeability by more than 5-fold and increase humic acid rejection from 93% to 98%, compared to the reference LNF membranes containing PEI/PSS active layers prepared without SDS. The SDS-intercalated LNF membranes also demonstrated superior permselectivity vs. other membranes that have been used for humic acid removal to date[328].

To gain molecular level insight and possibly find an explanation for the drastically enhanced performance of surfactant-intercalated polyelectrolyte active layers, multilayers of PEI/PSS and

PEI/SDS/PSS were prepared on model Au/Si surfaces for analysis via polarization modulation-infrared reflection absorption spectroscopy (PM-IRRAS).

Experimental Methods

Preparation of polyelectrolyte multilayers on model surfaces

Au/Si substrates were prepared and cleaned as described in Chapter III. The substrates were immersed into 1mM ethanoic solution of mercaptoacetic acid for 14 hours to yield negatively-charged SAMs on the surfaces for the subsequent deposition of PEI through electrostatic interactions. The deposition of the SAMs was confirmed by advancing water contact angle measurement (5°±3 for all samples). The attempts have been made to determine the thickness of the SAMs with ellipsometry, however the values were close to the sensitivity limit of the instrument.

Layer-by-layer deposition of polyelectrolytes and surfactants was conducted using aqueous solutions of neutral pH. The SAM/Au/Si substrates were submerged into a 1.5 g/L solution of PEI for 30 min, then rinsed with DI water. The following layers were assembled by immersion into SDS solution (3.5 g/L) or PSS solution (1.5 g/L) for 30 min with subsequent DI water rinses. The procedure was repeated until the desired number of layers was obtained.

Characterization of polyelectrolyte/surfactant layers

Contact angle goniometry and spectroscopic ellipsometry were performed according to the procedures described in Chapter III.

The measurement of the thickness of the polyelectrolyte films on SAM/Au substrates was conducted using JA Woollam M2000VI Spectroscopic Ellipsometer. Cauchy model for a transparent film (with fixed refractive index of 1.45) on gold was applied to determine the value of the film thickness.

PM-IRRAS was performed using a Bruker Tensor 27 FTIR spectrometer with a PEM-90 photoelastic modulator (Hinds Instruments) and a mercury-cadmium-telluride (MCT) detector with a non-dichroic BaF_2 window. The source beam employed a half-wavelength retardation modulated at a frequency of 50 kHz and set at 80° incident angle to the sample surface. Spectra were acquired over 10 min at a resolution of 2 cm^{-1}.

Results and Discussion

The thicknesses of various polyelectrolyte/surfactant multilayers are shown in Table A.1 below. As expected, the intercalation of SDS leads to increase in thickness, compared to the similar films comprised of two PEI/PSS bilayers. The deposition of another PEI layer results in decrease in thickness, possibly due to the effect of strong electrostatic interactions between the polyelectrolytes as PEI penetrates within the PSS layer.

Table A.1. Ellipsometric thickness of polyelectrolyte/surfactant multilayers.

Sample	Average thickness, nm	Standard deviation, nm
PEI+SDS+PSS+PEI+SDS	5.2	0.3
PEI+SDS+PSS+PEI+SDS+PSS	7.5	0.3
PEI+PSS+PEI+PSS	6.8	0.3
PEI+PSS+PEI+PSS+PEI	5.7	0.1

As interaction of the samples with water is primarily determined by the composition of the surface, contact angle goniometry was performed after deposition of each polyelectrolyte or surfactant layer. Interestingly, no difference between the contact angles of the terminal PSS layer absorbed on PEI or SDS was noticed. In both cases, the advancing water contact angles of 34 °± 3 were measured. The values of

advancing water contact angle systematically and quite reproducibly alternated with deposition of polyelectrolyte (34° ± 3) and SDS (88° ± 3) layers, except when SDS was absorbed on a single PEI layer (possibly due to the substrate effects, as reported in other studies[329]). Such an increase in contact angle suggests that hydrophobic tails of SDS molecules are exposed to the surface, while the anionic headgroups penetrate into the PEI layer[329], as depicted on Fig. A.1.

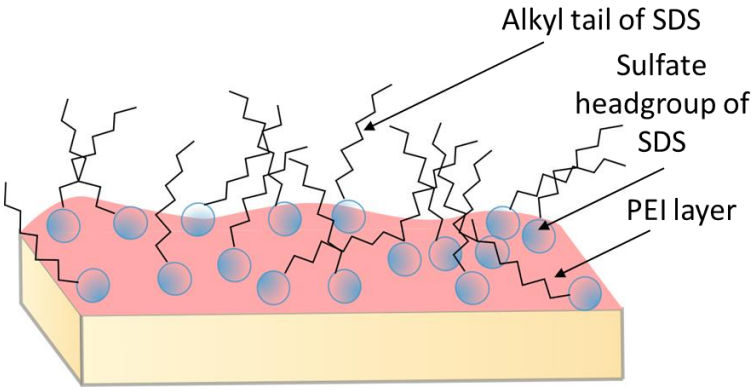

Figure A.1. Schematics of the inferred structure of the terminal SDS layer: hydrocarbon tails of SDS molecules are predominantly aligned towards the surface, while the headgroups penetrate into the PEI layer.

The "fingerprint" portion of the PM-IRRAS spectra of polyelectrolyte/surfactant films is presented in Figure A.2. The signals attributed to PEI are not visible in the acquired IR spectra, possibly because PEI has lower extinction coefficient than PSS and SDS. The interpretation of the IRRA spectra in the polar group region is complicated due to the highly nonlinear baseline in this region[330], as well as a number of overlapping peaks. For example, PEI C-N stretching peak (expected[331] at 1129 cm^{-1}) would overlap with sulfonate SO_3^- anion peak[332] at 1125 cm^{-1}. However, the successful deposition of PEI is imperative for the subsequent absorbance of SDS and PSS layers, as electrostatic and hydrophobic (between the polymer backbone and the surfactant's alkyl tail) interactions stabilize the system[333,334].

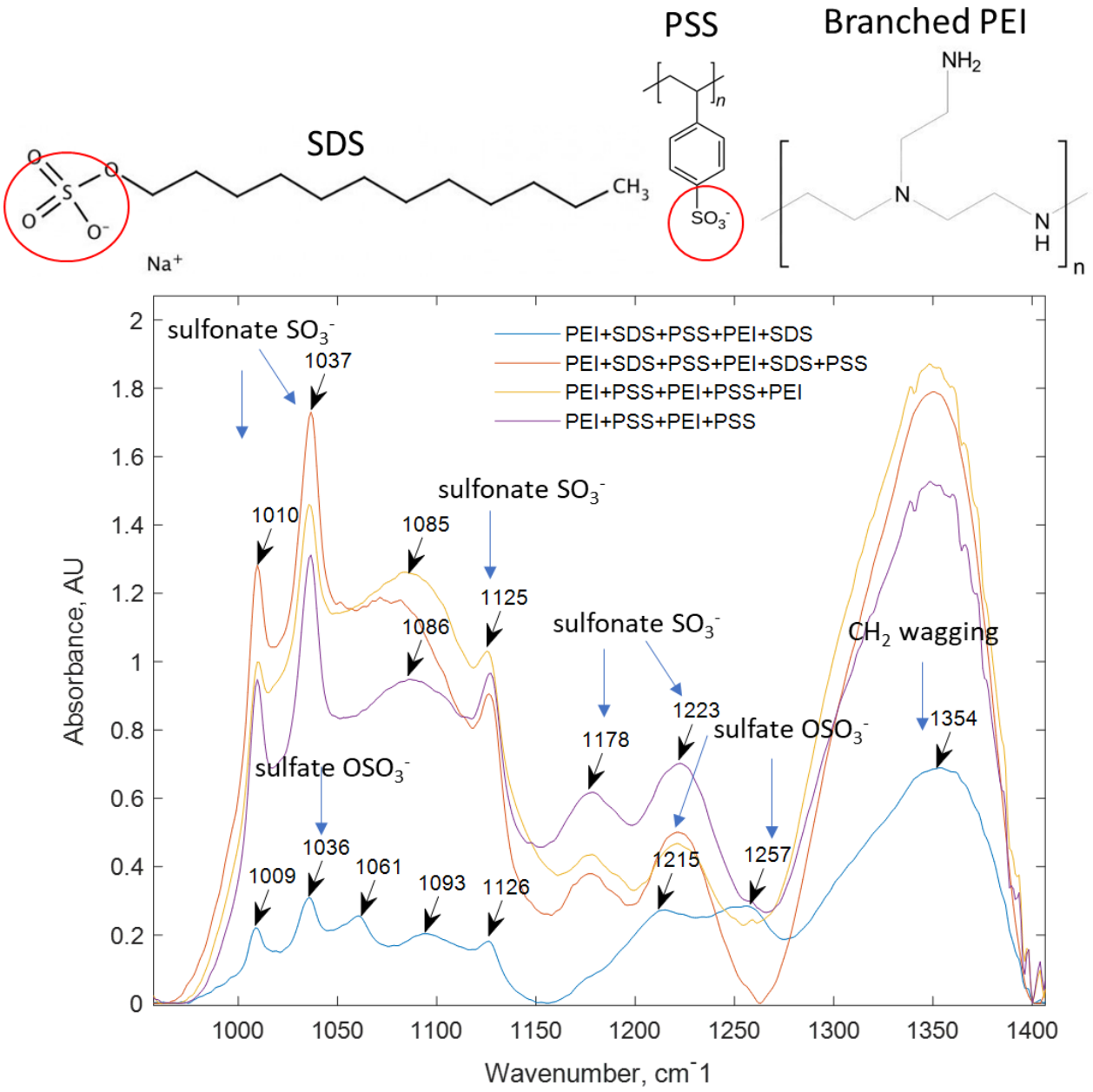

Figure A.2. PM-IRRAS spectra showing sulfonate and sulfate stretching of polyelectrolyte/surfactant films.

The peak at 1061 cm^{-1} (due to sulfate symmetric stretching), indicative of micellar SDS[335], is clearly distinguishable only when SDS is the terminal layer. The peak at 1085 – 1086 cm^{-1} can be attributed to symmetrical vibrations of sulfate and sulfonate moieties interacting with counterions[330,335].

The position of this peak at ~ 1087 cm^{-1} was observed for SDS sulfate groups oriented toward the substrate[336]. When SDS is the terminal layer, the broad asymmetric OSO_3^- stretching doublet is observed at 1215 cm^{-1} and 1257 cm^{-1}. From the separation between the two peaks the conformational structure of SDS can be inferred[335]. While the separations of 32 – 33 cm^{-1} are predicted for liquid crystals, the separation of 42 cm^{-1} observed in this study is consistent with the values for the bulk SDS (39 – 48 cm^{-1})[335].

Below, Figure A.3., which depicts the C-H stretching region of the PM-IRRAS spectra of polyelectrolyte/surfactant films, shows a clear evidence of SDS retention: the symmetric CH_3 stretching peak[169] at ~2960 cm^{-1} is observed only for the films containing SDS, which indicates that SDS adsorbed on PEI is not displaced by rinsing and subsequent deposition of PSS. The asymmetric CH_3 stretching peak, expected[335] at ~ 2873 cm^{-1}, is not visible (similar results for CH_3 stretching bands were obtained via reflection absorption spectroscopy of absorbed SDS monolayers[330]). The presence of primary CH_3 stretching band indicates considerable degree of alignment of SDS alkyl chains[336].

The conformational order of hydrocarbon chains in polyelectrolyte- and polyelectrolyte/surfactant layers is also evident in Figure A.4. The location of asymmetric CH_2 and symmetric CH_2 stretching peaks[169] at 2916 – 2917 cm^{-1} and 2848 cm^{-1}, respectively, suggests high degree of crystallinity (all-*trans* CH_2) in the PEI/PSS and PEI/SDS/PSS layers[330,335]. The samples containing SDS demonstrate increase in the bandwidth of both peaks, possibly indicative of the reduced crystallinity (increased number of gauche CH_2) within the films[330]. When SDS is the top layer, both asymmetric CH_2 and symmetric CH_2 stretching vibrational frequencies shift toward higher values that are characteristic for micelles and liquid crystals[335,337]. The shoulders at ~ 2858 cm^{-1} and ~ 2922 cm^{-1} indicate possible coexistence of non-crystallized SDS and hydrated crystalline SDS[335].

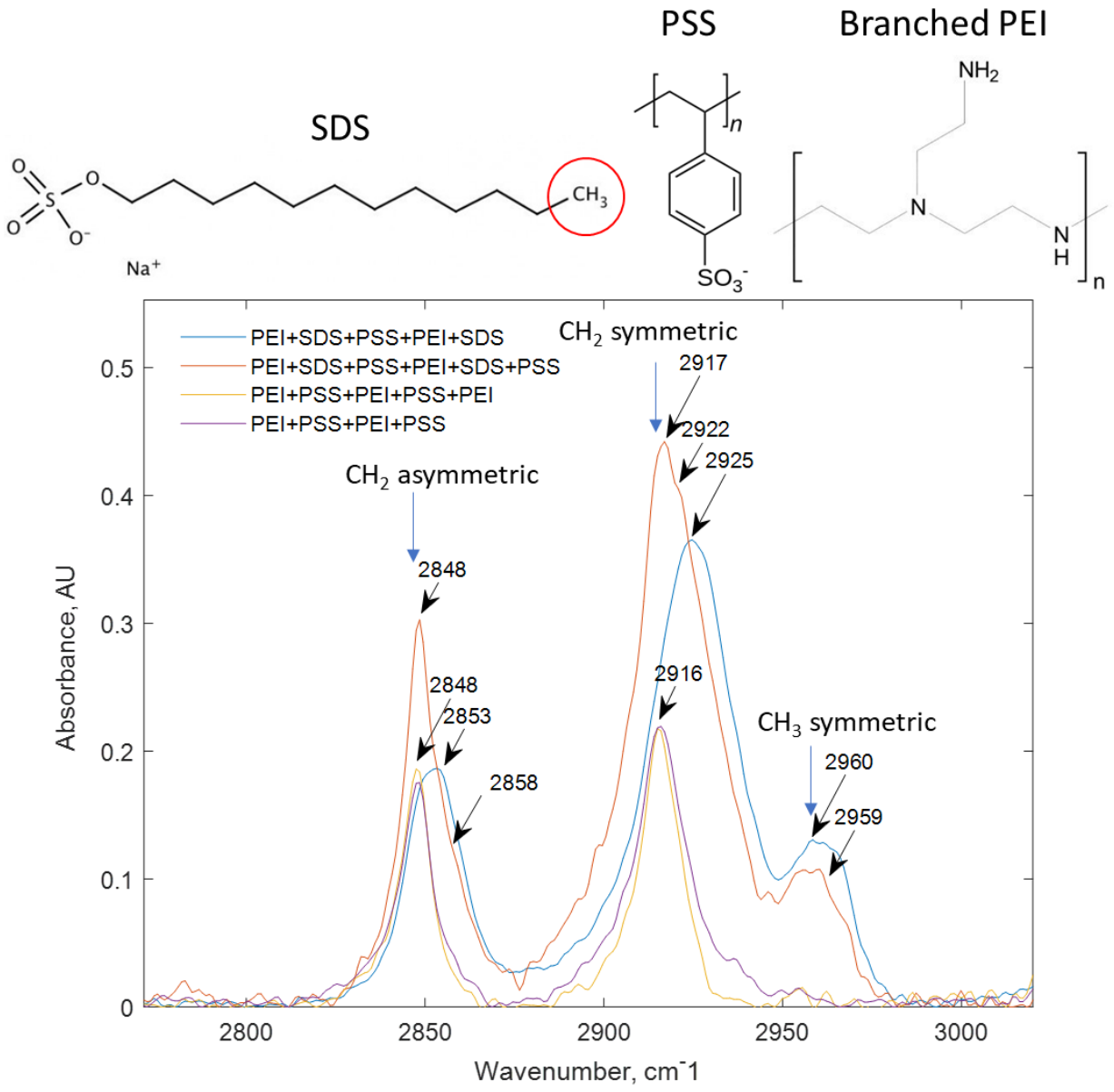

Figure A.3. PM-IRRAS spectra showing hydrocarbon stretching of polyelectrolyte/surfactant films.

Conclusions

Although the characteristic PEI peaks were not distinguishable in the obtained PM-IRRAS spectra, PEI must have been adsorbed on the negatively charged SAM and polyelectrolyte layers, as evidenced by

subsequent deposition of SDS and PSS. The spectra corroborate the retention of the SDS molecules adsorbed onto PEI, confirming that SDS is not displaced by rinsing and subsequent deposition of PSS.

Overall, the addition of SDS into the PEI/PSS films introduces regions of reduced crystallinity (therefore, a slight increase in the free volume within the films), which could contribute to the increased water permeation through PEI/SDS/PSS- vs. PEI/PSS-modified-PAN membranes[328].

References

(1) Freinkel, S. A Brief History of the Plastic's Conquest of the World. *Sci. Am.* **2011**, 1–9.

(2) Lewis Danny. Are We Living in the Plastic Age? | Smart News | Smithsonian https://www.smithsonianmag.com/smart-news/are-we-living-plastic-age-180957817/ (accessed Dec 28, 2020).

(3) Ball, P. Gourmet Macromolecules. *Nature*, 1995, *377*, 101–102.

(4) Wang, K.; Amin, K.; An, Z.; Cai, Z.; Chen, H.; Chen, H.; Dong, Y.; Feng, X.; Fu, W.; Gu, J.; *et al.* Advanced Functional Polymer Materials. *Materials Chemistry Frontiers*, 2020, *4*, 1803–1915.

(5) *IUPAC Compendium of Chemical Terminology*; Nič, M.; Jirát, J.; Košata, B.; Jenkins, A.; McNaught, A., Eds.; IUPAC: Research Triagle Park, NC, 2009.

(6) Ramanathan, K.; Bangar, M. A.; Yun, M.; Chen, W.; Myung, N. V.; Mulchandani, A. Bioaffinity Sensing Using Biologically Functionalized Conducting-Polymer Nanowire. *J. Am. Chem. Soc.* **2005**, *127*, 496–497.

(7) Garnier, F. Functionalized Conducting Polymers—Towards Intelligent Materials. *Angew. Chemie* **1989**, *101*, 529–533.

(8) Inzelt, G.; Pineri, M.; Schultze, J. W.; Vorotyntsev, M. A. Electron and Proton Conducting Polymers: Recent Developments and Prospects. *Electrochimica Acta*, 2000, *45*, 2403–2421.

(9) Wang, C.; Feng, Z.; Zhao, Y.; Li, X.; Li, W.; Xie, X.; Wang, S.; Hou, H. Preparation and Properties of Ion Exchange Membranes for PEMFC with Sulfonic and Carboxylic Acid Groups Based on Polynorbornenes. *Int. J. Hydrogen Energy* **2017**, *42*, 29988–29994.

(10) Darmanin, T.; Guittard, F. Wettability of Conducting Polymers: From Superhydrophilicity to

Superoleophobicity. *Prog. Polym. Sci.* **2014**, *39*, 656–682.

(11) Zheng, L.; Sundaram, H. S.; Wei, Z.; Li, C.; Yuan, Z. Applications of Zwitterionic Polymers. *Reactive and Functional Polymers*, 2017, *118*, 51–61.

(12) Imato, K.; Nishihara, M.; Kanehara, T.; Amamoto, Y.; Takahara, A.; Otsuka, H. Self-Healing of Chemical Gels Cross-Linked by Diarylbibenzofuranone-Based Trigger-Free Dynamic Covalent Bonds at Room Temperature. *Angew. Chemie* **2012**, *124*, 1164–1168.

(13) Williams, K. A.; Dreyer, D. R.; Bielawski, C. W. The Underlying Chemistry of Self-Healing Materials. *MRS Bull.* **2008**, *33*, 759–765.

(14) Groh, W.; Zimmermann, A. *What Is the Lowest Refractive Index of an Organic Polymer?*; 1991; Vol. 24.

(15) Illy, N.; Majonis, D.; Herrera, I.; Ornatsky, O.; Winnik, M. A. Metal-Chelating Polymers by Anionic Ring-Opening Polymerization and Their Use in Quantitative Mass Cytometry. *Biomacromolecules* **2012**, *13*, 2359–2369.

(16) Kantipuly, C.; Katragadda, S.; Chow, A.; Gesser, H. D. Chelating Polymers and Related Supports for Separation and Preconcentration of Trace Metals. *Talanta* **1990**, *37*, 491–517.

(17) Stuart, M. A. C.; Huck, W. T. S.; Genzer, J.; Müller, M.; Ober, C.; Stamm, M.; Sukhorukov, G. B.; Szleifer, I.; Tsukruk, V. V.; Urban, M.; *et al.* Emerging Applications of Stimuli-Responsive Polymer Materials. *Nat. Mater.* **2010**, *9*, 101–113.

(18) Wei, M.; Gao, Y.; Li, X.; Serpe, M. J. Stimuli-Responsive Polymers and Their Applications. *Polym. Chem.* **2017**, *8*, 127–143.

(19) Laloyaux, X.; Mathy, B.; Nysten, B.; Jonas, A. M. Surface and Bulk Collapse Transitions of

Thermoresponsive Polymer Brushes. *Langmuir* **2010**, *26*, 838–847.

(20) Zhao, Y.; Zhang, K. Thermoresponsive Polymers Based on Ring-Opening Metathesis Polymerization. *Polym. Chem.* **2016**, *7*, 4081–4089.

(21) Kumar, S.; Dory, Y. L.; Lepage, M.; Zhao, Y. Surface-Grafted Stimuli-Responsive Block Copolymer Brushes for the Thermo-, Photo- and PH-Sensitive Release of Dye Molecules. *Macromolecules* **2011**, *44*, 7385–7393.

(22) Bai, D.; Habersberger, B. M.; Jennings, G. K. PH-Responsive Copolymer Films by Surface-Catalyzed Growth. *J. Am. Chem. Soc.* **2005**, *127*, 16486–16493.

(23) Deng, X.; Livingston, J. L.; Spear, N. J.; Jennings, G. K. PH-Responsive Copolymer Films Prepared by Surface-Initiated Polymerization and Simple Modification. *Langmuir* **2020**, *36*, 715–722.

(24) Li, J. J.; Zhou, Y. N.; Luo, Z. H. Polymeric Materials with Switchable Superwettability for Controllable Oil/Water Separation: A Comprehensive Review. *Progress in Polymer Science*, 2018, *87*, 1–33.

(25) Fries, K.; Samanta, S.; Orski, S.; Locklin, J. Reversible Colorimetric Ion Sensors Based on Surface Initiated Polymerization of Photochromic Polymers. *Chem. Commun.* **2008**, 6288–6290.

(26) Pietschnig, R. Polymers with Pendant Ferrocenes. *Chemical Society Reviews*, 2016, *45*, 5216–5231.

(27) Stupp, S. I.; LeBonheur, V.; Walker, K.; Li, L. S.; Huggins, K. E.; Keser, M.; Amstutz, A. Supramolecular Materials: Self-Organized Nanostructures. *Science (80-.).* **1997**, *276*, 384–389.

(28) Whitesides, G. M.; Boncheva, M. Beyond Molecules: Self-Assembly of Mesoscopic and

Macroscopic Components. *Proc. Natl. Acad. Sci. U. S. A.* **2002**, *99*, 4769–4774.

(29) Schulz, D. N.; Patil, A. O. *Functional Polymers*; Patil, A. O.; Schulz, D. N.; Novak, B. M., Eds.; ACS Symposium Series; American Chemical Society: Washington, DC, 1998; Vol. 704.

(30) Tokarev, I.; Minko, S. Stimuli-Responsive Porous Hydrogels at Interfaces for Molecular Filtration, Separation, Controlled Release, and Gating in Capsules and Membranes. *Adv. Mater.* **2010**, *22*, 3446–3462.

(31) Ulbricht, M. Advanced Functional Polymer Membranes. *Polymer (Guildf).* **2006**, *47*, 2217–2262.

(32) Rolfe, A.; Loh, J. K.; Maity, P. K.; Hanson, P. R. High-Load, Hybrid Si-ROMP Reagents. *Org. Lett.* **2011**, *13*, 4–7.

(33) Deng, X.; Prozorovska, L.; Jennings, G. K. Metal Chelating Polymer Thin Films by Surface-Initiated ROMP and Modification. *J. Phys. Chem. C* **2019**, *123*, 23511–23519.

(34) Schüwer, N.; Klok, H.-A. A Potassium-Selective Quartz Crystal Microbalance Sensor Based on Crown-Ether Functionalized Polymer Brushes. *Adv. Mater.* **2010**, *22*, 3251–3255.

(35) Hu, J.; Liu, S. Responsive Polymers for Detection and Sensing Applications: Current Status and Future Developments. *Macromolecules* **2010**, *43*, 8315–8330.

(36) Kim, N. Y.; Jeon, N. L.; Choi, I. S.; Takami, S.; Harada, Y.; Finnie, K. R.; Girolami, G. S.; Nuzzo, R. G.; Whitesides, G. M.; Laibinis, P. E. Surface-Initiated Ring-Opening Metathesis Polymerization on Si/SiO 2. *Macromolecules* **2000**, *33*, 2793–2795.

(37) Horowitz, G. Organic Thin Film Transistors: From Theory to Real Devices. *J. Mater. Res.* **2004**, *19*, 1946–1962.

(38) Lin, P.; Yan, F. Organic Thin-Film Transistors for Chemical and Biological Sensing. *Adv. Mater.*

2012, *24*, 34–51.

(39) Dimitrakopoulos, C. D.; Malenfant, P. R. L. Organic Thin Film Transistors for Large Area Electronics. *Adv. Mater.* **2002**, *14*, 99–117.

(40) Krebs, F. C. Fabrication and Processing of Polymer Solar Cells: A Review of Printing and Coating Techniques. *Solar Energy Materials and Solar Cells*, 2009, *93*, 394–412.

(41) Braga, D.; Horowitz, G. High-Performance Organic Field-Effect Transistors. *Adv. Mater.* **2009**, *21*, 1473–1486.

(42) Tian, F.; Decker, E. A.; Goddard, J. M. Control of Lipid Oxidation by Nonmigratory Active Packaging Films Prepared by Photoinitiated Graft Polymerization. *J. Agric. Food Chem.* **2012**, *60*, 7710–7718.

(43) Faulkner, C. J.; Fischer, R. E.; Jennings, G. K. Surface-Initiated Polymerization of 5-(Perfluoro- n -Alkyl)Norbornenes from Gold Substrates. *Macromolecules* **2010**, *43*, 1203–1209.

(44) Berron, B. J.; Graybill, E. P.; Jennings, G. K. Growth and Structure of Surface-Initiated Poly(n -Alkylnorbornene) Films. *Langmuir* **2007**, *23*, 11651–11655.

(45) Wang, Y.; Huang, X.; Li, T.; Li, L.; Guo, X.; Jiang, P. Polymer-Based Gate Dielectrics for Organic Field-Effect Transistors. *Chem. Mater.* **2019**, *31*, 2212–2240.

(46) Ho, J. S.; Greenbaum, S. G. Polymer Capacitor Dielectrics for High Temperature Applications. *ACS Applied Materials and Interfaces*, 2018, *10*, 29189–29218.

(47) Song, J.; Winkeljann, B.; Lieleg, O. Biopolymer-Based Coatings: Promising Strategies to Improve the Biocompatibility and Functionality of Materials Used in Biomedical Engineering. *Adv. Mater. Interfaces* **2020**, *7*, 2000850.

(48) Wei, Q.; Becherer, T.; Angioletti-Uberti, S.; Dzubiella, J.; Wischke, C.; Neffe, A. T.; Lendlein, A.; Ballauff, M.; Haag, R. Protein Interactions with Polymer Coatings and Biomaterials. *Angew. Chemie - Int. Ed.* **2014**, *53*, 8004–8031.

(49) Raviv, U.; Giasson, S.; Kampf, N.; Gohy, J. F.; Jéröme, R.; Klein, J. Lubrication by Charged Polymers. *Nature* **2003**, *425*, 163–165.

(50) Seehof, N.; Risse, W. Ring-opening Olefin Metathesis Polymerization of Fluoroalkyl-substituted Polycyclic Olefins. *Die Makromol. Chemie. Rapid Commun.* **1991**, *12*, 107–112.

(51) Scriven, L. E. Physics and Applications of DIP Coating and Spin Coating. *MRS Proc.* **1988**, *121*, 717.

(52) Reneker, D. H.; Chun, I. Nanometre Diameter Fibres of Polymer, Produced by Electrospinning. *Nanotechnology* **1996**, *7*, 216–223.

(53) Baji, A.; Mai, Y. W.; Wong, S. C.; Abtahi, M.; Chen, P. Electrospinning of Polymer Nanofibers: Effects on Oriented Morphology, Structures and Tensile Properties. *Composites Science and Technology*, 2010, *70*, 703–718.

(54) Menard, E.; Bilhaut, L.; Zaumseil, J.; Rogers, J. A. Improved Surface Chemistries, Thin Film Deposition Techniques, and Stamp Designs for Nanotransfer Printing. *Langmuir* **2004**, *20*, 6871–6878.

(55) de Gans, B.-J.; Duineveld, P. C.; Schubert, U. S. Inkjet Printing of Polymers: State of the Art and Future Developments. *Adv. Mater.* **2004**, *16*, 203–213.

(56) Kim, E.; Xia, Y.; Whitesides, G. M. Micromolding in Capillaries: Applications in Materials Science. *J. Am. Chem. Soc.* **1996**, *118*, 5722–5731.

(57) Escobar, C. A.; Cooksey, T. J.; Spellings, M. P.; Jennings, G. K. Micromolding Surface-Initiated Polymerization: A Versatile Route for Fabrication of Coatings with Microscale Surface Features of Tunable Height. *Adv. Mater. Interfaces* **2014**, *1*, 1400055.

(58) Escobar, C. A.; Spellings, M. P.; Cooksey, T. J.; Jennings, G. K. Reproducing Superhydrophobic Leaves as Coatings by Micromolding Surface-Initiated Polymerization. *Macromol. Rapid Commun.* **2014**, *35*, 1937–1942.

(59) Hall, D. B.; Underhill, P.; Torkelson, J. M. Spin Coating of Thin and Ultrathin Polymer Films. *Polym. Eng. Sci.* **1998**, *38*, 2039–2045.

(60) Norrman, K.; Ghanbari-Siahkali, A.; Larsen, N. B. Studies of Spin-Coated Polymer Films. *Annual Reports on the Progress of Chemistry - Section C*, 2005, *101*, 174–201.

(61) Ariga, K.; Yamauchi, Y.; Mori, T.; Hill, J. P. 25th Anniversary Article: What Can Be Done with the Langmuir-Blodgett Method? Recent Developments and Its Critical Role in Materials Science. *Advanced Materials*, 2013, *25*, 6477–6512.

(62) Kharlampieva, E.; Kozlovskaya, V.; Sukhishvili, S. A. Layer-by-Layer Hydrogen-Bonded Polymer Films: From Fundamentals to Applications. *Adv. Mater.* **2009**, *21*, 3053–3065.

(63) Richardson, J. J.; Cui, J.; Björnmalm, M.; Braunger, J. A.; Ejima, H.; Caruso, F. Innovation in Layer-by-Layer Assembly. *Chemical Reviews*, 2016, *116*, 14828–14867.

(64) Zdyrko, B.; Luzinov, I. Polymer Brushes by the "Grafting to" Method. *Macromol. Rapid Commun.* **2011**, *32*, 859–869.

(65) Edmondson, S.; Osborne, V. L.; Huck, W. T. S. Polymer Brushes via Surface-Initiated Polymerizations. *Chem. Soc. Rev.* **2004**, *33*, 14–22.

(66) Deegan, R. D.; Bakajin, O.; Dupont, T. F.; Huber, G.; Nagel, S. R.; Witten, T. A. Capillary Flow as the Cause of Ring Stains from Dried Liquid Drops. *Nature* **1997**, *389*, 827–829.

(67) Brinker, C. J. Dip Coating. In *Chemical Solution Deposition of Functional Oxide Thin Films*; Springer Vienna: Vienna, 2013; pp. 233–261.

(68) Mouhamad, Y.; Mokarian-Tabari, P.; Clarke, N.; Jones, R. A. L.; Geoghegan, M. Dynamics of Polymer Film Formation during Spin Coating. *J. Appl. Phys.* **2014**, *116*, 123513.

(69) Lawrence, C. J. The Mechanics of Spin Coating of Polymer Films. *Phys. Fluids* **1988**, *31*, 2786.

(70) Balzarotti, R.; Cristiani, C.; Francis, L. F. Spin Coating Deposition on Complex Geometry Substrates: Influence of Operative Parameters. *Surf. Coatings Technol.* **2017**, *330*, 1–9.

(71) Li, Z.; Tolan, M.; Höhr, T.; Kharas, D.; Qu, S.; Sokolov, J.; Rafailovich, M. H.; Lorenz, H.; Kotthaus, J. P.; Wang, J.; *et al.* Polymer Thin Films on Patterned Si Surfaces. *Macromolecules* **1998**, *31*, 1915–1920.

(72) Yoon, B.; Acharya, H.; Lee, G.; Kim, H.-C.; Huh, J.; Park, C. Nanopatterning of Thin Polymer Films by Controlled Dewetting on a Topographic Pre-Pattern. *Soft Matter* **2008**, *4*, 1467.

(73) Roy, S.; Ansari, K. J.; Jampa, S. S. K.; Vutukuri, P.; Mukherjee, R. Influence of Substrate Wettability on the Morphology of Thin Polymer Films Spin-Coated on Topographically Patterned Substrates. *ACS Appl. Mater. Interfaces* **2012**, *4*, 1887–1896.

(74) Birnie, D. P. Spin Coating: Art and Science. In *Chemical Solution Deposition of Functional Oxide Thin Films*; Springer-Verlag Wien, 2013; Vol. 9783211993, pp. 263–274.

(75) Das, R.; Chanda, A. Fabrication and Properties of Spin-Coated Polymer Films. In *Nano-Size Polymers: Preparation, Properties, Applications*; Springer International Publishing, 2016; pp.

283–306.

(76) Toolan, D. T. W.; Howse, J. R. Development of in Situ Studies of Spin Coated Polymer Films. *J. Mater. Chem. C* **2013**, *1*, 603–616.

(77) Hall, D. B.; Underhill, P.; Torkelson, J. M. Spin Coating of Thin and Ultrathin Polymer Films. *Polym. Eng. Sci.* **1998**, *38*, 2039–2045.

(78) Emslie, A. G.; Bonner, F. T.; Peck, L. G. Flow of a Viscous Liquid on a Rotating Disk. *J. Appl. Phys.* **1958**, *29*, 858–862.

(79) Meyerhofer, D. Characteristics of Resist Films Produced by Spinning. *J. Appl. Phys.* **1978**, *49*, 3993–3997.

(80) Bornside, D. E.; Macosko, C. W.; Scriven, L. E. Spin Coating: One-Dimensional Model. *J. Appl. Phys.* **1989**, *66*, 5185–5193.

(81) Karpitschka, S.; Weber, C. M.; Riegler, H. Spin Casting of Dilute Solutions: Vertical Composition Profile during Hydrodynamic-Evaporative Film Thinning. *Chem. Eng. Sci.* **2015**, *129*, 243–248.

(82) Lehn, J.-M. Supramolecular Chemistry—Scope and Perspectives Molecules, Supermolecules, and Molecular Devices(Nobel Lecture). *Angew. Chemie Int. Ed. English* **1988**, *27*, 89–112.

(83) Seto, C. T.; Whitesides, G. M. Molecular Self-Assembly through Hydrogen Bonding: Supramolecular Aggregates Based on the Cyanuric Acid·Melamine Lattice. *J. Am. Chem. Soc.* **1993**, *115*, 905–916.

(84) Stupp, S. I.; Palmer, L. C. Supramolecular Chemistry and Self-Assembly in Organic Materials Design. *Chemistry of Materials*, 2014, *26*, 507–518.

(85) Love, J. C.; Estroff, L. A.; Kriebel, J. K.; Nuzzo, R. G.; Whitesides, G. M. Self-Assembled Monolayers of Thiolates on Metals as a Form of Nanotechnology. *Chem. Rev.* **2005**, *105*, 1103–1170.

(86) Ulman, A. Formation and Structure of Self-Assembled Monolayers. *Chem. Rev.* **1996**, *96*, 1533–1554.

(87) Onclin, S.; Ravoo, B. J.; Reinhoudt, D. N. Engineering Silicon Oxide Surfaces Using Self-Assembled Monolayers. *Angew. Chemie - Int. Ed.* **2005**, *44*, 6282–6304.

(88) Mahajan, S. Thiol-Based Self-Assembled Monolayers: Formation and Organization. **2001**, *Encycloped*, 9332–9344.

(89) Nuzzo, R. G.; Allara, D. L. Adsorption of Bifunctional Organic Disulfides on Gold Surfaces. *J. Am. Chem. Soc.* **1983**, *105*, 4481–4483.

(90) Hatchett, D. W.; Uibel, R. H.; Stevenson, K. J.; Harris, J. M.; White, H. S. Electrochemical Measurement of the Free Energy of Adsorption of N-Alkanethiolates at Ag(111). *J. Am. Chem. Soc.* **1998**, *120*, 1062–1069.

(91) Jennings, G. K.; Laibinis, P. E. Self-Assembled n -Alkanethiolate Monolayers on Underpotentially Deposited Adlayers of Silver and Copper on Gold. *J. Am. Chem. Soc.* **1997**, *119*, 5208–5214.

(92) Jennings, G. K.; Laibinis, P. E. Self-Assembled Monolayers of Alkanethiols on Copper Provide Corrosion Resistance in Aqueous Environments. *Colloids Surfaces A Physicochem. Eng. Asp.* **1996**, *116*, 105–114.

(93) Sheen, C. W.; Shi, J.; Martensson, J.; Parikh, A. N.; Allara, D. L.; Carcanague, D. R.; Knobler, C.

B. A New Class of Organized Self-Assembled Monolayers : Alkane Thiols on GaAs (100) Department of Chemistry Water-Soluble Cyclophane Receptors with Convergent Functional Groups University of California at Los Angeles. **1992**, 1514–1515.

(94) Fendler, J. H. Chemical Self-Assembly for Electronic Applications. *Chemistry of Materials*, 2001, *13*, 3196–3210.

(95) Richardson, J. J.; Bjornmalm, M.; Caruso, F. Technology-Driven Layer-by-Layer Assembly of Nanofilms. *Science (80-.).* **2015**, *348*, aaa2491–aaa2491.

(96) Decher, G. Fuzzy Nanoassemblies: Toward Layered Polymeric Multicomposites. *Science (80-.).* **1997**, *277*, 1232–1237.

(97) Cassier, T.; Lowack, K.; Decher, G. Layer-by-Layer Assembled Protein/Polymer Hybrid Films: Nanoconstruction via Specific Recognition. *Supramol. Sci.* **1998**, *5*, 309–315.

(98) Borges, J.; Mano, J. F. Molecular Interactions Driving the Layer-by-Layer Assembly of Multilayers. *Chem. Rev.* **2014**, *114*, 8883–8942.

(99) Jiang, C.; Tsukruk, V. V. Freestanding Nanostructures via Layer-by-Layer Assembly. *Adv. Mater.* **2006**, *18*, 829–840.

(100) Murugan, P.; Krishnamurthy, M.; Jaisankar, S. N.; Samanta, D.; Mandal, A. B. Controlled Decoration of the Surface with Macromolecules: Polymerization on a Self-Assembled Monolayer (SAM). *Chem. Soc. Rev.* **2015**, *44*, 3212–3243.

(101) Zoppe, J. O.; Ataman, N. C.; Mocny, P.; Wang, J.; Moraes, J.; Klok, H.-A. Surface-Initiated Controlled Radical Polymerization: State-of-the-Art, Opportunities, and Challenges in Surface and Interface Engineering with Polymer Brushes. *Chem. Rev.* **2017**, *117*, 1105–1318.

(102) Zhao, B.; Brittain, W. . Polymer Brushes: Surface-Immobilized Macromolecules. *Prog. Polym. Sci.* **2000**, *25*, 677–710.

(103) Jennings, G. K.; Brantley, E. L. Physicochemical Properties of Surface-Initiated Polymer Films in the Modification and Processing of Materials. *Adv. Mater.* **2004**, *16*, 1983–1994.

(104) Matyjaszewski, K.; Dong, H.; Jakubowski, W.; Pietrasik, J.; Kusumo, A. Grafting from Surfaces for "Everyone": ARGET ATRP in the Presence of Air. *Langmuir* **2007**, *23*, 4528–4531.

(105) Brantley, E. L.; Holmes, T. C.; Jennings, G. K. Modification of ATRP Surface-Initiated Poly(Hydroxyethyl Methacrylate) Films with Hydrocarbon Side Chains. *J. Phys. Chem. B* **2004**, *108*, 16077–16084.

(106) Brantley, E. L.; Jennings, G. K. Fluorinated Polymer Films from Acylation of ATRP Surface-Initiated Poly(Hydroxyethyl Methacrylate). *Macromolecules* **2004**, *37*, 1476–1483.

(107) Kong, B.; Lee, J. K.; Choi, I. S. Surface-Initiated, Ring-Opening Metathesis Polymerization: Formation of Diblock Copolymer Brushes and Solvent-Dependent Morphological Changes. *Langmuir* **2007**, *23*, 6761–6765.

(108) Colombani, D. Chain-Growth Control in Free Radical Polymerization. *Prog. Polym. Sci.* **1997**, *22*, 1649–1720.

(109) Stille, J. K. Step-Growth Polymerization. *J. Chem. Educ.* **1981**, *58*, 862–866.

(110) Charles, E.; Carraher, J. *Seymour/Carraher's Polymer Chemistry: Sixth Edition - Charles E. Carraher Jr.*

(111) Brydson, J. A. Epoxide Resins. In *Plastics Materials*; Elsevier, 1999; pp. 744–777.

(112) Matyjaszewski, K. *Cationic Polymerizations: Mechanisms, Synthesis & Applications - 1st E*;

1996.

(113) Matyjaszewski, K. Macromolecular Engineering: From Rational Design through Precise Macromolecular Synthesis and Processing to Targeted Macroscopic Material Properties. *Prog. Polym. Sci.* **2005**, *30*, 858–875.

(114) Hsieh, H.; Quirk, R. P. *Anionic Polymerization: Principles and Practical Applications - Henry Hsieh, Roderic P. Quirk - Google Books*; 1996.

(115) Galli, P.; Luciani, L.; Cecchin, G. Advances in the Polymerization of Polyolefins with Coordination Catalysts. *Die Angew. Makromol. Chemie* **1981**, *94*, 63–89.

(116) Fried, J. R. *Polymer Science and Technology*; Pearson, 2003.

(117) Breslow, D. S. Metathesis Polymerization. *Prog. Polym. Sci.* **1993**, *18*, 1141–1195.

(118) Ivin, K. J.; Mol, J. C. *Olefin Metathesis and Metathesis Polymerization*; 1997.

(119) Vougioukalakis, G. C.; Grubbs, R. H. Ruthenium-Based Heterocyclic Carbene-Coordinated Olefin Metathesis Catalysts. *Chem. Rev.* **2010**, *110*, 1746–1787.

(120) Bielawski, C. W.; Grubbs, R. H. Living Ring-Opening Metathesis Polymerization. *Prog. Polym. Sci.* **2007**, *32*, 1–29.

(121) Choi, T. L.; Grubbs, R. H. Controlled Living Ring-Opening-Metathesis Polymerization by a Fast-Initiating Ruthenium Catalyst. *Angew. Chemie - Int. Ed.* **2003**, *42*, 1743–1746.

(122) Slugovc, C. The Ring Opening Metathesis Polymerisation Toolbox. *Macromol. Rapid Commun.* **2004**, *25*, 1283–1297.

(123) Trnka, T. M.; Grubbs, R. H. The Development of L 2 X 2 RuCHR Olefin Metathesis Catalysts:

An Organometallic Success Story. *Acc. Chem. Res.* **2001**, *34*, 18–29.

(124) Grubbs, R. H. *Handbook of Metathesis, Volume I: Catalyst Development and Mechanism*; 2004; Vol. 1.

(125) Jean-Louis Hérisson, P.; Chauvin, Y. Catalyse de Transformation Des Oléfines Par Les Complexes Du Tungstène. II. Télomérisation Des Oléfines Cycliques En Présence d'oléfines Acycliques. *Die Makromol. Chemie* **1971**, *141*, 161–176.

(126) Buchmeiser, M. R.; Sinner, F.; Mupa, M.; Wurst, K. Ring-Opening Metathesis Polymerization for the Preparation of Surface-Grafted Polymer Supports. *Macromolecules* **2000**, *33*, 32–39.

(127) Faulkner, C. J.; Fischer, R. E.; Jennings, G. K. Surface-Initiated Polymerization of 5-(Perfluoro- n -Alkyl)Norbornenes from Gold Substrates. *Macromolecules* **2010**, *43*, 1203–1209.

(128) Nesvadba, P. Radical Polymerization in Industry. In *Encyclopedia of Radicals in Chemistry, Biology and Materials*; John Wiley & Sons, Ltd: Chichester, UK, 2012.

(129) Braunecker, W. A.; Matyjaszewski, K. Controlled/Living Radical Polymerization: Features, Developments, and Perspectives. *Prog. Polym. Sci.* **2007**, *32*, 93–146.

(130) Zetterlund, P. B.; Kagawa, Y.; Okubo, M. Controlled/Living Radical Polymerization in Dispersed Systems. *Chem. Rev.* **2008**, *108*, 3747–3794.

(131) Hawker, C. J.; Bosman, A. W.; Harth, E. New Polymer Synthesis by Nitroxide Mediated Living Radical Polymerizations. *Chem. Rev.* **2001**, *101*, 3661–3688.

(132) Matyjaszewski, K.; Xia, J. Atom Transfer Radical Polymerization. *Chem. Rev.* **2001**, *101*, 2921–2990.

(133) Moad, G.; Rizzardo, E.; Thang, S. H. Living Radical Polymerization by the RAFT Process. *Aust.*

J. Chem. **2005**, *58*, 379.

(134) Matyjaszewski, K. Atom Transfer Radical Polymerization (ATRP): Current Status and Future Perspectives. *Macromolecules* **2012**, *45*, 4015–4039.

(135) Min, K.; Gao, H.; Matyjaszewski, K. Preparation of Homopolymers and Block Copolymers in Miniemulsion by ATRP Using Activators Generated by Electron Transfer (AGET). *J. Am. Chem. Soc.* **2005**, *127*, 3825–3830.

(136) Min, K.; Gao, H.; Matyjaszewski, K. Use of Ascorbic Acid as Reducing Agent for Synthesis of Well-Defined Polymers by ARGET ATRP. *Macromolecules* **2007**, *40*, 1789–1791.

(137) Matyjaszewski, K.; Jakubowski, W.; Min, K.; Tang, W.; Huang, J.; Braunecker, W. A.; Tsarevsky, N. V. Diminishing Catalyst Concentration in Atom Transfer Radical Polymerization with Reducing Agents. *Proc. Natl. Acad. Sci. U. S. A.* **2006**, *103*, 15309–15314.

(138) Gao, H.; Chan, N.; Oh, J. K.; Matyjaszewski, K. Designing Hydrogels by ATRP. In; Springer, Singapore, 2015; pp. 69–105.

(139) Gauthier, M. A.; Gibson, M. I.; Klok, H.-A. Synthesis of Functional Polymers by Post-Polymerization Modification. *Angew. Chemie Int. Ed.* **2009**, *48*, 48–58.

(140) Galvin, C. J.; Genzer, J. Applications of Surface-Grafted Macromolecules Derived from Post-Polymerization Modification Reactions. *Prog. Polym. Sci.* **2012**, *37*, 871–906.

(141) Muzammil, E. M.; Khan, A.; Stuparu, M. C. Post-Polymerization Modification Reactions of Poly(Glycidyl Methacrylate)S. *RSC Adv.* **2017**, *7*, 55874–55884.

(142) Moore, J. D.; Byrne, R. J.; Vedantham, P.; Flynn, D. L.; Hanson, P. R. High-Load, ROMP-Generated Oligomeric Bis-Acid Chlorides: Design of Soluble and Insoluble Nucleophile

Scavengers. *Org. Lett.* **2003**, *5*, 4241–4244.

(143) *IUPAC Compendium of Chemical Terminology*; IUPAC, 2009.

(144) Hider, R. C.; Ma, Y. CHAPTER 2. Basic Principles of Metal Chelation and Chelator Design. In *Metal Chelation in Medicine*; The Royal Society of Chemistry, 2016; Vol. 13, pp. 24–55.

(145) Martell, A. E.; Hancock, R. D. *Metal Complexes in Aqueous Solutions*; Springer US: Boston, MA, 1996.

(146) Pearson, R. G. Hard and Soft Acids and Bases. *J. Am. Chem. Soc.* **1963**, *85*, 3533–3539.

(147) Pearson, R. G. Hard and Soft Acids and Bases, HSAB, Part 1: Fundamental Principles. *J. Chem. Educ.* **1968**, *45*, 581.

(148) Pearson, R. G. Hard and Soft Acids and Bases, HSAB, Part II: Underlying Theories. *J. Chem. Educ.* **1968**, *45*, 643.

(149) Hancock, R. D.; Martell, A. E. Ligand Design for Selective Complexation of Metal Ions in Aqueous Solution. *Chem. Rev.* **1989**, *89*, 1875–1914.

(150) Schweigert, N.; Zehnder, A. J. B.; Eggen, R. I. L. Chemical Properties of Catechols and Their Molecular Modes of Toxic Action in Cells, from Microorganisms to Mammals. Minireview. *Environ. Microbiol.* **2001**, *3*, 81–91.

(151) Martell, A. E.; Smith, R. M. Phenols. In *Critical Stability Constants*; Springer US: Boston, MA, 1982; pp. 336–356.

(152) Raymond, K. N.; McMurry, T. J.; Garrett, T. M. Macrocyclic Catechol-Containing Ligands. *Pure Appl. Chem.* **1988**, *60*, 545–548.

(153) Howlin, B.; Mohd-Nor, A. R.; Silver, J.; Barnard, P. W. C. Model Compounds for Microbial Iron-Transport Compounds. Part V. Substituent Effects in the Catechol/FeCl3 System. *Inorganica Chim. Acta* **1984**, *91*, 153–160.

(154) Hider, R. C.; Liu, Z. D.; Khodr, H. H. Metal Chelation of Polyphenols. In; 2001; Vol. 6879, pp. 190–203.

(155) Hider, R. C.; Howlin, B.; Miller, J. R.; Mohd-Nor, A. R.; Silver, J. Model Compounds for Microbial Iron-Transport Compounds. Part IV. Further Solution Chemistry and Mössbauer Studies on Iron(II) and Iron(III) Catechol Complexes. *Inorganica Chim. Acta* **1983**, *80*, 51–56.

(156) Avdeef, A.; Sofen, S. R.; Bregante, T. L.; Raymond, K. N. Coordination Chemistry of Microbial Iron Transport Compounds. 9. Stability Constants for Catechol Models of Enterobactin. *J. Am. Chem. Soc.* **1978**, *100*, 5362–5370.

(157) Andersen, A.; Chen, Y.; Birkedal, H. Bioinspired Metal–Polyphenol Materials: Self-Healing and Beyond. *Biomimetics* **2019**, *4*, 30.

(158) Patil, N.; Jérôme, C.; Detrembleur, C. Recent Advances in the Synthesis of Catechol-Derived (Bio)Polymers for Applications in Energy Storage and Environment. *Prog. Polym. Sci.* **2018**, *82*, 34–91.

(159) Faure, E.; Falentin-Daudré, C.; Jérôme, C.; Lyskawa, J.; Fournier, D.; Woisel, P.; Detrembleur, C. Catechols as Versatile Platforms in Polymer Chemistry. *Prog. Polym. Sci.* **2013**, *38*, 236–270.

(160) Sedõ, J.; Saiz-Poseu, J.; Busqué, F.; Ruiz-Molina, D. Catechol-Based Biomimetic Functional Materials. *Adv. Mater.* **2013**, *25*, 653–701.

(161) Guin, P. S.; Das, S.; Mandal, P. C. Electrochemical Reduction of Quinones in Different Media: A

Review. *Int. J. Electrochem.* **2011**, *2011*, 1–22.

(162) Yang, J.; Cohen Stuart, M. A.; Kamperman, M. Jack of All Trades: Versatile Catechol Crosslinking Mechanisms. *Chem. Soc. Rev.* **2014**, *43*, 8271–8298.

(163) Kurzak, B.; Kozłowski, H.; Farkas, E. Hydroxamic and Aminohydroxamic Acids and Their Complexes with Metal Ions. *Coord. Chem. Rev.* **1992**, *114*, 169–200.

(164) Keth, J.; Johann, T.; Frey, H. Hydroxamic Acid: An Underrated Moiety? Marrying Bioinorganic Chemistry and Polymer Science. *Biomacromolecules* **2020**, *21*, 2546–2556.

(165) Johann, T.; Keth, J.; Bros, M.; Frey, H. A General Concept for the Introduction of Hydroxamic Acids into Polymers. *Chem. Sci.* **2019**, *10*, 7009–7022.

(166) Roman, M. J.; Decker, E. A.; Goddard, J. M. Fourier Transform Infrared Studies on the Dissociation Behavior of Metal-Chelating Polyelectrolyte Brushes. *ACS Appl. Mater. Interfaces* **2014**, *6*, 5383–5387.

(167) Love, J. A.; Morgan, J. P.; Trnka, T. M.; Grubbs, R. H. A Practical and Highly Active Ruthenium-Based Catalyst That Effects the Cross Metathesis of Acrylonitrile. *Angew. Chemie Int. Ed.* **2002**, *41*, 4035–4037.

(168) Perez, E.; Laval, J. P.; Bon, M.; Rico, I.; Lattes, A. Synthesis of Bicyclo [2· 2· 1] Hept-2-Enes with Mono and Disubstituted Long Perfluorinated Chains CnF2n+1 (n = 4,6,8,10) Investigation of Association in Solution by 19F NMR Study of Polymerization via a Metathetic Reaction. *J. Fluor. Chem.* **1988**, *39*, 173–196.

(169) Greber, G. Vogel's Textbook of Practical Organic Chemistry (5th Ed.), Revised by Brian S. Furniss, Antony J. Hannaford, Peter W. G. Smith, and Austin R. Tatchell, John Wiley & Sons,

New York, 1514 Pp. Price: $84.95. *J. Polym. Sci. Part A Polym. Chem.* **1991**, *29*, 1223–1223.

(170) Blum, M. M.; John, H. Historical Perspective and Modern Applications of Attenuated Total Reflectance - Fourier Transform Infrared Spectroscopy (ATR-FTIR). *Drug Test. Anal.* **2012**, *4*, 298–302.

(171) Smith, B. C. *Fundamentals of Fourier Transform Infrared Spectroscopy, Second Edition*; CRC Press, 2011.

(172) Fahrenfort, J. Attenuated Total Reflection. *Spectrochim. Acta* **1961**, *17*, 698–709.

(173) Milosevic, M. *Internal Reflection and ATR Spectroscopy*; John Wiley & Sons, Inc.: Hoboken, NJ, USA, 2012.

(174) Harrick, N. J. Surface Chemistry from Spectral Analysis of Totally Internally Reflected Radiation. *J. Phys. Chem.* **1960**, *64*, 1110–1114.

(175) Huhtamäki, T.; Tian, X.; Korhonen, J. T.; Ras, R. H. A. Surface-Wetting Characterization Using Contact-Angle Measurements. *Nat. Protoc.* **2018**, *13*, 1521–1538.

(176) Marmur, A. Thermodynamic Aspects of Contact Angle Hysteresis. *Adv. Colloid Interface Sci.* **1994**, *50*, 121–141.

(177) Tosa, M. Surface Profilometer. In *Compendium of Surface and Interface Analysis*; Springer Singapore, 2018; pp. 679–682.

(178) Fujiwara, H. *Spectroscopic Ellipsometry: Principles and Applications*; John Wiley & Sons, 2007.

(179) Woollam, J. A. Ellipsometry Measurements - J.A. Woollam https://www.jawoollam.com/resources/ellipsometry-tutorial/ellipsometry-measurements (accessed Mar 24, 2020).

(180) Lvovich, V. F. *Impedance Spectroscopy: Applications to Electrochemical and Dielectric Phenomena*; John Wiley and Sons, 2012.

(181) Bott, A. W.; Ph, D. Electrochemical Techniques for the Characterization of Redox Polymers. *Curr. Sep.* **2001**, *19*, 71–75.

(182) Nano science Instruments. Quartz Crystal Microbalance (QCM) - Nanoscience Instruments https://www.nanoscience.com/techniques/quartz-crystal-microbalance/ (accessed Oct 11, 2019).

(183) Reviakine, I.; Johannsmann, D.; Richter, R. P. Hearing What You Cannot See and Visualizing What You Hear: Interpreting Quartz Crystal Microbalance Data from Solvated Interfaces. *Anal. Chem.* **2011**, *83*, 8838–8848.

(184) Sauerbrey, G. Verwendung von Schwingquarzen Zur Wägung Dünner Schichten Und Zur Mikrowägung. *Zeitschrift für Phys.* **1959**, *155*, 206–222.

(185) Sartore, L.; Barbaglio, M.; Borgese, L.; Bontempi, E. Polymer-Grafted QCM Chemical Sensor and Application to Heavy Metal Ions Real Time Detection. *Sensors Actuators, B Chem.* **2011**, *155*, 538–544.

(186) Voinova, M. V; Rodahl, M.; Jonson, M.; Kasemo, B. Viscoelastic Acoustic Response of Layered Polymer Films at Fluid-Solid Interfaces: Continuum Mechanics Approach. *Phys. Scr.* **1999**, *59*, 391–396.

(187) Gill, P.; Moghadam, T. T.; Ranjbar, B. Differential Scanning Calorimetry Techniques: Applications in Biology and Nanoscience. *Journal of Biomolecular Techniques*, 2010, *21*, 167–193.

(188) Fava, R. A. Differential Scanning Calorimetry of Epoxy Resins. *Polymer (Guildf).* **1968**, *9*, 137–

151.

(189) Hardis, R.; Jessop, J. L. P.; Peters, F. E.; Kessler, M. R. Cure Kinetics Characterization and Monitoring of an Epoxy Resin Using DSC, Raman Spectroscopy, and DEA. *Compos. Part A Appl. Sci. Manuf.* **2013**, *49*, 100–108.

(190) Coats, A. W.; Redfern, J. P. Thermogravimetric Analysis. A Review. *Analyst* **1963**, *88*, 906.

(191) Brandon, D.; Kaplan, W. D. *Microstructural Characterization of Materials: 2nd Edition*; John Wiley and Sons: Chichester, UK, 2008.

(192) Goldstein, J. I.; Newbury, D. E.; Michael, J. R.; Ritchie, N. W. M.; Scott, J. H. J.; Joy, D. C. *Scanning Electron Microscopy and X-Ray Microanalysis*; Springer New York, 2017.

(193) Björklund, A.; Dunnett, S. B. Dopamine Neuron Systems in the Brain: An Update. *Trends Neurosci.* **2007**, *30*, 194–202.

(194) Perron, N. R.; Brumaghim, J. L. A Review of the Antioxidant Mechanisms of Polyphenol Compounds Related to Iron Binding. *Cell Biochem. Biophys.* **2009**, *53*, 75–100.

(195) Lee, H.; Lee, B. P.; Messersmith, P. B. A Reversible Wet/Dry Adhesive Inspired by Mussels and Geckos. *Nature* **2007**, *448*, 338–341.

(196) Lee, B. P.; Messersmith, P. B.; Israelachvili, J. N.; Waite, J. H. Mussel-Inspired Adhesives and Coatings. *Annu. Rev. Mater. Res.* **2011**, *41*, 99–132.

(197) Yamada, K.; Chen, T.; Kumar, G.; Vesnovsky, O.; Timmie Topoleski, L. D.; Payne, G. F. Chitosan Based Water-Resistant Adhesive. Analogy to Mussel Glue. *Biomacromolecules* **2000**, *1*, 252–258.

(198) Hider, R. C. Siderophore Mediated Absorption of Iron. *Siderophores from Microorg. Plants*

2007, 25–87.

(199) Lee, B. P.; Konst, S. Novel Hydrogel Actuator Inspired by Reversible Mussel Adhesive Protein Chemistry. *Adv. Mater.* **2014**, *26*, 3415–3419.

(200) Kim, E.; Liu, Z.; Liu, Y.; Bentley, W.; Payne, G. Catechol-Based Hydrogel for Chemical Information Processing. *Biomimetics* **2017**, *2*, 11.

(201) Gao, Z.; Duan, L.; Yang, Y.; Hu, W.; Gao, G. Mussel-Inspired Tough Hydrogels with Self-Repairing and Tissue Adhesion. *Appl. Surf. Sci.* **2018**, *427*, 74–82.

(202) Cheng, H.; Yue, K.; Kazemzadeh-Narbat, M.; Liu, Y.; Khalilpour, A.; Li, B.; Zhang, Y. S.; Annabi, N.; Khademhosseini, A. Mussel-Inspired Multifunctional Hydrogel Coating for Prevention of Infections and Enhanced Osteogenesis. *ACS Appl. Mater. Interfaces* **2017**, *9*, 11428–11439.

(203) Xu, L. Q.; Chen, J. C.; Wang, R.; Neoh, K. G.; Kang, E. T.; Fu, G. D. A Poly(Vinylidene Fluoride)-Graft-Poly(Dopamine Acrylamide) Copolymer for Surface Functionalizable Membranes. *RSC Adv.* **2013**, *3*, 25204–25214.

(204) Statz, A. R.; Meagher, R. J.; Barron, A. E.; Messersmith, P. B. New Peptidomimetic Polymers for Antifouling Surfaces. *J. Am. Chem. Soc.* **2005**, *127*, 7972–7973.

(205) Bhatt, R. R.; Shah, B. A. Sorption Studies of Heavy Metal Ions by Salicylic Acid–Formaldehyde–Catechol Terpolymeric Resin: Isotherm, Kinetic and Thermodynamics. *Arab. J. Chem.* **2015**, *8*, 414–426.

(206) Li, L.; Li, Y.; Luo, X.; Deng, J.; Yang, W. Helical Poly(N-Propargylamide)s with Functional Catechol Groups: Synthesis and Adsorption of Metal Ions in Aqueous Solution. *React. Funct.*

Polym. **2010**, *70*, 938–943.

(207) Vetriselvi, V.; Jaya Santhi, R. Redox Polymer as an Adsorbent for the Removal of Chromium (VI) and Lead (II) from the Tannery Effluents. *Water Resour. Ind.* **2015**, *10*, 39–52.

(208) Lemos, V. A.; dos Passos, A. S.; dos Santos Novaes, G.; de Andrade Santana, D.; de Carvalho, A. L.; da Silva, D. G. Determination of Cobalt, Copper and Nickel in Food Samples after Pre-Concentration on a New Pyrocatechol-Functionalized Polyurethane Foam Sorbent. *React. Funct. Polym.* **2007**, *67*, 573–581.

(209) Kara, D.; Fisher, A.; Hill, S. J. Comparison of Some Newly Synthesized Chemically Modified Amberlite XAD-4 Resins for the Preconcentration and Determination of Trace Elements by Flow Injection Inductively Coupled Plasma-Mass Spectrometry (ICP-MS). *Analyst* **2006**, *131*, 1232–1240.

(210) Draye, M.; Czerwinski, K. R.; Favre-Réguillon, A.; Foos, J.; Guy, A.; Lemaire, M. Selective Separation of Lanthanides with Phenolic Resins: Extraction Behavior and Thermal Stability. *Sep. Sci. Technol.* **2000**, *35*, 1117–1132.

(211) Al-Rimawi, F.; Ahmad, A.; Khalili, F. I.; Mubarak, M. S. Chelation Properties of Some Phenolicformaldehyde Polymers toward Some Trivalent Lanthanide Ions. *Solvent Extr. Ion Exch.* **2004**, *22*, 721–735.

(212) Prabhakaran, D.; Subramanian, M. S. A Column System for the Selective Extraction of U(VI) and Th(IV) Using a New Chelating Sorbent. *Talanta* **2003**, *61*, 423–430.

(213) Sabarudin, A.; Oshima, M.; Takayanagi, T.; Hakim, L.; Oshita, K.; Gao, Y. H.; Motomizu, S. Functionalization of Chitosan with 3,4-Dihydroxybenzoic Acid for the Adsorption/Collection of

Uranium in Water Samples and Its Determination by Inductively Coupled Plasma-Mass Spectrometry. *Anal. Chim. Acta* **2007**, *581*, 214–220.

(214) Arrambide Cruz, C.; Marie, S.; Arrachart, G.; Pellet-Rostaing, S. Selective Extraction and Separation of Germanium by Catechol Based Resins. *Sep. Purif. Technol.* **2018**, *193*, 214–219.

(215) Jaishankar, M.; Tseten, T.; Anbalagan, N.; Mathew, B. B.; Beeregowda, K. N. Toxicity, Mechanism and Health Effects of Some Heavy Metals. *Interdisciplinary Toxicology*, 2014, *7*, 60–72.

(216) Yokel, R. A. *Aluminum Chelation Principles and Recent Advances*.

(217) Smith, S. W. The Role of Chelation in the Treatment of Other Metal Poisonings. *Journal of Medical Toxicology*, 2013, *9*, 355–369.

(218) Gupta, N.; Gaurav, S. S.; Kumar, A. Molecular Basis of Aluminium Toxicity in Plants: A Review. *Am. J. Plant Sci.* **2013**, *04*, 21–37.

(219) Niu, B.; Xiao, K.; Huang, X.; Zhang, Z.; Kong, X. Y.; Wang, Z.; Wen, L.; Jiang, L. High-Sensitivity Detection of Iron(III) by Dopamine-Modified Funnel-Shaped Nanochannels. *ACS Appl. Mater. Interfaces* **2018**, *10*, 22632–22639.

(220) Muñoz, J.; Montes, R.; Bastos-Arrieta, J.; Guardingo, M.; Busqué, F.; Ruíz-Molina, D.; Palet, C.; García-Orellana, J.; Baeza, M. Carbon Nanotube-Based Nanocomposite Sensor Tuned with a Catechol as Novel Electrochemical Recognition Platform of Uranyl Ion in Aqueous Samples. *Sensors Actuators B Chem.* **2018**, *273*, 1807–1815.

(221) Holten-Andersen, N.; Harrington, M. J.; Birkedal, H.; Lee, B. P.; Messersmith, P. B.; Lee, K. Y. C.; Waite, J. H. PH-Induced Metal-Ligand Cross-Links Inspired by Mussel Yield Self-Healing

Polymer Networks with near-Covalent Elastic Moduli. *Proc. Natl. Acad. Sci.* **2011**, *108*, 2651–2655.

(222) Krogsgaard, M.; Behrens, M. A.; Pedersen, J. S.; Birkedal, H. Self-Healing Mussel-Inspired Multi-PH-Responsive Hydrogels. *Biomacromolecules* **2013**, *14*, 297–301.

(223) Jia, Z.; Zeng, Y.; Tang, P.; Gan, D.; Xing, W.; Hou, Y.; Wang, K.; Xie, C.; Lu, X. Conductive, Tough, Transparent, and Self-Healing Hydrogels Based on Catechol-Metal Ion Dual Self-Catalysis. *Chem. Mater.* **2019**, *31*, 5625–5632.

(224) Filippidi, E.; Cristiani, T. R.; Eisenbach, C. D.; Herbert Waite, J.; Israelachvili, J. N.; Kollbe Ahn, B.; Valentine, M. T. Toughening Elastomers Using Mussel-Inspired Iron-Catechol Complexes. *Science (80-.).* **2017**, *358*, 502–505.

(225) Lee, B. P.; Narkar, A.; Wilharm, R. Effect of Metal Ion Type on the Movement of Hydrogel Actuator Based on Catechol-Metal Ion Coordination Chemistry. *Sensors Actuators, B Chem.* **2016**, *227*, 248–254.

(226) Lee, B. P. Chapter 10. Mussel Adhesive-Inspired Polymers. In; 2016; pp. 322–353.

(227) Matyjaszewski, K.; Dong, H.; Jakubowski, W.; Pietrasik, J.; Kusumo, A. Grafting from Surfaces for “Everyone”: ARGET ATRP in the Presence of Air. *Langmuir* **2007**, *23*, 4528–4531.

(228) Richter, R. P. Technical Note Ellipsometric Analysis of Qcm-d Sensor Surfaces. **2010**, 1–10.

(229) Heavens, O. S. Optical Properties of Thin Films. *Reports Prog. Phys.* **1960**, *23*, 301.

(230) Matyjaszewski, K.; Miller, P. J.; Shukla, N.; Immaraporn, B.; Gelman, A.; Luokala, B. B.; Siclovan, T. M.; Kickelbick, G.; Vallant, T.; Hoffmann, H.; *et al.* Polymers at Interfaces: Using Atom Transfer Radical Polymerization in the Controlled Growth of Homopolymers and Block

Copolymers from Silicon Surfaces in the Absence of Untethered Sacrificial Initiator. *Macromolecules* **1999**, *32*, 8716–8724.

(231) Edmondson, S.; Huck, W. T. S. Controlled Growth and Subsequent Chemical Modification of Poly(Glycidyl Methacrylate) Brushes on Silicon Wafers. *J. Mater. Chem.* **2004**, 730–734.

(232) Long, D. A. Infrared and Raman Characteristic Group Frequencies. Tables and ChartsGeorge Socrates John. **2001**.

(233) Lemon, M. T.; Jones, M. S.; Stansbury, J. W. Hydrogen Bonding Interactions in Methacrylate Monomers and Polymers. *J. Biomed. Mater. Res. Part A* **2007**, *83A*, 734–746.

(234) Barbey, R.; Klok, H. A. Room Temperature, Aqueous Post-Polymerization Modification of Glycidyl Methacrylate-Containing Polymer Brushes Prepared via Surface-Initiated Atom Transfer Radical Polymerization. *Langmuir* **2010**, *26*, 18219–18230.

(235) Kord Forooshani, P.; Polega, E.; Thomson, K.; Bhuiyan, M. S. A.; Pinnaratip, R.; Trought, M.; Kendrick, C.; Gao, Y.; Perrine, K. A.; Pan, L.; *et al.* Antibacterial Properties of Mussel-Inspired Polydopamine Coatings Prepared by a Simple Two-Step Shaking-Assisted Method. *Front. Chem.* **2019**, *7*.

(236) Luo, R.; Tang, L.; Zhong, S.; Yang, Z.; Wang, J.; Weng, Y.; Tu, Q.; Jiang, C.; Huang, N. In Vitro Investigation of Enhanced Hemocompatibility and Endothelial Cell Proliferation Associated with Quinone-Rich Polydopamine Coating. *ACS Appl. Mater. Interfaces* **2013**, *5*, 1704–1714.

(237) Bordes, R.; Tropsch, J.; Holmberg, K. Adsorption of Dianionic Surfactants Based on Amino Acids at Different Surfaces Studied by QCM-D and SPR. *Langmuir* **2010**, *26*, 10935–10942.

(238) Sikora, F. J.; McBride, M. B. Aluminum Complexation by Catechol as Determined by Ultraviolet

Spectrophotometry. *Environ. Sci. Technol.* **1989**, *23*, 349–356.

(239) Korpany, K. V.; Majewski, D. D.; Chiu, C. T.; Cross, S. N.; Blum, A. S. Iron Oxide Surface Chemistry: Effect of Chemical Structure on Binding in Benzoic Acid and Catechol Derivatives. *Langmuir* **2017**, *33*, 3000–3013.

(240) Sauerbrey, G. Verwendung von Schwingquarzen Zur Wägung Dünner Schichten Und Zur Mikrowägung. *Zeitschrift für Phys.* **1959**, *155*, 206–222.

(241) Dixon, M. C. Quartz Crystal Microbalance with Dissipation Monitoring: Enabling Real-Time Characterization of Biological Materials and Their Interactions. *Journal of Biomolecular Techniques*, 2008, *19*, 151–158.

(242) Kankare, J. Sauerbrey Equation of Quartz Crystal Microbalance in Liquid Medium. *Langmuir* **2002**, *18*, 7092–7094.

(243) Yang, C. hai. Statistical Mechanical Study on the Freundlich Isotherm Equation. *J. Colloid Interface Sci.* **1998**, *208*, 379–387.

(244) Skopp, J. Derivation of the Freundlich Adsorption Isotherm from Kinetics. *J. Chem. Educ.* **2009**, *86*, 1341.

(245) Foo, K. Y.; Hameed, B. H. Insights into the Modeling of Adsorption Isotherm Systems. *Chem. Eng. J.* **2010**, *156*, 2–10.

(246) McKay, G. *Use of Adsorbents for the Removal of Pollutants from Wastewater*; 1995.

(247) Leitgeb, A.; Wappel, J.; Slugovc, C. The ROMP Toolbox Upgraded. *Polymer (Guildf).* **2010**, *51*, 2927–2946.

(248) Sonntag, N. O. V. The Reactions of Aliphatic Acid Chlorides. *Chem. Rev.* **1953**, *52*, 237–416.

(249) Deng, X.; Prozorovska, L.; Kane Jennings, G. Metal Chelating Polymer Thin Films by Surface-Initiated ROMP and Modification. *J. Phys. Chem. C* **2019**.

(250) Ameduri, B. Fluoropolymers: The Right Material for the Right Applications. *Chemistry - A European Journal*, 2018, *24*, 18830–18841.

(251) Cui, Z.; Drioli, E.; Lee, Y. M. Recent Progress in Fluoropolymers for Membranes. *Progress in Polymer Science*, 2014, *39*, 164–198.

(252) Cardoso, V. F.; Correia, D. M.; Ribeiro, C.; Fernandes, M. M.; Lanceros-Méndez, S. Fluorinated Polymers as Smart Materials for Advanced Biomedical Applications. *Polymers*, 2018, *10*, 161.

(253) Liang, C. Y.; Krimm, S. Infrared Spectra of High Polymers. III. Polytetrafluoroethylene and Polychlorotrifluoroethylene. *J. Chem. Phys.* **1956**, *25*, 563–571.

(254) Berron, B. J.; Faulkner, C. J.; Fischer, R. E.; Payne, P. A.; Jennings, G. K. Surface-Initiated Growth of Ionomer Films from Pt-Modified Gold Electrodes. *Langmuir* **2009**, *25*, 12721–12728.

(255) Kovačič, S.; Slugovc, C. Ring-Opening Metathesis Polymerisation Derived Poly(Dicyclopentadiene) Based Materials. *Mater. Chem. Front.* **2020**, *4*, 2235–2255.

(256) Mol, J. C. Industrial Applications of Olefin Metathesis. In *Journal of Molecular Catalysis A: Chemical*; Elsevier, 2004; Vol. 213, pp. 39–45.

(257) Njoroge, I.; Kempler, P. A.; Deng, X.; Arnold, S. T.; Jennings, G. K. Surface-Initiated Ring-Opening Metathesis Polymerization of Dicyclopentadiene from the Vapor Phase. *Langmuir* **2017**, *33*, 13903–13912.

(258) Dong, J.; Ozaki, Y.; Nakashima, K. Infrared, Raman, and near-Infrared Spectroscopic Evidence for the Coexistence of Various Hydrogen-Bond Forms in Poly(Acrylic Acid). *Macromolecules*

1997, *30*, 1111–1117.

(259) Jencks, W. P. The Reaction of Hydroxylamine with Activated Acyl Groups. II. Mechanism of the Reaction. *J. Am. Chem. Soc.* **1958**, *80*, 4585–4588.

(260) Jencks, W. P. The Reaction of Hydroxylamine with Activated Acyl Groups. I. Formation of O-Acylhy Droxylamine. *J. Am. Chem. Soc.* **1958**, *80*, 4581–4584.

(261) Winston, A.; Mazza, E. T. HYDROXAMIC ACID POLYMERS. *J Polym Sci Polym Chem Ed* **1975**, *13*, 2019–2030.

(262) Yong Wen, S. S.; Rahman, M. L.; Arshad, S. E.; Surugau, N. L.; Musta, B. Synthesis and Characterization of Poly(Hydroxamic Acid)-Poly(Amidoxime) Chelating Ligands from Polymer-Grafted Acacia Cellulose. *J. Appl. Polym. Sci.* **2011**, *124*, n/a-n/a.

(263) Rahman, M. L.; Wong, Z. J.; Sarjadi, M. S.; Abdullah, M. H.; Heffernan, M. A.; Sarkar, M. S.; O'Reilly, E. Poly(Hydroxamic Acid) Ligand from Palm-based Waste Materials for Removal of Heavy Metals from Electroplating Wastewater. *J. Appl. Polym. Sci.* **2021**, *138*, 49671.

(264) Hostert, L.; Zarbin, A. J. G.; Orth, E. S. Hydroxamic Acid-Functionalized Graphene Thin Films as Nanocatalysts towards Organophosphate Degradation. *J. Phys. Mater.* **2020**, *3*, 034003.

(265) Nguyen, T. K. L.; Livi, S.; Soares, B. G.; Pruvost, S.; Duchet-Rumeau, J.; Gérard, J. F. Ionic Liquids: A New Route for the Design of Epoxy Networks. *ACS Sustain. Chem. Eng.* **2016**, *4*, 481–490.

(266) Lu, J.; Yan, F.; Texter, J. Advanced Applications of Ionic Liquids in Polymer Science. *Progress in Polymer Science (Oxford)*, 2009, *34*, 431–448.

(267) Freemantle, M. An Introduction of Ionic Liquids. In; RCS Publishing, 2009.

(268) Rahmathullah, M. A. M.; Jeyarajasingam, A.; Merritt, B.; VanLandingham, M.; McKnight, S. H.; Palmese, G. R. Room Temperature Ionic Liquids as Thermally Latent Initiators for Polymerization of Epoxy Resins. *Macromolecules* **2009**, *42*, 3219–3221.

(269) Maksym, P.; Tarnacka, M.; Dzienia, A.; Matuszek, K.; Chrobok, A.; Kaminski, K.; Paluch, M. Enhanced Polymerization Rate and Conductivity of Ionic Liquid-Based Epoxy Resin. *Macromolecules* **2017**, *50*, 3262–3272.

(270) Maka, H.; Spychaj, T. Epoxy Resin Crosslinked with Conventional and Deep Eutectic Ionic Liquids. *Polimery/Polymers* **2012**, *57*, 456–462.

(271) Nguyen, T. K. L.; Livi, S.; Pruvost, S.; Soares, B. G.; Duchet-Rumeau, J. Ionic Liquids as Reactive Additives for the Preparation and Modification of Epoxy Networks. *J. Polym. Sci. Part A Polym. Chem.* **2014**, *52*, 3463–3471.

(272) Soares, B. G.; Silva, A. A.; Livi, S.; Duchet-Rumeau, J.; Gerard, J. F. New Epoxy/Jeffamine Networks Modified with Ionic Liquids. *J. Appl. Polym. Sci.* **2014**, *131*, n/a-n/a.

(273) Ly Nguyen, T. K.; Obadia, M. M.; Serghei, A.; Livi, S.; Duchet-Rumeau, J.; Drockenmuller, E. 1,2,3-Triazolium-Based Epoxy-Amine Networks: Ion-Conducting Polymer Electrolytes. *Macromol. Rapid Commun.* **2016**, *37*, 1168–1174.

(274) Sanes, J.; Carrión-Vilches, F. J.; Bermúdez, M. D. New Epoxy-Ionic Liquid Dispersions. Room Temperature Ionic Liquid as Lubricant of Epoxy Resin-Stainless Steel Contacts. *E-Polymers* **2007**, *7*, 1–12.

(275) Shirshova, N.; Bismarck, A.; Carreyette, S.; Fontana, Q. P. V.; Greenhalgh, E. S.; Jacobsson, P.; Johansson, P.; Marczewski, M. J.; Kalinka, G.; Kucernak, A. R. J.; *et al.* Structural

Supercapacitor Electrolytes Based on Bicontinuous Ionic Liquid-Epoxy Resin Systems. *J. Mater. Chem. A* **2013**, *1*, 15300–15309.

(276) Shirshova, N.; Bismarck, A.; Greenhalgh, E. S.; Johansson, P.; Kalinka, G.; Marczewski, M. J.; Shaffer, M. S. P.; Wienrich, M. Composition as a Means to Control Morphology and Properties of Epoxy Based Dual-Phase Structural Electrolytes. *J. Phys. Chem. C* **2014**, *118*, 28377–28387.

(277) Westover, A. S.; Baer, B.; Bello, B. H.; Sun, H.; Oakes, L.; Bellan, L. M.; Pint, C. L. Multifunctional High Strength and High Energy Epoxy Composite Structural Supercapacitors with Wet-Dry Operational Stability. *J. Mater. Chem. A* **2015**, *3*, 20097–20102.

(278) Barton, J. M.; Harnerton, I.; Howlin, B. J.; Jones, J. R.; Liu, S. Studies of Cure Schedule and Final Property Relationships of a Commercial Epoxy Resin Using Modified Imidazole Curing Agents. *Polymer (Guildf).* **1998**, *39*, 1929–1937.

(279) Wang, M.; Yu, Y.; Wu, X.; Li, S. Polymerization Induced Phase Separation in Poly(Ether Imide)-Modified Epoxy Resin Cured with Imidazole. *Polymer (Guildf).* **2004**, *45*, 1253–1259.

(280) O'Brien, D. J.; Mather, P. T.; White, S. R. Viscoelastic Properties of an Epoxy Resin during Cure. *J. Compos. Mater.* **2001**, *35*, 883–904.

(281) O'Brien, D. J.; Sottos, N. R.; White, S. R. Cure-Dependent Viscoelastic Poisson's Ratio of Epoxy. *Exp. Mech.* **2007**, *47*, 237–249.

(282) Simpson, J. O.; Bidstrup, S. A. Rheological and Dielectric Changes during Isothermal Epoxy-amine Cure. *J. Polym. Sci. Part B Polym. Phys.* **1995**, *33*, 55–62.

(283) Klosterman, D.; Li, L.; Morris, J. E. Materials Characterization, Conduction Development, and Curing Effects on Reliability of Isotropically Conductive Adhesives. *IEEE Trans. Components*

Packag. Manuf. Technol. Part A **1998**, *21*, 23–31.

(284) Kortaberria, G.; Arruti, P.; Mondragon, I. Dielectric Monitoring of Curing of Liquid Oligomer-Modified Epoxy Matrices. *Polym. Int.* **2001**, *50*, 957–965.

(285) deBakker, C. J.; George, G. A.; St John, N. A.; Fredericks, P. M. The Kinetics of the Cure of an Advanced Epoxy Resin by Fourier Transform Raman and Near-IR Spectroscopy. *Spectrochim. Acta Part A Mol. Spectrosc.* **1993**, *49*, 739–752.

(286) González, M. G.; Cabanelas, J. C.; Baselga, J. Applications of FTIR on Epoxy Resins - Identification, Monitoring the Curing Process, Phase Separation and Water Uptake. In *Infrared Spectroscopy - Materials Science, Engineering and Technology*; InTech, 2012.

(287) Mijović, J.; Kenny, J. M.; Maffezzoli, A.; Trivisano, A.; Bellucci, F.; Nicolais, L. The Principles of Dielectric Measurements for in Situ Monitoring of Composite Processing. *Compos. Sci. Technol.* **1993**, *49*, 277–290.

(288) Andjelić, S.; Mijović, J.; Bellucci, F. Impedance Spectroscopy of Reactive Polymers. 5. Impedance as a Measure of Chemical and Physical Changes in Glass Formers. *J. Polym. Sci. Part B Polym. Phys.* **1998**, *36*, 641–653.

(289) Gallone, G.; Levita, J.; Mijovic, S.; Andjelic, S.; Rolla, P. A. Anomalous Trends in Conductivity during Epoxy-Amine Reactions. *Polymer (Guildf).* **1998**, *39*, 2095–2102.

(290) Kranbuehl, D.; Delos, S.; Hoff, M.; Haverty, P.; Freeman, W.; Hoffman, R.; Godfrey, J. Use of the Frequency Dependence of the Impedance to Monitor Viscosity during Cure. *Polym. Eng. Sci.* **1989**, *29*, 285–289.

(291) García-Sánchez, M. F.; M'Peko, J. C.; Ruiz-Salvador, A. R.; Rodríguez-Gattorno, G.; Echevarría,

Y.; Fernández-Gutierrez, F.; Delgado, A. An Elementary Picture of Dielectric Spectroscopy in Solids: Physical Basis. *J. Chem. Educ.* **2003**, *80*, 1062–1073.

(292) MacDonald, D. D. Reflections on the History of Electrochemical Impedance Spectroscopy. In *Electrochimica Acta*; Pergamon, 2006; Vol. 51, pp. 1376–1388.

(293) Mansfeld, F. Electrochemical Impedance Spectroscopy (EIS) as a New Tool for Investigating Methods of Corrosion Protection. *Electrochim. Acta* **1990**, *35*, 1533–1544.

(294) Leng, W. H.; Zhang, Z.; Zhang, J. Q.; Cao, C. N. Investigation of the Kinetics of a TiO2 Photoelectrocatalytic Reaction Involving Charge Transfer and Recombination through Surface States by Electrochemical Impedance Spectroscopy. *J. Phys. Chem. B* **2005**, *109*, 15008–15023.

(295) Cheng, H.; Zhu, C.; Huang, B.; Lu, M.; Yang, Y. Synthesis and Electrochemical Characterization of PEO-Based Polymer Electrolytes with Room Temperature Ionic Liquids. *Electrochim. Acta* **2007**, *52*, 5789–5794.

(296) Evans, J.; Vincent, C. A.; Bruce, P. G. Electrochemical Measurement of Transference Numbers in Polymer Electrolytes. *Polymer (Guildf).* **1987**, *28*, 2324–2328.

(297) Han, Y.; Wang, J.; Zhang, H.; Zhao, S.; Ma, Q.; Wang, Z. Electrochemical Impedance Spectroscopy (EIS): An Efficiency Method to Monitor Resin Curing Processes. *Sensors Actuators, A Phys.* **2016**, *250*, 78–86.

(298) Mijović, J.; Andjelić, S. A Study of Reaction Kinetics by Near-Infrared Spectroscopy. 1. Comprehensive Analysis of a Model Epoxy/Amine System. *Macromolecules* **1995**, *28*, 2787–2796.

(299) Skordos, A. A.; Partridge, I. K. Determination of the Degree of Cure under Dynamic and

Isothermal Curing Conditions with Electrical Impedance Spectroscopy. *J. Polym. Sci. Part B Polym. Phys.* **2004**, *42*, 146–154.

(300) ASTM D695-02a, A. I. Standard Test Method for Compressive Properties of Rigid Plastics. *ASTM Int. West Conshohocken, PA* **2002**, *03*, 1–8.

(301) Kessler, M. R.; White, S. R. Cure Kinetics of the Ring-Opening Metathesis Polymerization of Dicyclopentadiene. *J. Polym. Sci. Part A Polym. Chem.* **2002**, *40*, 2373–2383.

(302) Kienle, R. H.; Race, H. H. The Electrical, Chemical and Physical Properties of Alkyd Resins. *Trans. Electrochem. Soc.* **1934**, *65*, 87.

(303) Nass, K. A.; Seferis, J. C. Analysis of the Dielectric Response of Thermosets During Isothermal and Nonisothermal Cure. *Polym. Eng. Sci.* **1989**, *29*, 315–324.

(304) Matsumoto, K.; Endo, T. Confinement of Ionic Liquid by Networked Polymers Based on Multifunctional Epoxy Resins. *Macromolecules* **2008**, *41*, 6981–6986.

(305) Maïstros, G. M.; Block, H.; Bucknall, C. B.; Partridge, I. K. Dielectric Monitoring of Phase Separation during Cure of Blends of Epoxy Resin with Carboxyl-Terminated Poly(Butadiene-Co-Acrylonitrile). *Polymer (Guildf).* **1992**, *33*, 4470–4478.

(306) Staudinger, H. Über Polymerisation. *Berichte der Dtsch. Chem. Gesellschaft (A B Ser.* **1920**, *53*, 1073–1085.

(307) Abd-El-Aziz, A. S.; Antonietti, M.; Barner-Kowollik, C.; Binder, W. H.; Böker, A.; Boyer, C.; Buchmeiser, M. R.; Cheng, S. Z. D.; D'Agosto, F.; Floudas, G.; *et al.* The Next 100 Years of Polymer Science. *Macromol. Chem. Phys.* **2020**, *221*, 2000216.

(308) Morawetz, H. Difficulties in the Emergence of the Polymer Concept—an Essay. *Angewandte*

Chemie International Edition in English, 1987, *26*, 93–97.

(309) Kim, Y. J. o.; Wu, W.; Chun, S. E.; Whitacre, J. F.; Bettinger, C. J. Catechol-Mediated Reversible Binding of Multivalent Cations in Eumelanin Half-Cells. *Adv. Mater.* **2014**, *26*, 6572–6579.

(310) Son, E. J.; Kim, J. H.; Kim, K.; Park, C. B. Quinone and Its Derivatives for Energy Harvesting and Storage Materials. *J. Mater. Chem. A* **2016**, *4*, 11179–11202.

(311) Patil, N.; Aqil, A.; Ouhib, F.; Admassie, S.; Inganäs, O.; Jérôme, C.; Detrembleur, C. Bioinspired Redox-Active Catechol-Bearing Polymers as Ultrarobust Organic Cathodes for Lithium Storage. *Adv. Mater.* **2017**, *29*, 1703373.

(312) Li, J.; Ejima, H.; Yoshie, N. Seawater-Assisted Self-Healing of Catechol Polymers via Hydrogen Bonding and Coordination Interactions. *ACS Appl. Mater. Interfaces* **2016**, *8*, 19047–19053.

(313) Li, X.; Gao, P.; Tan, J.; Xiong, K.; Maitz, M. F.; Pan, C.; Wu, H.; Chen, Y.; Yang, Z.; Huang, N. Assembly of Metal-Phenolic/Catecholamine Networks for Synergistically Anti-Inflammatory, Antimicrobial, and Anticoagulant Coatings. *ACS Appl. Mater. Interfaces* **2018**, *10*, 40844–40853.

(314) Kim, Y. J.; Matsunaga, Y. T. Thermo-Responsive Polymers and Their Application as Smart Biomaterials. *Journal of Materials Chemistry B*, 2017, *5*, 4307–4321.

(315) Paulus, A. S.; Heinzler, R.; Ooi, H. W.; Franzreb, M. Temperature-Switchable Agglomeration of Magnetic Particles Designed for Continuous Separation Processes in Biotechnology. *ACS Appl. Mater. Interfaces* **2015**, *7*, 14279–14287.

(316) Nagl, S.; Wolfbeis, O. S. Optical Multiple Chemical Sensing: Status and Current Challenges. *Analyst* **2007**, *132*, 507.

(317) Schneiderman, D. K.; Hillmyer, M. A. 50th Anniversary Perspective: There Is a Great Future in

Sustainable Polymers. *Macromolecules* **2017**, *50*, 3733–3749.

(318) Bai, Y.; Muralidharan, N.; Sun, Y. K.; Passerini, S.; Stanley Whittingham, M.; Belharouak, I. Energy and Environmental Aspects in Recycling Lithium-Ion Batteries: Concept of Battery Identity Global Passport. *Materials Today*, 2020, *41*, 304–315.

(319) Shan, L.; Gu, J.; Fan, H.; Ji, S.; Zhang, G. Microphase Diffusion-Controlled Interfacial Polymerization for an Ultrahigh Permeability Nanofiltration Membrane. *ACS Appl. Mater. Interfaces* **2017**, *9*, 44820–44827.

(320) Nghiem, L. D.; Schäfer, A. I.; Elimelech, M. Pharmaceutical Retention Mechanisms by Nanofiltration Membranes. *Environ. Sci. Technol.* **2005**, *39*, 7698–7705.

(321) Nghiem, L. D.; Schäfer, A. I.; Elimelech, M. Removal of Natural Hormones by Nanofiltration Membranes: Measurement, Modeling and Mechanisms. *Environ. Sci. Technol.* **2004**, *38*, 1888–1896.

(322) Van Der Bruggen, B.; Everaert, K.; Wilms, D.; Vandecasteele, C. Application of Nanofiltration for Removal of Pesticides, Nitrate and Hardness from Ground Water: Rejection Properties and Economic Evaluation. *J. Memb. Sci.* **2001**, *193*, 239–248.

(323) Zhu, J.; Tian, M.; Zhang, Y.; Zhang, H.; Liu, J. Fabrication of a Novel “Loose” Nanofiltration Membrane by Facile Blending with Chitosan-Montmorillonite Nanosheets for Dyes Purification. *Chem. Eng. J.* **2015**, *265*, 184–193.

(324) Prozorovska, L.; Kidambi, P. R. State-of-the-Art and Future Prospects for Atomically Thin Membranes from 2D Materials. *Adv. Mater.* **2018**, *30*, 1801179.

(325) Malaisamy, R.; Bruening, M. L. High-Flux Nanofiltration Membranes Prepared by Adsorption of

Multilayer Polyelectrolyte Membranes on Polymeric Supports. *Langmuir* **2005**, *21*, 10587–10592.

(326) Ba, C.; Ladner, D. A.; Economy, J. Using Polyelectrolyte Coatings to Improve Fouling Resistance of a Positively Charged Nanofiltration Membrane. *J. Memb. Sci.* **2010**, *347*, 250–259.

(327) Cho, K. L.; Hill, A. J.; Caruso, F.; Kentish, S. E. Chlorine Resistant Glutaraldehyde Crosslinked Polyelectrolyte Multilayer Membranes for Desalination. *Adv. Mater.* **2015**, *27*, 2791–2796.

(328) Shan, L.; Liang, Y.; Prozorovska, L.; Jennings, G. K.; Ji, S.; Lin, S. Multifold Enhancement of Loose Nanofiltration Membrane Performance by Intercalation of Surfactant Assemblies. *Environ. Sci. Technol. Lett.* **2018**, *5*, 668–674.

(329) El-Khouri, R. J.; Johal, M. S. Fine-Tuning the Wetting Behavior of Polyelectrolyte Films with Sodium Dodecyl Sulfate. *Langmuir*, 2003, *19*, 4880–4883.

(330) Prosser, A. J.; Franses, E. I. Infrared Reflection Absorption Spectroscopy (IRRAS) of Aqueous Nonsurfactant Salts, Ionic Surfactants, and Mixed Ionic Surfactants. *Langmuir* **2002**, *18*, 9234–9242.

(331) Peng, C.; Thio, Y. S.; Gerhardt, R. A. Enhancing the Layer-by-Layer Assembly of Indium Tin Oxide Thin Films by Using Polyethyleneimine. *J. Phys. Chem. C* **2010**, *114*, 9685–9692.

(332) Schoeler, B.; Kumaraswamy, G.; Caruso, F. Investigation of the Influence of Polyelectrolyte Charge Density on the Growth of Multilayer Thin Films Prepared by the Layer-by-Layer Technique. *Macromolecules* **2002**, *35*, 889–897.

(333) Ober, C. K.; Wegner, G. Polyelectrolyte-Surfactant Complexes in the Solid State: Facile Building Blocks for Self-Organizing Materials. *Adv. Mater.* **1997**, *9*, 17–31.

(334) Varga, I.; Mezei, A.; Mészáros, R.; Claesson, P. M. Controlling the Interaction of Poly(Ethylene Imine) Adsorption Layers with Oppositely Charged Surfactant by Tuning the Structure of the Preadsorbed Polyelectrolyte Layer. *Soft Matter* **2011**, *7*, 10701–10712.

(335) Viana, R. B.; Da Silva, A. B. F.; Pimentel, A. S. Infrared Spectroscopy of Anionic, Cationic, and Zwitterionic Surfactants. *Adv. Phys. Chem.* **2012**, *2012*, 14.

(336) Song, S. H.; Koelsch, P.; Weidner, T.; Wagner, M. S.; Castner, D. G. Sodium Dodecyl Sulfate Adsorption onto Positively Charged Surfaces: Monolayer Formation with Opposing Headgroup Orientations. *Langmuir* **2013**, *29*, 12710–12719.

(337) Sperline, R. P. Infrared Spectroscopic Study of the Crystalline Phases of Sodium Dodecyl Sulfate. *Langmuir* **1997**, *13*, 3715–3726.